

Regularization of ill-posed inverse problem in ultrasound tomography

Carević, Anita

Doctoral thesis / Disertacija

2020

Degree Grantor / Ustanova koja je dodijelila akademski / stručni stupanj: **University of Zagreb, Faculty of Science / Sveučilište u Zagrebu, Prirodoslovno-matematički fakultet**

Permanent link / Trajna poveznica: <https://um.nsk.hr/um:nbn:hr:217:364338>

Rights / Prava: [In copyright](#) / [Zaštićeno autorskim pravom.](#)

Download date / Datum preuzimanja: **2025-03-13**



Repository / Repozitorij:

[Repository of the Faculty of Science - University of Zagreb](#)





University of Zagreb

Faculty of science
Department of Mathematics

Anita Carević

REGULARIZATION OF ILL-POSED INVERSE PROBLEM IN ULTRASOUND TOMOGRAPHY

DOCTORAL DISSERTATION

Zagreb, 2020.



University of Zagreb

Faculty of science
Department of Mathematics

Anita Carević

REGULARIZATION OF ILL-POSED INVERSE PROBLEM IN ULTRASOUND TOMOGRAPHY

DOCTORAL DISSERTATION

Supervisors:

Prof. dr. sc. Ivan Slapničar
Doc. dr. sc. Mohamed Almekkawy

Zagreb, 2020.



Sveučilište u Zagrebu

Prirodoslovno – matematički fakultet
Matematički odsjek

Anita Carević

REGULARIZACIJA LOŠE UVJETOVANOG INVERZNOG PROBLEMA U ULTRAZVUČNOJ TOMOGRAFIJI

DOKTORSKI RAD

Mentori:

Prof. dr. sc. Ivan Slapničar
Doc. dr. sc. Mohamed Almekkawy

Zagreb, 2020.

Acknowledgments

I would like to express my deepest gratitude to my two supervisors prof. dr. sc. Ivan Slapničar and doc. dr. sc. Mohamed Almekkawy for giving me the opportunity to work with them, devoting their time and advising me during my research. In addition, I would like to thank prof. Jesse Barlow for welcoming me to Penn State University, for his ideas and advice that were very helpful to me. I would like to thank Geunseop Lee for sharing his codes with me. Furthermore, I would like to thank my colleagues at Faculty of Electrical Engineering, Mechanical Engineering and Naval Architecture, especially from the Department of Mathematics and Physics, for their valuable support and advice. In addition, I would like to thank Antonija, Ante, Karla and Kata for welcoming me in Zagreb during my PhD program. Finally, I would like to thank my family Jure, Cvita, Jelena and Milan for believing in me and Josip for his encouragement and support.

Abstract

Ultrasound tomography (UT) is a medical imaging modality which can be used for the detection of breast cancer. One of the ways to solve the problem of UT is to use the distorted Born iterative method. In order for this method to provide a good solution, an ill-posed inverse problem must be solved within each iteration. In this dissertation, we regularize the inverse problem using direct spectral filtering methods. We show the advantage of using them in general form instead of standard, since employing modification of discrete version of first order derivative operator will provide additional regularization. The goal of the aforementioned methods is to minimize the influence of smaller (generalized) singular values, so the selection of the regularization parameter that is determining which of the values will be omitted is crucial to these methods. For this purpose we develop a new algorithm for choosing the regularization parameter that is, minimizing the residual and the error resulted from the noise of the measured data. In addition, we regularize the inverse problem using new forms of regularized total least squares where the existing problem is projected onto lower dimensional subspace. The dimension reduction is achieved by employing a generalized Krylov subspace expansion which results in significant decrease of computational time. In addition, the problem associated with finding the regularization parameter is avoided since an integrated parameter search inside the method is provided.

Keywords

Ill posed inverse problem, regularization methods, regularization parameters, ultrasound tomography, distorted Born iterative method, regularized total least squares method

Sažetak

Ultrazvučna tomografija (UT) je dijagnostička radiološka metoda koja se može koristiti za otkrivanje karcinoma dojke. Jedan od načina za rješavanje problema UT-a je uporaba perturbirane Bornove iterativne metode. Ova metoda može dati dobro rješenje samo ako se unutar svake njene iteracije riješi loše uvjetovan inverzni problem. U ovoj disertaciji regulariziramo loše uvjetovani inverzni problem u ultrazvučnoj tomografiji koristeći direktne spektralne metode kod kojih ćemo pokazati prednost korištenja njihovog generaliziranog oblika nad standardnim budući da se dodatna regularizacija postiže upotrebom modificirane diskretizirane verzije operatora prve derivacije. Ideja prije spomenutih metoda je smanjiti utjecaj najmanjih (generaliziranih) singularnih vrijednosti pa je odabir regularizacijskog parametra, koji će odrediti to smanjenje, od iznimne važnosti. U tu svrhu razvijamo novi algoritam za odabir parametra koji će, uz minimizaciju reziduala, minimizirati i grešku koja je posljedica šuma na vektoru izmjerenih podataka. Također, regularizaciju ćemo provesti koristeći novi ubrzani oblik metode potpunih najmanjih kvadrata gdje će se postojeći problem projicirati na potprostor niže dimenzije. Ovo rezultira smanjenjem vremena izvršavanja metode. Manja dimenzija potprostora je postignuta koristeći generalizirane Krylovljeve potprostore. Budući da metoda ima integriran algoritam za traženje parametara, izbjegnut je problem korištenja vanjske metode u tu svrhu.

Ključne riječi

Loša uvjetovost, inverzni problem, regularizacijske metode, regularizacijski parametri, ultrazvučna tomografija, perturbirana Bornova iterativna metoda, regularizirana metoda potpunih najmanjih kvadrata

Contents

1	Introduction	1
1.1	Regularization	1
1.2	Ultrasound Tomography	2
1.3	Contribution of Dissertation	5
1.4	Organization of Dissertation	5
1.5	Basic notation	7
2	Numerical Model of Ultrasound Tomography	9
2.1	Theory of a Scattering Problem	10
2.2	Forward Model	12
2.3	Inverse Model	14
2.4	Distorted Born Iterative Method	16
2.5	Simulation of Ultrasound Tomography	18
3	Preliminaries	20
3.1	Singular Value Decomposition	21
3.2	Least Squares Problem	23
3.2.1	Regularization matrix L	26
3.3	Generalized Singular Value Decomposition	28
4	Direct Regularization Methods	31
4.1	Truncated SVD and GSVD	32
4.1.1	TGSVD	34
4.2	Tikhonov Regularization	37
4.2.1	Regularized inverse and filter factors	38

4.3	Damped SVD and GSVD	41
4.4	Regularization in UT with TSVD and TGSVD	43
4.4.1	Conclusions	45
4.5	Regularization in UT with DSVD and DGSVD	47
4.5.1	Conclusions	48
5	Choosing the Regularization Parameters	50
5.1	Standard Methods for Choosing Regularization Parameter	51
5.1.1	Generalized Cross validation (GCV)	51
5.1.2	L-curve	51
5.2	Adaptive Method based on Signal-loss and Noise Error	52
5.3	Numerical results	56
6	Different Approaches to Total Least Squares	68
6.1	Truncated Total Least Squares	69
6.2	Adaptive truncated total least squares	71
6.2.1	Numerical results	71
6.2.2	Conclusions	74
6.3	Regularized Total Least Squares	75
6.4	RTLS-Newton	76
6.4.1	Numerical results	76
6.5	Projection Based Regularized Total Least Squares	81
6.5.1	Numerical Results	82
6.5.2	Reconstruction with Born approximation and DBI	86
6.5.3	Conclusions	92
6.6	Comparison between Adaptive algorithm, RTLS-Newton and PB-RTLS . .	93
7	Conclusions	96
7.1	Summary and conclusions	96
7.2	Future work	98

List of Tables

4.1	RE- ℓ_2 of reconstructed scattering function	44
5.1	Number of transmitters (M_t) and receivers (M_r) used in full and limited aperture setting.	57
5.2	RE- ℓ_2 for Born approximation and after 10 iterations of DBI in full aperture setting.	58
6.1	Values of truncation parameter obtained using adaptive method	71
6.2	RE- ℓ_2 for the reconstructed scattering function \hat{S} using Born approximation and after 10 iterations of the DBI in both settings.	80
6.3	RE- ℓ_2 for the reconstructed scattering function using Born approximation in Full and Limited aperture setting.	86
6.4	RE- ℓ_2 for Born approximation and after 10 iterations of DBI.	93

List of Figures

2.1	The circular array of transducers surrounding the ROI.	10
2.2	The basis function expansion of the total field inside ROI using N pulse basis functions (one for each cell).	11
4.1	Exact phantom (left) and reconstruction after 10 iterations of DBI with TSVD (center) and TGSVD (right).	44
4.2	Slice plots of the scattering function after 10 iterations of DBI when TSVD and TGSVD are used for regularization. (a) Vertical slice at $x = 3.3$ mm, and (b) horizontal slice at $y = -1.33$ mm for the simulated phantom. (c) Vertical slice at $x = 13.33$ mm, and (d) horizontal slice at $y = -2.66$ mm for the modified Shepp-Logan phantom.	46
4.3	Reconstruction of the ROI after 6 iterations of DBI with (a) Pseudoinverse, (b) DSVD and (c) DGSVD, (SNR=30dB).	47
4.4	Plots of RE- ℓ_2 for scattering function during 6 iterations of DBI, f=500kHz.	48
5.1	Decrease and increase of (generalized) singular values, Signal loss error (SLE) and Noise error (NE) in the proposed adaptive method.	53
5.2	Presentation of the limited aperture setting.	56
5.3	Exact simulated phantom and breast phantom used in simulations with frequency of 1MHz.	57
5.4	Plots of the relative error (RE- ℓ_2) for the scattering function during 10 iterations of DBI. All combinations between Tikhonov regularization in standard and in general form with algorithms for obtaining the parameter (GCV, L-curve and adaptive) are tested.	59

5.5	Values of regularization parameter λ during 10 iterations of DBI obtained with three different algorithms: L-curve, GCV and the proposed adaptive algorithm.	60
5.6	The reconstructed images of simulated phantom after 10 iterations of DBI for 30 dB noise. Methods used for regularization are Tikhonov in standard and general form, while λ is obtained with L-curve, GCV and proposed adaptive algorithm.	60
5.7	The reconstructed images of breast phantom after 10 iterations of DBI for 30 dB noise. Methods used for regularization are Tikhonov in standard and general form, while λ is obtained with L-curve, GCV and proposed adaptive algorithm.	61
5.8	Vertical slice plots of phnatoms after 10 iterations of DBI in full aperture setting.	62
5.9	Vertical slice plots of phnatoms after 10 iterations of DBI in limited aperture setting.	63
5.10	L-curve plot and plot of the GCV function used for finding regularization parameter λ when Tikhonov in standard and general form is used for regularization in Born approximation and in DBI.	65
6.1	Reconstructed phantom using Born approximation (top) and after 10 iterations of DBI (bottom).	72
6.2	Plots of relative errors for scattering function (left) and scattered field (right).	73
6.3	Slice plots of scattering function after 10 iterations of DBI. Horizontal slice at $y = 0$ mm (left) and vertical slice at $x = 6.67$ mm (right).	73
6.4	The reconstructed ROI in the first setting when a noise of SNR=30dB is added to the right side b . Reconstruction with Born approximation when (a) TTLS and (c) RTLS-Newton are used for regularization. The ROI after 10 iterations of the DBI using (b) TTLS and (d) RTLS-Newton . The frequency is $f = 2$ MHz.	77

6.5	The second setting considers errors in \mathbf{X} and \mathbf{b} . The frequency is $f = 2$ MHz and the noise is SNR=30dB. Reconstruction of ROI using (a) Born approximation and (b) 10 iterations of DBI with TTLS . Reconstruction using (a) Born approximation and (b) 10 iterations of DBI with RTLS-Newton	78
6.6	(a) Plots of relative errors for the scattering function during 10 iterations of the DBI in both settings with TTLS and RTLS-Newton. (b) Slice plots of the exact and reconstructed scattering functions in the first setting (noise in \mathbf{b}) after 10 iterations of the DBI with TTLS and RTLS-Newton	79
6.7	Exact (a) first simulated, (b) second simulated and (c) breast phantom used in our simulations of UT.	82
6.8	Plots for SVD of operator matrix in Born approximation for first simulated (left), second simulated (middle) and breast phantom (right).	84
6.9	Position of transmitters and receivers in the limited aperture setting. . . .	85
6.10	Plots of the relative error $RE-\ell_2$ during the 10 iterations of the DBI method for (a) first simulated, (b) second simulated and (c) breast phantom in the full aperture setting.	87
6.11	Reconstructions of first simulated, second simulated and breast phantom after 10 iterations of DBI using TTLS and PB-RTLS in the Full aperture setting.	88
6.12	Slice plots in the Full aperture setting for first simulated phantom at $y=-1.33$ mm (top), second simulated phantom at $y=2.58$ mm (middle) and breast phantom at $y=11.25$ mm (bottom).	89
6.13	Plots of the relative error $RE-\ell_2$ during the 10 iterations of the DBI method in the Limited aperture setting with 30 dB noise for first simulated (left), second simulated (middle) and breast phantom (right).	90
6.14	Reconstructions of first simulated, second simulated and breast phantom after 10 iterations of DBI using TTLS and PB-RTLS in the Limited aperture setting.	90

6.15	Plots of the relative error $RE-\ell_2$ for PB-RTLS, RTLS-Newton and Tikhonov general Adaptive during 10 iterations of the DBI method with 30 dB (left), 25 dB (middle) and 20 dB noise (right).	94
6.16	Slice plots of the reconstructed phantom after 10 iterations of DBI for three different cases: 30 dB (left), 25 dB (middle) and 20 dB noise (right).	95

List of Algorithms

- 1 Algorithm for DBI 16
- 2 Algorithm for RTLS - Newton 79
- 3 Algorithm for PB-RTLS 83

Chapter 1

Introduction

This dissertation is focused on improving the regularization techniques for an ill-posed inverse problem in the ultrasound tomography.

Generally, an inverse problem is a process of calculating the values of parameters that are characterizing the unknown system using measured data caused by this same system. It is a common phenomenon in natural science and engineering and it arises in many fields such as signal processing, medical imaging and non destructive testing of materials. One of its special cases is the ill-posed discrete inverse problem, more precisely, a system of linear equations $\mathbf{X}\mathbf{y} = \mathbf{b}$ where ill-posedness is presented as follows. Small errors in measured vector \mathbf{b} can lead to big errors in the solution vector \mathbf{y} . In fact, singular values of matrix \mathbf{X} are gradually decreasing until they approach zero. The process of regularization is necessary as we are solving the problem with a better numerical values by de-emphasizing some of the smallest singular values.

1.1 Regularization

Regularization is a process in which an ill-posed inverse problem is replaced with a similar one that has better numerical properties. A lot of work regarding characterization of regularization methods for ill-posed discrete inverse problems $\mathbf{X}\mathbf{y} = \mathbf{b}$ was done by Hansen [33]. He analyzed the truncated singular value decomposition (TSVD)[30] where the idea was to truncate smallest singular values, to approximate \mathbf{X} with a matrix that has smaller condition number. Then, he introduced truncated generalized singular value

decomposition (TGSVD)[31] which required additional constraint on the solution \mathbf{y} by minimizing the norm of the vector $\mathbf{L}\mathbf{y}$, where \mathbf{L} is a regularization matrix. Other option was to damp (generalized) singular values using DSVD, DGSVD and Tikhonov regularization in standard and general form described in [34]. The aforementioned methods use filter factors to give more or less significance to the singular values. Hence, they are called spectral filtering methods. They are also known in literature under the name of direct regularization methods. By choosing different filter factors [33], we can define different methods. However, they all have in common the necessity for appropriate parameter that decides which singular values to be de-emphasized, whether truncating or damping them, to find an optimal solution. Algorithms that have already been developed for this purpose are L-curve [35], GCV and discrepancy principle. However, their efficiency depends on the problem being solved. In addition to these direct spectral filtering methods, new iterative methods are also developed, such as conjugate gradient and Tikhonov-Arnoldi which implements Tikhonov regularization using iterative algorithm, described in [19]. Aforementioned methods are solving the least squares problems.

Another approach to regularize the inverse problem is the truncated total least squares method (TTLS) described by Golub and Van Loan in [23]. Method takes into account not just errors in vector \mathbf{b} but also in matrix \mathbf{X} . That is why a singular decomposition of the augmented matrix $(\mathbf{X} \ \mathbf{b})$ is used and its smallest singular values are truncated. Regularization properties of TTLS were analyzed by Fierro et al in [18], where the problem remains how to chose regularization parameter, that is, how many singular values should be omitted. New regularized forms of TTLS are derived in [47] using regularization matrix \mathbf{L} , and faster forms of TTLS using bidiagonalization and generalized Krylov subspaces are shown in [46]. Efficiency of this methods is demonstrated on the image deblurring problem.

1.2 Ultrasound Tomography

One of the important inverse problems is ultrasound tomography (UT), a non-invasive method used for medical imaging. It creates an image based on acoustical properties of human tissue such as speed of sound, attenuation and scattering. Since malignant tissues

have different values from benign tissues, UT can be used in detecting early stages of breast cancer and separating malignant tumors from benign ones [15, 16, 38].

Although X-ray mammography, computerized tomography (CT Scan) and MRI are standard medical imaging systems that have been in clinical use for a long time, they still have major drawbacks. For example, X-ray mammography has a problem of differentiating between breast cancer and dense tissue [59]. In addition, during the imaging process, the patient is exposed to ionizing radiation. MRI provides a good image quality, but it is expensive and has a long examination time. UT retains their strengths while improving their shortcomings. It is safe and low cost alternative imaging modality that can be used more frequently and it can detect cancers even in dense breast tissue [59].

To reproduce an ultrasound image, an inverse scattering problem must be solved, that is, the internal properties of the object needs to be determined based on the scattered ultrasound waves that passed through that object [41]. Most researchers utilize the Born inverse solution (Born approximation) which causes the scattering function to be linear [27, 28, 42]. A forward scattering solver was developed in [56] for simultaneous reconstruction of acoustic density, attenuation and compressibility profiles which takes advantage of matrix structure. A numerical solver based on preconditioned conjugate gradient method for the inverse scattering problem of inhomogeneous medium was presented in [37], where the inverse problem was modeled with the operator equation. Convergence of iterative solvers was analyzed by Norton in [58]. Solvers based on singular value decomposition were used in [48]. Another algorithm uses the Newton-Kantorovitch method which is adaptable to many different circumstances. However, this algorithm has been proven in [63] to be computationally identical to the Born approximation. Another technique is the frequency based inverse scattering method which uses eigenfunctions of the scattering operator [49],[54]. This method has advantages in gathering and examining data and its complexity depends only on the size and structure of the scattering medium. Clinical uses of UT have been advanced by [3, 4, 20, 53, 65]. These studies developed a scanner consisting of a semi-spherical array of transducers for 3-D UT. Another improvement in the 3-D scanner was described in [73]. A different approach for UT is full wave inversion used in [2, 55, 61, 62]. A waveform inversion with source encoding method is presented in [71].

In this dissertation we model UT with integral representation of the Helmholtz equation and solve it using the distorted Born iterative (DBI) method developed by Chew and Wang [11]. They used the electromagnetic waves to find a shape and composition of imaging object, and the pulse basis functions for discretization. Later, with the same purpose, the DBI method was used with ultrasonic waves by Lu et al [52], Haddadin and Ebbini [27] [28] [26], Liu et al. in [50] and Lavarello and Oelze in [42], [43] and [44]. In [45], a 3-D reconstruction of spherical object was obtained using 2-D DBI method. In this dissertation we are focusing just on 2-D reconstruction for UT. The DBI method may not work under high frequency circumstances and is more sensitive when noise is added [27],[28].

The methods goal is to determine coefficients of the scattering function that represents the imaging object. It iteratively solves the discretized forward and inverse scattering system of linear equations. Since the method is iterative, it needs to be initialized with an estimate of scattering function. The Born approximation, which assumes that the scattering of the ultrasound wave is weak, can be used for this purpose, as already explained in [27] and [50]. More on this is presented in Chapter 2.

The drawback of the DBI method is the ill posed linear system of the inverse scattering equations. Its regularization is an important problem that has already been analyzed by utilizing well known regularization methods such as Tikhonov regularization [42], [39], Truncated SVD (TSVD), [26], Total Variation [44], Conjugate Gradient Least Squares [56], and Truncated Total Least Squares (TTLS) [50]. However, the effectiveness of most of these methods in finding acceptable solution depends largely on the choice of an appropriate regularization parameter λ that is utilized within each method. Namely, a solution is overregularized when a large regularization parameter λ is used. Then, most of the (generalized) singular values are omitted from calculating the solution. On the other hand, a solution is underregularized when a small parameter λ is utilized and then most of the (generalized) singular values are used to calculate the solution. The regularization parameter λ will be appropriate for a given problem when balance is achieved between overregularized and underregularized solutions.

Some of the standard parameter selection algorithms are Generalized Cross-Validation (GCV) [22], L-curve [35], quasi-optimality criterion [34] and the discrepancy principle [34].

The disadvantage of the discrepancy principle versus GCV and L-curve is that it requires a good noise estimate from the measured data. Over or under estimate of the noise can lead to underregularized or overregularized solution respectively. On the other hand, L-curve and GCV may failed in finding appropriate λ as shown by Lavarello and Oelze in [42]. In their paper they have proposed a scaled maximum singular value to be used as λ for Tikhonov regularization in standard form. This idea was also used in [39].

1.3 Contribution of Dissertation

The contributions of this dissertation in solving the inverse problem in ultrasound tomography when the DBI method is utilized are the following:

- Showing advantages of using direct regularization (spectral filtering) methods that employ the GSVD over methods that employ the SVD. This happens because the regularization matrix \mathbf{L} , which is responsible for noise reduction from the measured data, is utilized within GSVD.
- Developing a new algorithm for choosing the regularization parameter, suited for direct regularization methods which employ both SVD and GSVD. The algorithm provides an optimal balance between omitting and keeping singular values when used within iterations of DBI.
- Solving the problem using Newton based regularized total least squares (RTL-Newton) and projection based regularized total least squares (PB-RTL) where errors in the operator matrix are taken into account. The computational time is decreased since the problem is projected onto a lower dimensional subspace.

1.4 Organization of Dissertation

The dissertation is organized as follows:

- Since the purpose of this dissertation is to provide possible ways to regularize inverse problems in ultrasound tomography, we begin with Chapter 2 which presents

a numerical model of UT. We describe the forward and the inverse model, and detailed process of their discretization. In addition, we describe the distorted Born iterative method which is used to solve the UT problem. A simulation of the UT problem is also presented in this chapter, and it is later used to test effects of other regularization methods and algorithms described in this dissertation.

- Well-known facts from the field of numerical linear algebra, which are used through the rest of the dissertation, are stated in Chapter 3. We describe the least squares problem, matrix factorizations SVD and GSVD, and the regularization matrix \mathbf{L} .
- Direct regularization methods TSVD, TGSVD, DSVD, DGSVD and Tikhonov regularization are described in Chapter 4 using SVD, GSVD and filter factors which determine a particular method. The regularized inverse, specific to the aforementioned methods, is also introduced and its difference from the Moore-Penrose pseudoinverse is explained. In addition, numerical results, where an inverse problem of UT is regularized with TSVD, TGSVD, DSVD and DGSVD are presented. The advantages of using the methods which employ GSVD are visible in the presented numerical results. The reason is the usage of regularization matrix \mathbf{L} which smooths out the noise in the measured data.
- Algorithms for obtaining the regularization parameter λ , such as GCV and L-curve, are explained in Chapter 5. This parameter is necessary for aforementioned direct regularization methods. In addition, we present our new algorithm for obtaining the parameter λ . It is based on minimizing two inversely proportional components: signal loss and noise error. It starts with an overestimation of the noise in the measured data which is appropriately adjusted within iterations of the DBI method using the discrepancy between measured and calculated data. Using numerical simulation, we show that our algorithm, when utilized within iterations of DBI, provides a lower relative error (defined in Equation (4.22)) for the reconstruction of phantoms over GCV and L-curve. This results in better quality of images reproduced with the DBI method.
- Chapter 6 presents truncated total least squares (TTLS), adaptive TTLS, regu-

larized total least squares combined with Newton method (RTLS-Newton) and projection based regularized total least squares (PB-RTLS). Their application to regularization in ultrasound tomography is also presented.

In adaptive TTLS, truncation parameter k is found by minimizing the expression which consist of two parts: signal loss and noise error.

Using RTLS-Newton instead of TTLS for regularization within DBI results with solution that has lower relative error since the regularization matrix \mathbf{L} is employed. In addition, it is faster since solves an equivalent eigenvalue problem instead of calculating the SVD.

The advantages of using PB-RTLS over TTLS are the dimension reduction of the problem being solved and the avoidance of the SVD calculation. These results in significant decrease of computational time. The dimension reduction is achieved by projecting the problem onto lower dimensional subspace, where the subspace is expanded dynamically by employing a generalized Krylov subspace expansion. In addition, PB-RTLS is avoiding the problem associated with finding the truncation parameter in TTLS since it has integrated parameter search. In numerical simulation we show benefits of using PB-RTLS over TTLS for regularization of inverse problem in UT, both in time execution and robustness to errors.

Parts of the material in this dissertation have already been published in [1], [7], [8], [9] and [10].

1.5 Basic notation

Throughout this dissertation, we use the following notation. A matrix is denoted by a bold upper case letter such as \mathbf{X} , its i^{th} column is denoted by a bold lower case letter \mathbf{x}_i and its $(i, j)^{th}$ element is denoted by x_{ij} . That is:

$$\mathbf{X} = \left(\mathbf{x}_1 \quad \dots \quad \mathbf{x}_n \right) = \begin{pmatrix} x_{11} & \dots & x_{1n} \\ \vdots & \ddots & \vdots \\ x_{m1} & \dots & x_{mn} \end{pmatrix}.$$

A bold lower case denotes a vector, such as \mathbf{b} and its i^{th} element is denoted by b_i . A transpose of matrix \mathbf{X} is denoted by \mathbf{X}^T and conjugate transpose by $\mathbf{X}^* = \overline{\mathbf{X}}^T$. It is obvious that $(\mathbf{X}^T)^T = \mathbf{X}$ and $(\mathbf{X}^*)^* = \mathbf{X}$. The diagonal matrix \mathbf{D} is denoted with $\text{diag}(d_{11}, \dots, d_{nn})$. That is:

$$\mathbf{D} = \text{diag}(d_{11}, \dots, d_{nn}) = \begin{pmatrix} d_{11} & \dots & 0 \\ \vdots & \ddots & \vdots \\ 0 & \dots & d_{nn} \end{pmatrix}.$$

An identity matrix is denoted with \mathbf{I} .

Chapter 2

Numerical Model of Ultrasound Tomography

Ultrasound tomography (UT) is a technique used for medical imaging, mostly for breast cancer detection. It is a safe and inexpensive diagnostic which produces a quantitative image of the region of interest - ROI (composed of the background medium and the scattering object). This image contains values of acoustical parameters such as speed of sound and attenuation. Based on this values, the malignant tissue can be separated from the benign. After one transducer emits the wave, the echo is collected from the transducer array surrounding the ROI, as shown in Figure 2.1. Using this method, two measurements are made. The first, when the object is not present within ROI, is to obtain the incident field measurement. The second, when the object is present in the ROI, is to obtain the total field. Subtraction of the incident field from the total field results in the scattered field which serves as an input to a reconstruction algorithm. This process is repeated with different transducers acting as transmitters until enough data to reproduce the image is obtained. In this chapter we describe the theory of inverse scattering problem, the forward and the inverse model and the distorted Born iterative method which is used to solve them.

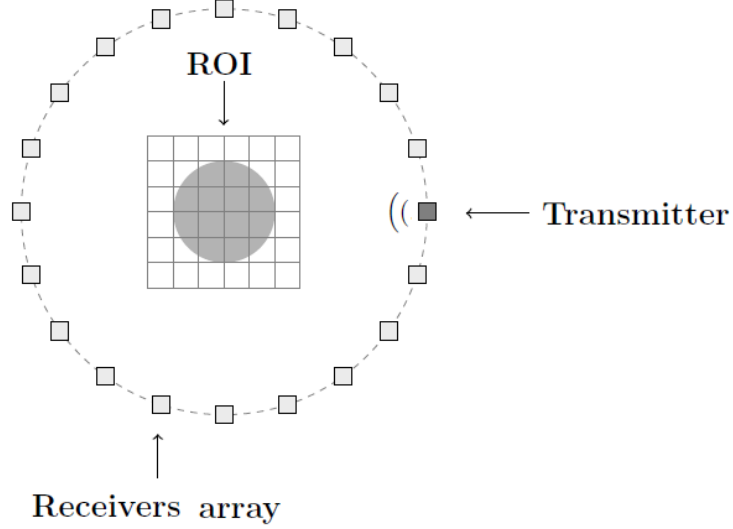


Figure 2.1: The circular array of transducers surrounding the ROI.

2.1 Theory of a Scattering Problem

A common mathematical model for acoustic wave propagation through the system composed of an infinite space containing a homogeneous acoustic medium and a scattering object embedded inside it is the Helmholtz equation [27]:

$$(\nabla^2 + k^2(\mathbf{r}))\psi_t(\mathbf{r}) = 0, \quad \psi_t(\mathbf{r}) = \psi_i(\mathbf{r}) + \psi_s(\mathbf{r}) \quad (2.1)$$

where ∇^2 is the Laplacian operator and $k(\mathbf{r})$ is the wavenumber. The incident, total and scattered field at position $\mathbf{r} = (x, y) \in \mathbb{R}^2$ are denoted with $\psi_i(\mathbf{r})$, $\psi_t(\mathbf{r})$ and $\psi_s(\mathbf{r})$ respectively. The Helmholtz equation (2.1) with Sommerfeld radiation condition [74] can be transformed to the Lippmann - Schwinger integral representation [74] as:

$$\psi_t(\mathbf{r}) = \psi_i(\mathbf{r}) + \iint_R G_0(\mathbf{r}, \mathbf{r}') s(\mathbf{r}') \psi_t(\mathbf{r}') d\mathbf{r}' \quad (2.2)$$

where \mathbf{r} and \mathbf{r}' are spatial positions of the two different points inside ROI and R denotes bounded spatial domain of the whole ROI. The scattering function is defined as [27]:

$$s(\mathbf{r}) = \omega^2 \left(\frac{1}{c^2(\mathbf{r})} - \frac{1}{c_0^2} \right) + i \frac{2\omega\alpha(\mathbf{r})}{c(\mathbf{r})} \quad (2.3)$$

where $c(\mathbf{r})$ and c_0 are speed of sound in scattering object at position \mathbf{r} and in the background medium respectively. The attenuation factor $\alpha(\mathbf{r})$ presents the decrease of amplitude and intensity of ultrasound wave as it travels through tissue and the angular

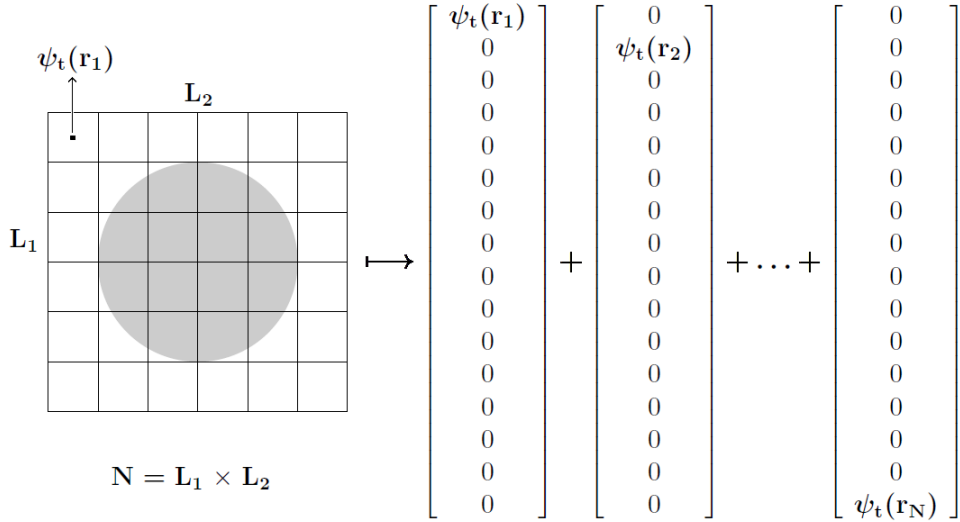


Figure 2.2: The basis function expansion of the total field inside ROI using N pulse basis functions (one for each cell).

frequency ω is a scalar measure of rotation rate. We note that the connection between wavenumber, angular frequency and speed of sound is given with the relation $k = \omega/c$. The speed of sound is constant in the background medium, while it may vary inside the scattering object depending on spatial position \mathbf{r} . Those changes are reflected in the scattering function which can be used to reproduce an image of ROI. The 2-D homogeneous-background Green's function is defined as a response on position \mathbf{r} to a point source positioned at \mathbf{r}' . Its expression in cylindrical coordinates is given as [29]:

$$G_0(\mathbf{r}, \mathbf{r}') = \frac{i}{4} H_0^{(1)}(k_o |\mathbf{r} - \mathbf{r}'|) \quad (2.4)$$

where $H_0^{(1)}$ is the zero-th order Hankel function of the first kind [29] and k_o is the wavenumber of background medium. The Equation (2.2) is difficult to solve because it has two unknowns, the total field $\psi_t(\mathbf{r})$ and the scattering function $s(\mathbf{r})$, making the problem of UT nonlinear and impossible to find a solution analytically.

To solve Equation (2.2) numerically, we first need to discretized it. The square region enclosing the ROI is divided into $N = L_1 \times L_2$ square cells as shown in Figure 2.2. Length ' w ' of one cell is small compared to the sound wavelength λ in the background medium. Changes in the speed of sound and total field inside each cell are negligible. The center of the n^{th} cell is denoted with $\mathbf{r}_n = (x_n, y_n)$, $n = 1, \dots, N$. For the basis function expansion,

we will use pulse basis functions $f_n(\mathbf{r})$ that are defined as:

$$f_n(\mathbf{r}) = f_n(x, y) = \text{rect}\left(\frac{|x - x_n|}{w}\right) \text{rect}\left(\frac{|y - y_n|}{w}\right), \quad (2.5)$$

where the function *rect* is defined as:

$$\text{rect}(x) = \begin{cases} 1, & |x| \leq 1/2 \\ 0, & |x| > 1/2 \end{cases}. \quad (2.6)$$

As presented in Figure 2.2, if point \mathbf{r} is inside the n^{th} cell, then $f_n(\mathbf{r}) = 1$. Otherwise, it is $f_n(\mathbf{r}) = 0$. Using the rectangular pulse basis functions, discrete approximations of scattering function and total field have a constant value over each cell. Another approach is to use sinc basis functions defined as $\text{sinc } x = \frac{\sin(\pi x)}{\pi x}$ [40]. However, we decided to use pulse basis functions because they produce simpler formulas [40] and are reasonably accurate for small pixel dimension [27].

2.2 Forward Model

The goal of the forward model is to calculate the total field inside the ROI from Equation (2.2) using values of the scattering function s . Here, we present the derivation of the linear system of equations that will provide a values for the total field inside ROI.

The basis function expansion of the sub integral function from Equation (2.2), using a finite set of N pulse basis function, is given as:

$$G_0(\mathbf{r}, \mathbf{r}') s(\mathbf{r}') \psi_t(\mathbf{r}') = \sum_{n=1}^N G_0(\mathbf{r}, \mathbf{r}_n) \psi_t(\mathbf{r}_n) s(\mathbf{r}_n) f_n(\mathbf{r}'). \quad (2.7)$$

A variable \mathbf{r}' is an arbitrary position inside ROI and the center of the n^{th} cell is denoted with \mathbf{r}_n . The value of the total field is constant in each cell and it is denoted with $\psi_t(\mathbf{r}_n)$. Then, the double integral from the Lippmann-Schwinger integral equation (2.2) can be transformed as:

$$\begin{aligned}
\iint_R G_0(\mathbf{r}, \mathbf{r}') s(\mathbf{r}') \psi_t(\mathbf{r}') d\mathbf{r}' &= \iint_R \sum_{n=1}^N G_0(\mathbf{r}, \mathbf{r}_n) \psi_t(\mathbf{r}_n) s(\mathbf{r}_n) f_n(\mathbf{r}') d\mathbf{r}' \\
&= \sum_{n=1}^N G_0(\mathbf{r}, \mathbf{r}_n) \psi_t(\mathbf{r}_n) s(\mathbf{r}_n) \iint_R f_n(\mathbf{r}') d\mathbf{r}' \\
&= \sum_{n=1}^N G_0(\mathbf{r}, \mathbf{r}_n) \psi_t(\mathbf{r}_n) s(\mathbf{r}_n) \mathbf{w}^2.
\end{aligned}$$

This leads to new expression for (2.2) given as:

$$\psi_t(\mathbf{r}) = \psi_i(\mathbf{r}) + \mathbf{w}^2 \cdot \sum_{n=1}^N G_0(\mathbf{r}, \mathbf{r}_n) \psi_t(\mathbf{r}_n) s(\mathbf{r}_n). \quad (2.8)$$

The total and incident field can also be written in the form of basis function expansion as:

$$\psi_t = \sum_{j=1}^N \psi_t(\mathbf{r}_j) f_j \quad \text{and} \quad \psi_i = \sum_{j=1}^N \psi_i(\mathbf{r}_j) f_j. \quad (2.9)$$

From Equation (2.8) and (2.9) follows:

$$\begin{aligned}
\sum_{n=1}^N \psi_t(\mathbf{r}_n) f_n &= \sum_{n=1}^N \psi_i(\mathbf{r}_n) f_n + \mathbf{w}^2 \sum_{j=1}^N \sum_{n=1}^N G_0(\mathbf{r}_j, \mathbf{r}_n) \psi_t(\mathbf{r}_n) s(\mathbf{r}_n) \\
\Rightarrow \begin{bmatrix} \psi_t(\mathbf{r}_1) \\ \vdots \\ \psi_t(\mathbf{r}_N) \end{bmatrix} - \mathbf{w}^2 \begin{bmatrix} \sum_{n=1}^N G_0(\mathbf{r}_1, \mathbf{r}_n) \psi_t(\mathbf{r}_n) s(\mathbf{r}_n) \\ \vdots \\ \sum_{n=1}^N G_0(\mathbf{r}_N, \mathbf{r}_n) \psi_t(\mathbf{r}_n) s(\mathbf{r}_n) \end{bmatrix} &= \begin{bmatrix} \psi_i(\mathbf{r}_1) \\ \vdots \\ \psi_i(\mathbf{r}_N) \end{bmatrix} \\
\Rightarrow \begin{bmatrix} \psi_t(\mathbf{r}_1) - \mathbf{w}^2 \sum_{n=1}^N G_0(\mathbf{r}_1, \mathbf{r}_n) \psi_t(\mathbf{r}_n) s(\mathbf{r}_n) \\ \vdots \\ \psi_t(\mathbf{r}_N) - \mathbf{w}^2 \sum_{n=1}^N G_0(\mathbf{r}_N, \mathbf{r}_n) \psi_t(\mathbf{r}_n) s(\mathbf{r}_n) \end{bmatrix} &= \begin{bmatrix} \psi_i(\mathbf{r}_1) \\ \vdots \\ \psi_i(\mathbf{r}_N) \end{bmatrix}.
\end{aligned}$$

We model the wave propagation with Green's functions so in the case when $\mathbf{r} = \mathbf{r}_n$ is true, there is no transmission of energy and we set $G_0(\mathbf{r}, \mathbf{r}_n) = 0$. This leads to:

$$\begin{bmatrix}
\psi_t(\mathbf{r}_1) + \mathbf{w}^2 G_0(\mathbf{r}_1, \mathbf{r}_2) \psi_t(\mathbf{r}_2) s_2 + \cdots + \mathbf{w}^2 G_0(\mathbf{r}_1, \mathbf{r}_N) \psi_t(\mathbf{r}_N) s_N \\
\vdots \\
\psi_t(\mathbf{r}_N) + \mathbf{w}^2 G_0(\mathbf{r}_N, \mathbf{r}_1) \psi_t(\mathbf{r}_1) s_1 + \cdots + \mathbf{w}^2 G_0(\mathbf{r}_N, \mathbf{r}_{N-1}) \psi_t(\mathbf{r}_{N-1}) s_{N-1}
\end{bmatrix} = \begin{bmatrix}
\psi_i(\mathbf{r}_1) \\
\vdots \\
\psi_i(\mathbf{r}_N)
\end{bmatrix}$$

$$\underbrace{\begin{bmatrix}
1 & \mathbf{w}^2 G_0(\mathbf{r}_1, \mathbf{r}_2) s_2 & \cdots & \mathbf{w}^2 G_0(\mathbf{r}_1, \mathbf{r}_N) s_N \\
\vdots & & & \\
\mathbf{w}^2 G_0(\mathbf{r}_N, \mathbf{r}_1) s_1 & \mathbf{w}^2 G_0(\mathbf{r}_N, \mathbf{r}_2) s_2 & \cdots & 1
\end{bmatrix}}_{\mathbf{F}(G_0, s)} \cdot \underbrace{\begin{bmatrix}
\psi_t(\mathbf{r}_1) \\
\vdots \\
\psi_t(\mathbf{r}_N)
\end{bmatrix}}_{\boldsymbol{\psi}_t} = \underbrace{\begin{bmatrix}
\psi_i(\mathbf{r}_1) \\
\vdots \\
\psi_i(\mathbf{r}_N)
\end{bmatrix}}_{\boldsymbol{\psi}_i}$$

where $s_i = -s(\mathbf{r}_i)$ for $i = 1, \dots, N$. The total field is found as a solution of system of linear equations:

$$\mathbf{F}(G_0, s) \boldsymbol{\psi}_t = \boldsymbol{\psi}_i \quad (2.10)$$

where $\boldsymbol{\psi}_t, \boldsymbol{\psi}_i \in \mathbb{C}^{N \times 1}$ are vectors which contain values of total and incident field in each of the cells respectively.

2.3 Inverse Model

The same process of discretization, as in forward model, is used for the inverse model. First, for an arbitrary transducer positioned at $\mathbf{q}_j = (x, y)$, the Equation (2.2) is transformed to:

$$\begin{aligned}
\psi_s(\mathbf{q}_j) &= \psi_t(\mathbf{q}_j) - \psi_i(\mathbf{q}_j) = \iint_R G_0(\mathbf{q}_j, \mathbf{r}) s(\mathbf{r}) \psi_t(\mathbf{r}) \, d\mathbf{r} \\
&= \iint_R \sum_{n=1}^N G_0(\mathbf{q}_j, \mathbf{r}_n) s(\mathbf{r}_n) \psi_t(\mathbf{r}_n) f_n(\mathbf{r}) \, d\mathbf{r} \\
&= \sum_{n=1}^N G_0(\mathbf{q}_j, \mathbf{r}_n) s(\mathbf{r}_n) \psi_t(\mathbf{r}_n) \iint_R f_n(\mathbf{r}) \, d\mathbf{r} \\
&= \mathbf{w}^2 \sum_{n=1}^N G_0(\mathbf{q}_j, \mathbf{r}_n) s(\mathbf{r}_n) \psi_t(\mathbf{r}_n).
\end{aligned}$$

The derived equation holds for all transducers positions \mathbf{q}_j , $j = 1, \dots, M$, that is:

$$\underbrace{\begin{bmatrix} \psi_s(\mathbf{q}_1) \\ \vdots \\ \psi_s(\mathbf{q}_M) \end{bmatrix}}_{\boldsymbol{\psi}_s} = \mathbf{w}^2 \begin{bmatrix} \sum_{n=1}^N G_0(\mathbf{q}_1, \mathbf{r}_n) \psi_t(\mathbf{r}_n) s(\mathbf{r}_n) \\ \vdots \\ \sum_{n=1}^N G_0(\mathbf{q}_M, \mathbf{r}_n) \psi_t(\mathbf{r}_n) s(\mathbf{r}_n) \end{bmatrix} \\ = \mathbf{w}^2 \begin{bmatrix} G_0(\mathbf{q}_1, \mathbf{r}_1) \psi_t(\mathbf{r}_1) & \dots & G_0(\mathbf{q}_1, \mathbf{r}_N) \psi_t(\mathbf{r}_N) \\ \vdots & & \vdots \\ G_0(\mathbf{q}_M, \mathbf{r}_1) \psi_t(\mathbf{r}_1) & \dots & G_0(\mathbf{q}_M, \mathbf{r}_N) \psi_t(\mathbf{r}_N) \end{bmatrix} \cdot \underbrace{\begin{bmatrix} s(\mathbf{r}_1) \\ \vdots \\ s(\mathbf{r}_N) \end{bmatrix}}_{\mathbf{s}}.$$

The coefficients of scattering function (2.3) can be found as a solution of system of linear equations:

$$\mathbf{U}(\mathbf{G}_s, \boldsymbol{\psi}_t) \mathbf{s} = \mathbf{G}_s \text{diag}(\boldsymbol{\psi}_t) \cdot \mathbf{s} = \boldsymbol{\psi}_s \quad (2.11)$$

where $\boldsymbol{\psi}_s \in \mathbb{C}^{M \times 1}$ is a vector that contains values of scattered field received with M transducers. The matrix \mathbf{G}_s is defined as:

$$\mathbf{G}_s = \mathbf{w}^2 \begin{bmatrix} G_0(\mathbf{q}_1, \mathbf{r}_1) & \dots & G_0(\mathbf{q}_1, \mathbf{r}_N) \\ \vdots & \vdots & \vdots \\ G_0(\mathbf{q}_M, \mathbf{r}_1) & \dots & G_0(\mathbf{q}_M, \mathbf{r}_N) \end{bmatrix} \quad (2.12)$$

where $\mathbf{r}_1, \mathbf{r}_2, \dots, \mathbf{r}_N$ are spatial positions of cell's centers in ROI and $\mathbf{q}_1, \mathbf{q}_2, \dots, \mathbf{q}_M$ are positions of M transducers that receive the scattered wave. Since the transducers are located outside ROI, it is always true that $\mathbf{q}_i \neq \mathbf{r}_j$, $i = 1, \dots, M$, $j = 1, \dots, N$. We already mentioned that the problem of UT is nonlinear since both total field and scattering function are unknown.

A basic approach to linearize this problem is to assume that the scattered field, which is produced by the object, is a very small perturbation of the incident field. That is why the total field $\boldsymbol{\psi}_t(\mathbf{r})$ in Equation (2.11) can be replaced by the incident field $\boldsymbol{\psi}_i(\mathbf{r})$ and approximation for the scattering function can be obtained. This approach is called the

Born approximation [5]. However, Born approximation is not good enough for imaging biological tissue because of strong scattering [66].

2.4 Distorted Born Iterative Method

The distorted Born iterative method uses Born approximation to obtain first estimation of the scattering function. Then it iterates between solving the forward and the inverse scattering problem. The method was constructed by Chew and Wang [11] in order to provide a good image reconstruction when Born approximation fails due to its limitations.

Algorithm 1 Algorithm for DBI

- 1: Initialize: $\ell = 0$; $\boldsymbol{\psi}_t^0 = \boldsymbol{\psi}_i$; $G_s^0 = G_0(\mathbf{q}, \mathbf{r})$; $G_d = G_0(\mathbf{r}, \mathbf{r}')$;
 - 2: Calculate Born approximation $\mathbf{s}_e^0 = \mathbf{U}(G_s^0, \psi_t^0)\boldsymbol{\psi}_{s_m}$;
 - 3: **while** RRV $>$ pre-selected threshold **do**
 - 4: $\ell = \ell + 1$;
 - 5: Solve $\mathbf{F}(G_d, \mathbf{s}_e^{\ell-1})(\mathbf{G}_s^\ell)^T = (\mathbf{G}_s^0)^T$ for \mathbf{G}_s^ℓ ;
 - 6: Solve $\mathbf{F}(G_d, \mathbf{s}_e^{\ell-1})\boldsymbol{\psi}_t^\ell = \boldsymbol{\psi}_i$ for $\boldsymbol{\psi}_t^\ell$;
 - 7: Calculate $\boldsymbol{\psi}_{s_e}^\ell = \mathbf{U}(G_s^\ell, \psi_t^\ell)\mathbf{s}_e^{\ell-1}$;
 - 8: Solve $\mathbf{U}(G_s^\ell, \psi_t^\ell)\Delta\mathbf{s}^\ell = \boldsymbol{\psi}_{s_m} - \boldsymbol{\psi}_{s_e}^\ell$ for $\Delta\mathbf{s}^\ell$;
 - 9: Set $\mathbf{s}_e^\ell = \mathbf{s}_e^{\ell-1} + \Delta\mathbf{s}^\ell$;
 - 10: Calculate RRV;
 - 11: **end while**
-

In each iteration of the method, the scattering function is updated by a correction factor. The new scattering function is then used to update the total field and the Green's function. The iterations continue until the residual error is below a predefined threshold. The following steps illustrate the detailed process of the DBI:

1) To initialize the problem, first use Born approximation to set the total field to be the incident field as $\boldsymbol{\psi}_t^0 = \boldsymbol{\psi}_i$. We denote the total field for the ℓ^{th} iteration as $\boldsymbol{\psi}_t^\ell$. Throughout the execution of the algorithm, the value of the total field $\boldsymbol{\psi}_t^\ell$ should be updated for every iteration. Let the Green's function for the inverse model of the first iteration to be \mathbf{G}_s^0 , where $\mathbf{G}_s^0 = \mathbf{G}_0(\mathbf{q}, \mathbf{r})$ according to the relation defined in Equation

(2.4). Use the homogeneous Green's function \mathbf{G}_0 to solve for the first estimated scattering function \mathbf{s}_e^0 as shown in line 2 in the Algorithm 1, where $\boldsymbol{\psi}_{sm}$ is the value of the scattered field measured at transducers. In the Algorithm 1, \mathbf{G}_d is the forward model's Green's function $\mathbf{G}_0(\mathbf{r}, \mathbf{r}')$, and \mathbf{G}_s^ℓ is the inverse model's Green's function $\mathbf{G}(\mathbf{q}, \mathbf{r})$ of the ℓ^{th} iteration.

2) Since the Green's functions satisfy the same Helmholtz equation as the total field [11], [42], the same matrix \mathbf{F} from the forward model, Equation (2.10), that updates incident field to the total field, is used to find updated inverse model of the Green's function \mathbf{G}_s^ℓ as:

$$\mathbf{F}(\mathbf{G}_d, \mathbf{s}_e^{\ell-1})(\mathbf{G}_s^\ell)^T = (\mathbf{G}_s^0)^T. \quad (2.13)$$

Here \mathbf{s}_e^ℓ is the scattering function for the ℓ^{th} iteration.

3) Solve the forward problem using Equation (2.10) for the new approximation of the total field:

$$\mathbf{F}(\mathbf{G}_d, \mathbf{s}_e^{\ell-1})\boldsymbol{\psi}_t^\ell = \boldsymbol{\psi}_i, \quad (2.14)$$

and solve the inverse problem for the estimated scattered field:

$$\boldsymbol{\psi}_{s_e}^\ell = \mathbf{U}(\mathbf{G}_s^\ell, \boldsymbol{\psi}_t^\ell)\mathbf{s}_e^{\ell-1}. \quad (2.15)$$

4) Solve for the correction factor $\Delta\mathbf{s}_e^\ell$ of the scattering function by solving the inverse problem:

$$\mathbf{U}(\mathbf{G}_s^\ell, \boldsymbol{\psi}_t^\ell)\Delta\mathbf{s}_e^\ell = \boldsymbol{\psi}_{sm} - \boldsymbol{\psi}_{s_e}^\ell \quad (2.16)$$

where $\boldsymbol{\psi}_{sm}$ and $\boldsymbol{\psi}_{s_e}^{\ell-1}$ are the measured and the estimated scattered field respectively. The justification for the Equation (2.16) is following: from Equations (2.11) and (2.15), under assumption that measured scattered field $\boldsymbol{\psi}_{sm}$ is exact, we have:

$$\mathbf{s} = \mathbf{U}(\mathbf{G}_s, \boldsymbol{\psi}_t)^{-1}\boldsymbol{\psi}_{sm} \quad \text{and} \quad \mathbf{s}_e^{\ell-1} = \mathbf{U}(\mathbf{G}_s^\ell, \boldsymbol{\psi}_t^\ell)^{-1}\boldsymbol{\psi}_{s_e}^\ell.$$

Using approximation $\mathbf{U}(\mathbf{G}_s, \boldsymbol{\psi}_t) \approx \mathbf{U}(\mathbf{G}_s^\ell, \boldsymbol{\psi}_t^\ell)$ and subtracting previous two equations, we have

$$\mathbf{s} - \mathbf{s}_e^{\ell-1} = \mathbf{U}(\mathbf{G}_s^\ell, \boldsymbol{\psi}_t^\ell)^{-1}(\boldsymbol{\psi}_{sm} - \boldsymbol{\psi}_{s_e}^\ell).$$

The goal of DBI method is that the new estimate \mathbf{s}_e^ℓ for the scattering function is closer to the exact \mathbf{s} than the previous estimate $\mathbf{s}_e^{\ell-1}$. That is why the update $\Delta\mathbf{s}_e^\ell$ is calculated from (2.16). Then, use the update to find better estimate for the scattering function:

$$\mathbf{s}_e^\ell = \mathbf{s}_e^{\ell-1} + \Delta\mathbf{s}_e^\ell. \quad (2.17)$$

5) Calculate the relative residual value (RRV) for the estimation of the scattered field $\psi_{s_e}^\ell$ at the ℓ^{th} iteration as:

$$\text{RRV} = \frac{\sum_{n=1}^M |\psi_{s_m}^i(\mathbf{r}_n) - \psi_{s_e}^\ell(\mathbf{r}_n)|}{\sum_{n=1}^M |\psi_{s_m}(\mathbf{r}_n)|} \quad (2.18)$$

to test the convergence of the DBI method. The iterations will continue by going back to step 2) until the algorithm converges.

2.5 Simulation of Ultrasound Tomography

The efficiency of regularization methods presented in this dissertation is tested on the simulation of UT. So, in this section we describe a general guidelines of our simulations.

We simulate M equidistant transducers surrounding the ROI as shown in Figure 2.1. We have M_t out of M transducers acting as transmitters, that is, they are emitting the ultrasound wave at known frequency f , one at a time. The frequencies used in simulations are 500 kHz, 1 MHz or 2 MHz, similar to those reported in [20], [29] and [42]. All M transducers are used for receiving the echo data in the full aperture setting.

Different phantom are used for reconstructions in simulations, some of them are shown in Figures 4.1, 5.3 and 6.7. The Modified Shepp-Logan and simulated phantoms were created using Matlab routine 'phantom', while the Matlab data for the breast phantoms were extracted from the database [51]. Values of the exact scattering function \mathbf{s} are calculated using the Equation (2.3). The speed of sound in the background medium is 1480 m/s, as in water, and the values of aforementioned phantoms are the percentage increase over the background medium.

We note that the realistic experimental setting directly use measurement of the scattered field received by transducers to calculate the discrepancy from the estimated scattered field. However, in our simulations, we used the exact scattering function to calculate the exact total field $\boldsymbol{\psi}_t$ and the Green's functions \mathbf{G}_s in inhomogeneous medium. Then, using Equation (2.11), we calculated $\boldsymbol{\psi}_s = \mathbf{U}(G_s, \boldsymbol{\psi}_t)\mathbf{s}$. A Gaussian white noise with signal to noise ratio between 20, 25 or 30 dB, depending on the case, was added on $\boldsymbol{\psi}_s$ to mimic the realistic settings. This process was done only in the beginning to obtain "measured" scattered fields with different noise levels. Similar noise levels were used in [29] and [42]. We also want to emphasize that in the reconstruction process, the incident field $\boldsymbol{\psi}_i$ will be used instead of $\boldsymbol{\psi}_t$ and the Green's function \mathbf{G}_s will be replaced by \mathbf{G}_0 in homogeneous medium. The zero-th order Hankel function from Equation (2.4) were calculated using Matlab routine 'besselh'.

The focus of this dissertation is on solving the inverse problem where the system of linear equations $\mathbf{G}_s \text{diag}(\boldsymbol{\psi}) \cdot \Delta\mathbf{s} = \Delta\boldsymbol{\psi}_s$ is ill-posed. The update for each pixel is corresponding to each component of the vector $\Delta\mathbf{s}$, making it N components. The dimension of matrix $\mathbf{G}_s \text{diag}(\boldsymbol{\psi}_t)$ is $M \times N$ and the vector $\Delta\boldsymbol{\psi}_s$ has M components, that is, system $\mathbf{G}_s \text{diag}(\boldsymbol{\psi}_t) \cdot \Delta\mathbf{s} = \Delta\boldsymbol{\psi}_s$ is underdetermined.

To overcome this lack of data (M is often much less than N), a sound wave emission from M_t different equidistant positions is simulated, leading to M_t underdetermined systems $\mathbf{G}_s \text{diag}(\boldsymbol{\psi}_t)^{(\ell)} \cdot \Delta\mathbf{s} = \Delta\boldsymbol{\psi}_s^{(\ell)}$, $\ell = 1, \dots, M_t$. Instead of solving each underdetermined system individually, we construct the overdetermined system

$$\begin{pmatrix} \mathbf{G}_s \text{diag}(\boldsymbol{\psi}_t)^{(1)} \\ \vdots \\ \mathbf{G}_s \text{diag}(\boldsymbol{\psi}_t)^{(M_t)} \end{pmatrix} \cdot \Delta\mathbf{s} = \begin{pmatrix} \Delta\boldsymbol{\psi}_s^{(1)} \\ \vdots \\ \Delta\boldsymbol{\psi}_s^{(M_t)} \end{pmatrix} \Rightarrow \mathbf{G}_s \text{diag}(\boldsymbol{\psi}_t) \cdot \Delta\mathbf{s} = \Delta\boldsymbol{\psi}_s$$

\Rightarrow Trough the rest of this dissertation we will use new labels for the system: $\mathbf{X}\mathbf{y} = \mathbf{b}$,

where $\mathbf{X} \in \mathbb{C}^{(M_t \cdot M) \times N}$ and $\mathbf{b} \in \mathbb{C}^{(M_t \cdot M)}$. This problem is ill-posed and a regularization method is necessary to solve it. Possible ways to solve this problem are described in this dissertation.

Chapter 3

Preliminaries

In this chapter we state a basic results from the field of numerical linear algebra regarding the singular value decomposition (SVD), the generalized singular value decomposition (GSVD) and the least squares problem. These mathematical tools are used extensively trough the rest of this dissertation. The definitions and theorems listed below can be found in [12], [36], [67] and [68]. Main theorems are given without proof. Basic mathematical terms for an arbitrary vector $\mathbf{y} \in \mathbb{C}^\ell$ and matrix $\mathbf{X} \in \mathbb{C}^{q \times \ell}$ that are used in this dissertation are the following:

- The **norm** ℓ_2 of vector \mathbf{y} is given as $\|\mathbf{y}\|_2 = \sqrt{\sum_{i=1}^{\ell} |y_i|^2}$.
- The **inner product** of two vectors $\mathbf{y}, \mathbf{z} \in \mathbb{C}^\ell$ is given as $(\mathbf{y}, \mathbf{z}) = \mathbf{y}^* \mathbf{z} = \sum_{i=1}^{\ell} y_i \bar{z}_i$. In addition, the norm ℓ_2 can be defined using inner product as $\|\mathbf{y}\|_2 = \sqrt{(\mathbf{y}, \mathbf{y})}$.
- **Norm-2** of matrix \mathbf{X} is given as $\|\mathbf{X}\|_2 = \max_{\mathbf{y} \neq \mathbf{0}} \frac{\|\mathbf{X}\mathbf{y}\|_2}{\|\mathbf{y}\|_2}$. In addition, it holds $\|\mathbf{X}\mathbf{y}\|_2 \leq \|\mathbf{X}\|_2 \|\mathbf{y}\|_2$.
- **Frobenius norm** of matrix \mathbf{X} is given as $\|\mathbf{X}\|_F = \sqrt{\sum_{i=1}^q \sum_{j=1}^{\ell} |x_{ij}|^2}$.
- **Range** of matrix \mathbf{X} is given as $\mathcal{R}(\mathbf{X}) = \text{span}\{\mathbf{x}_1, \dots, \mathbf{x}_\ell\}$. That is, range of matrix \mathbf{X} is equal to the set of all linear combinations of columns of matrix \mathbf{X} .

- The **rank** of matrix \mathbf{X} is the number of linear independent columns of matrix \mathbf{X} , that is $rank(\mathbf{X}) = \dim \mathcal{R}(\mathbf{X})$. In addition, it holds $rank(\mathbf{X}) = rank(\mathbf{X}^T)$.
- A matrix \mathbf{X} has **full row rank** if its rank is equal to the number of rows, that is $rank(\mathbf{X}) = q$.
- The **null space** of matrix \mathbf{X} is given as $\mathcal{N}(\mathbf{X}) = \{\mathbf{y} \in \mathbb{C}^\ell \mid \mathbf{X}\mathbf{y} = \mathbf{0}\}$.
- A matrix \mathbf{X} is called **left orthogonal** if it holds $\mathbf{X}^*\mathbf{X} = \mathbf{I}$, where \mathbf{I} is the identity matrix. A square matrix \mathbf{X} is called **unitary** if it holds $\mathbf{X}^*\mathbf{X} = \mathbf{X}\mathbf{X}^* = \mathbf{I}$.
- For any unitary matrix \mathbf{X} holds $\|\mathbf{X}\mathbf{y}\|_2 = \|\mathbf{y}\|_2$ and $\|\mathbf{X}\|_2 = 1$.
- A **trace** of square matrix $\mathbf{A} \in \mathbb{R}^{n \times n}$ is given as $trace(\mathbf{A}) = \sum_{i=1}^n a_{ii}$.
- Let $\mathbf{X} \in \mathbb{C}^{n \times n}$ and $\mathbf{y} \in \mathbb{C}^n$, $\mathbf{y} \neq \mathbf{0}$. If there exist scalar λ that satisfies $\mathbf{X}\mathbf{y} = \lambda\mathbf{y}$, then \mathbf{y} is an eigenvector and λ is an eigenvalue of matrix \mathbf{X} .
- If the product $\mathbf{A} \cdot \mathbf{B}$ is defined, then $(\mathbf{A} \cdot \mathbf{B})^* = \mathbf{B}^* \cdot \mathbf{A}^*$.
- If matrices $\mathbf{A}, \mathbf{B} \in \mathbb{C}^{n \times n}$ are regular then $(\mathbf{A} \cdot \mathbf{B})^{-1} = \mathbf{B}^{-1} \cdot \mathbf{A}^{-1}$.
- If $\mathbf{A} \in \mathbb{C}^{n \times n}$ is a nonsingular matrix, then $(\mathbf{A}^{-1})^* = (\mathbf{A}^*)^{-1}$.
- If \mathbf{D} is a diagonal matrix with real entries, then $\mathbf{D}^* = \mathbf{D}$.
- If \mathbf{D}_1 and \mathbf{D}_2 are diagonal matrices of same size, then $\mathbf{D}_1\mathbf{D}_2 = \mathbf{D}_2\mathbf{D}_1$.

3.1 Singular Value Decomposition

Singular Value Decomposition (SVD) is one of the most important matrix factorization. It exists for all matrices regardless of their type. Using SVD, the given matrix \mathbf{X} is decomposed into product of two unitary and one diagonal matrix. Using this decomposition, a valuable informations about rank, range and null space of given matrix \mathbf{X} can be easily obtained. A formal definition of SVD is provided with the following theorem.

Theorem 3.1.1 (SVD, Theorem 3.2 in [12]). *Let $\mathbf{X} \in \mathbb{C}^{q \times \ell}$, $q > \ell$, be an arbitrary matrix. Then, there exist unitary matrices $\mathbf{U} \in \mathbb{C}^{q \times q}$, $\mathbf{V} \in \mathbb{C}^{\ell \times \ell}$ and matrix $\mathbf{\Sigma} = \text{diag}(\sigma_1, \sigma_2, \dots, \sigma_\ell)$, $\sigma_1 \geq \sigma_2 \geq \dots \geq \sigma_\ell \geq 0$, such that*

$$\mathbf{X} = \mathbf{U} \begin{pmatrix} \mathbf{\Sigma} \\ \mathbf{0} \end{pmatrix} \mathbf{V}^*. \quad (3.1)$$

We refer to Equation (3.1) as a singular value decomposition of matrix \mathbf{X} . Columns of matrices \mathbf{U} and \mathbf{V} are left and right singular vectors respectively and σ_i , $i = 1, \dots, \ell$ are singular values. □

When notation

$$\mathbf{U} = \begin{pmatrix} \mathbf{u}_1 & \mathbf{u}_2 & \dots & \mathbf{u}_q \end{pmatrix} \quad (3.2)$$

and

$$\mathbf{V} = \begin{pmatrix} \mathbf{v}_1 & \mathbf{v}_2 & \dots & \mathbf{v}_\ell \end{pmatrix}, \quad (3.3)$$

is introduced, then the matrix \mathbf{X} can be written as a sum of rank-one matrices, that is:

$$\mathbf{X} = \sum_{i=1}^{\ell} \sigma_i \mathbf{u}_i \mathbf{v}_i^*. \quad (3.4)$$

If the last $q - \ell$ columns of matrix \mathbf{U} from Theorem 3.1.1 are omitted, then it holds $\mathbf{U}^* \mathbf{U} = \mathbf{I}$ and $\mathbf{U} \mathbf{U}^* \neq \mathbf{I}$. When SVD of the matrix \mathbf{X} is calculated, then the following informations can be obtained:

1. If r is the number of nonzero singular values, then $\text{rank}(\mathbf{X}) = r$.
2. $\mathcal{R}(\mathbf{X}) = \text{span} \{ \mathbf{u}_1, \dots, \mathbf{u}_r \}$
3. $\mathcal{N}(\mathbf{X}) = \text{span} \{ \mathbf{v}_{r+1}, \dots, \mathbf{v}_\ell \}$
4. $\|\mathbf{X}\|_2 = \sigma_1$
5. $\|\mathbf{X}\|_F^2 = \sigma_1^2 + \sigma_2^2 + \dots + \sigma_\ell^2$
6. The condition number of matrix \mathbf{X} in ℓ_2 norm is $\kappa_2(\mathbf{X}) = \sigma_1 / \sigma_\ell$.

In addition, the best lower rank approximation of the matrix \mathbf{X} can be found using its SVD as stated with the following theorem [67].

Theorem 3.1.2 (Eckart-Young-Mirsky Theorem). *Let $\mathbf{X} \in \mathbb{C}^{q \times \ell}$ be an arbitrary matrix of a rank r . For $k < r$ we define*

$$\mathbf{X}_k = \sum_{i=1}^k \sigma_i \cdot \mathbf{u}_i \mathbf{v}_i^*. \quad (3.5)$$

Then

- 1.) $\|\mathbf{X} - \mathbf{X}_k\|_2 = \inf_{\text{rank}(A) < k} \|\mathbf{X} - \mathbf{A}\|_2 = \sigma_{k+1}$
- 2.) $\|\mathbf{X} - \mathbf{X}_k\|_F = \inf_{\text{rank}(A) < k} \|\mathbf{X} - \mathbf{A}\|_F = \sqrt{\sigma_{k+1}^2 + \sigma_{k+2}^2 + \dots + \sigma_r^2}$.

□

A Moore-Penrose pseudoinverse of a matrix $\mathbf{X} \in \mathbb{C}^{q \times \ell}$ is a matrix with ℓ rows and q columns, denoted with \mathbf{X}^\dagger , which satisfies four Penrose conditions [67]:

1. $\mathbf{X}\mathbf{X}^\dagger\mathbf{X} = \mathbf{X}$
2. $\mathbf{X}^\dagger\mathbf{X}\mathbf{X}^\dagger = \mathbf{X}^\dagger$
3. $(\mathbf{X}\mathbf{X}^\dagger)^* = \mathbf{X}\mathbf{X}^\dagger$
4. $(\mathbf{X}^\dagger\mathbf{X})^* = \mathbf{X}^\dagger\mathbf{X}$.

When SVD of a matrix \mathbf{X} is obtained, its Moore-Penrose pseudoinverse can be found as:

$$\mathbf{X}^\dagger = \mathbf{V} \begin{pmatrix} \boldsymbol{\Sigma}^{-1} & \mathbf{0} \end{pmatrix} \mathbf{U}^* = \sum_{i=1}^{\ell} \frac{1}{\sigma_i} \mathbf{v}_i \mathbf{u}_i^*. \quad (3.6)$$

3.2 Least Squares Problem

A very common problem in the field of numerical linear algebra is to solve an overdetermined linear system

$$\mathbf{X}\mathbf{y} = \mathbf{b}, \quad \mathbf{X} \in \mathbb{C}^{q \times \ell}, \quad \mathbf{b} \in \mathbb{C}^q, \quad q > \ell. \quad (3.7)$$

Standard approach to solve it is to find its least squares solution.

A vector $\mathbf{y} \in \mathbb{C}^\ell$ is called a least squares solution of (3.7) if it satisfies [12]:

$$\|\mathbf{X}\mathbf{y} - \mathbf{b}\|_2 = \min_{\mathbf{z} \in \mathbb{C}^\ell} \|\mathbf{X}\mathbf{z} - \mathbf{b}\|_2. \quad (3.8)$$

The following theorem gives one way to find minimum norm least squares solution of 3.7 using Moore-Penrose pseudoinverse [57].

Theorem 3.2.1 (Minimum norm least squares solution). *Let $\mathbf{X} \in \mathbb{C}^{q \times \ell}$ be an arbitrary matrix of rank r and $\mathbf{X} = \mathbf{U} \begin{pmatrix} \boldsymbol{\Sigma} \\ \mathbf{0} \end{pmatrix} \mathbf{V}^*$ its singular value decomposition. The minimum norm least squares solution of the equation $\mathbf{X}\mathbf{y} = \mathbf{b}$ is given as $\mathbf{y} = \mathbf{X}^\dagger \mathbf{b}$ where \mathbf{X}^\dagger is the Moore-Penrose pseudoinverse (3.6).*

Proof. Columns of matrix \mathbf{V} form an orthogonal basis for the vector space \mathbb{C}^ℓ . That is why vector $\mathbf{y} \in \mathbb{C}^\ell$ can be written as a linear combination

$$\mathbf{y} = \sum_{i=1}^{\ell} d_i \mathbf{v}_i = \mathbf{V} \mathbf{d} \quad (3.9)$$

where the vector \mathbf{d} is given as $\mathbf{d} = \begin{pmatrix} d_1 & d_2 & \dots & d_\ell \end{pmatrix}^T$. We denote elements of vector $\mathbf{U}^* \mathbf{b}$ with g_i , that is $\mathbf{U}^* \mathbf{b} = \begin{pmatrix} g_1 & g_2 & \dots & g_q \end{pmatrix}^T$ and compute

$$\begin{aligned} \|\mathbf{X}\mathbf{y} - \mathbf{b}\|_2^2 &= \|\mathbf{U}\boldsymbol{\Sigma}\mathbf{V}^* \cdot \mathbf{V}\mathbf{d} - \mathbf{U}\mathbf{U}^* \mathbf{b}\|_2^2 \\ &= \|\mathbf{U}(\boldsymbol{\Sigma}\mathbf{d} - \mathbf{U}^* \mathbf{b})\|_2^2 = \|\boldsymbol{\Sigma}\mathbf{d} - \mathbf{U}^* \mathbf{b}\|_2^2 \\ &= \sum_{i=1}^r (\sigma_i d_i - g_i)^2 + \sum_{i=r+1}^q (g_i)^2. \end{aligned}$$

It is obvious that the value of expression $\|\mathbf{X}\mathbf{y} - \mathbf{b}\|_2^2$ is minimal when $d_i = \frac{g_i}{\sigma_i}$, for $i = 1, \dots, r$. Then the vector \mathbf{y} is given as:

$$\mathbf{y} = \mathbf{V} \cdot \begin{pmatrix} \frac{g_1}{\sigma_1} & \dots & \frac{g_r}{\sigma_r} & g_{r+1} & \dots & g_\ell \end{pmatrix}^T. \quad (3.10)$$

The smallest norm of the solution $\|\mathbf{y}\|_2$ is achieved when $g_i = 0$ for $r < i \leq \ell$, so the minimum least squares solution is uniquely determined by the formula

$$\mathbf{y} = \mathbf{X}^\dagger \mathbf{b} = \mathbf{V} \boldsymbol{\Sigma}^{-1} \mathbf{U}^* \mathbf{b} = \sum_{i=1}^{\ell} \frac{\mathbf{u}_i^* \mathbf{b}}{\sigma_i} \mathbf{v}_i. \quad (3.11)$$

□

If matrix \mathbf{X} has a large condition number and its singular values are decreasing and approaching to zero, then the linear system (3.7) is ill-posed [33]. This means that small errors in the vector \mathbf{b} produce large errors in the least squares solution \mathbf{y} when it is calculated using Equation (3.11).

The following example shows how small singular values of matrix \mathbf{X} can have detrimental effect on the least squares solution when a "measured" vector $\tilde{\mathbf{b}}$ given with noise is used in calculations instead of exact vector \mathbf{b} .

Example 3.2.2. We want to solve a linear system $\mathbf{X}\mathbf{y} = \tilde{\mathbf{b}}$ where the matrix \mathbf{X} is given as:

$$\mathbf{X} = \begin{pmatrix} 0.081926788634506 & -0.002027961639074 & 0.097447639682838 \\ 0.085216023638418 & -0.002109057544086 & 0.101361200841502 \\ 0.040440069687235 & -0.001001013837422 & 0.048101164945327 \\ 0.030841167295902 & -0.000763767640783 & 0.036683103427746 \end{pmatrix}.$$

The vector $\tilde{\mathbf{b}} = \begin{pmatrix} 0.017734973960188 \\ 0.018446991332726 \\ 0.008753835370936 \\ 0.006676776098835 \end{pmatrix}$ contains a normally distributed noise with zero

mean and the variance equal to 10^{-6} . This results in relative error of vector $\tilde{\mathbf{b}}$, defined as $\frac{\|\tilde{\mathbf{b}}-\mathbf{b}\|_2}{\|\mathbf{b}\|_2}$, to be equal to $3 \cdot 10^{-5}$. The exact least squares solution of linear system $\mathbf{X}\mathbf{y} = \mathbf{b}$

is $\mathbf{y} = \begin{pmatrix} 0.1 \\ 0.1 \\ 0.1 \end{pmatrix}$. However, in order to find least squares solution using Equation (3.11),

we calculate SVD of matrix \mathbf{X} using Matlab routine 'svd'. The calculated singular values of matrix \mathbf{X} are 0.2, 10^{-6} and 10^{-7} , and left and right singular vectors are columns of matrices

$$\mathbf{U} = \begin{pmatrix} -0.636634781567791 & -0.231599658895989 & -0.187418253983662 & -0.711289076937856 \\ -0.662199211796307 & 0.593197818576590 & 0.335964091025294 & 0.311025210350983 \\ -0.314250033176460 & -0.216454155047623 & -0.744445543997357 & 0.547900855478153 \\ -0.239656578134369 & -0.740017259797268 & 0.545713624200223 & 0.311666199837785 \end{pmatrix},$$

and

$$\mathbf{V} = \begin{pmatrix} -0.643435043666662 & -0.674197593975200 & -0.362558890195417 \\ 0.015926488646733 & 0.461730483459696 & -0.886877278772808 \\ -0.765335019152440 & 0.576422210642622 & 0.286355973461018 \end{pmatrix}.$$

Then, the least squares solution, calculated using Equation (3.11), is given as

$$\tilde{\mathbf{y}} = \begin{pmatrix} -1.514138612128782 \\ -4.838235661915373 \\ 1.354283113338196 \end{pmatrix}. \quad (3.12)$$

Then, the relative error of vector $\tilde{\mathbf{y}}$ is $\frac{\|\mathbf{y} - \tilde{\mathbf{y}}\|_2}{\|\tilde{\mathbf{y}}\|_2} = 1.018524800497955$.

The problem when a least squares solution is obtained with Equation (3.11) is its sensitivity to even relatively small noise on vector \mathbf{b} . One of the reasons is that singular vectors, which corresponds to smaller singular values, tend to have more sign changes in their elements [34]. Then, when singular values are inverted, as seen in Equation (3.11), influence of these singular vectors on the least squares solution is increased, resulting in high relative errors.

A regularization method, which decreases the influence of smaller singular values and corresponding singular vectors, is necessary in order to produce acceptable solution for the linear system (3.7). More on regularization methods is explained in Chapter 4.

3.2.1 Regularization matrix \mathbf{L}

Common practice for solving an ill-posed linear system (3.7), when vector \mathbf{b} is given with errors, is adding the constraint on the solution \mathbf{y} using a regularization matrix \mathbf{L} . It is required that matrix \mathbf{L} has a full row rank. The problem 3.7 is modified to

$$\mathbf{X}\mathbf{y} = \mathbf{b} \quad \text{s.t.} \quad \|\mathbf{L}\mathbf{y}\|_2 \leq \delta \quad (3.13)$$

where the value for δ is a priori known. In the term of least squares problem, similarly as defined in Equation (3.8), a least squares solution of 3.13 for an unknown and relatively small δ can be defined as:

$$\left\| \begin{pmatrix} \mathbf{X} \\ \mathbf{L} \end{pmatrix} \mathbf{y} - \begin{pmatrix} \mathbf{b} \\ \mathbf{0} \end{pmatrix} \right\|_2 = \min_{\mathbf{z} \in \mathbb{C}^\ell} \left\| \begin{pmatrix} \mathbf{X} \\ \mathbf{L} \end{pmatrix} \mathbf{z} - \begin{pmatrix} \mathbf{b} \\ \mathbf{0} \end{pmatrix} \right\|_2. \quad (3.14)$$

The regularization matrix \mathbf{L} can be beneficial when dealing with noisy data. Common choices for this matrix are discrete versions of the first or second order derivative operator

given as:

$$\mathbf{L}_1 = \frac{1}{2} \begin{pmatrix} 1 & -1 & 0 & \dots & 0 \\ 0 & 1 & -1 & \dots & 0 \\ & & \ddots & \ddots & \\ 0 & \dots & 0 & 1 & -1 \end{pmatrix} \in \mathbb{R}^{(\ell-1) \times \ell} \quad (3.15)$$

and

$$\mathbf{L}_2 = \frac{1}{4} \begin{pmatrix} -1 & 2 & -1 & 0 & \dots & 0 \\ 0 & -1 & 2 & -1 & \dots & 0 \\ & & \ddots & \ddots & \ddots & \\ 0 & \dots & 0 & -1 & 2 & -1 \end{pmatrix} \in \mathbb{R}^{(\ell-2) \times \ell}. \quad (3.16)$$

They are supposed to impose smoothness on the solution of (3.13). Null spaces of these matrices are given with:

$$\mathcal{N}(\mathbf{L}_1) = \text{span} \left\{ \begin{pmatrix} 1 \\ \vdots \\ 1 \end{pmatrix} \right\} \quad \text{and} \quad \mathcal{N}(\mathbf{L}_2) = \text{span} \left\{ \begin{pmatrix} 1 \\ \vdots \\ 1 \end{pmatrix}, \begin{pmatrix} 1 \\ \vdots \\ \ell \end{pmatrix} \right\} \quad (3.17)$$

However, the choice of matrix \mathbf{L} is not limited to aforementioned options and different matrices can be constructed to suite better the nature of the problem.

The problem of constructing regularization matrices has been discussed in literature before. Calvetti et al. in [6] modified the matrices \mathbf{L}_1 and \mathbf{L}_2 to the square invertible matrices $\tilde{\mathbf{L}}_1$ and $\tilde{\mathbf{L}}_2 \in \mathbb{R}^{\ell \times \ell}$ defined as:

$$\tilde{\mathbf{L}}_1 = \frac{1}{2} \begin{pmatrix} 1 & -1 & 0 & \dots & 0 \\ 0 & 1 & -1 & \dots & 0 \\ & & \ddots & \ddots & \\ 0 & \dots & 0 & 1 & -1 \\ 0 & \dots & 0 & 0 & 10^{-8} \end{pmatrix} \quad \text{and} \quad \tilde{\mathbf{L}}_2 = \frac{1}{4} \begin{pmatrix} 2 & -1 & 0 & 0 & \dots & 0 \\ -1 & 2 & -1 & 0 & \dots & 0 \\ 0 & -1 & 2 & -1 & \dots & 0 \\ & & \ddots & \ddots & \ddots & \\ 0 & \dots & 0 & -1 & 2 & -1 \\ 0 & \dots & 0 & 0 & -1 & 2 \end{pmatrix}$$

and used their inverses as preconditioners for the iterative methods GMRES, RRGMRRES and LSQR. New ways to construct square invertible regularization matrices for large-scale minimization problems that allow inexpensive computation of the matrix vector product

are shown in [13]. Their transformations based on given boundary conditions are given in [14]

Since the focus of dissertation is the regularization of the inverse problem in ultrasound tomography, there are some known facts which can be used to modify original matrices \mathbf{L}_1 or \mathbf{L}_2 . Specifically, the reproduced image consists of a scattering object surrounded with the background medium. Since the values of pixels that represent background medium are equal to zero (more on this is explained in Chapter 2), we can impose boundary conditions. That is why in some of our tests we use modification of matrix \mathbf{L}_1 given as:

$$\mathbf{L} = \frac{1}{2} \begin{pmatrix} 10^{-5} & 0 & 0 & \dots & 0 & 0 \\ 0 & 1 & -1 & \dots & 0 & 0 \\ & & \ddots & \ddots & & \\ 0 & \dots & 0 & 1 & -1 & 0 \\ 0 & \dots & 0 & 0 & 0 & 10^{-5} \end{pmatrix} \in \mathbb{R}^{(\ell-1) \times \ell} \quad (3.18)$$

with null space

$$\mathcal{N}(\mathbf{L}) = \text{span} \left\{ \begin{pmatrix} 0 \\ 1 \\ \vdots \\ 1 \\ 0 \end{pmatrix} \right\} \quad (3.19)$$

3.3 Generalized Singular Value Decomposition

Generalized Singular Value Decomposition (GSVD), described in [24], [60] and [70], is generalizing the idea of SVD for one matrix to the matrix pair (\mathbf{X}, \mathbf{L}) . For GSVD to be defined, matrices $\mathbf{X} \in \mathbb{C}^{q \times \ell}$ and $\mathbf{L} \in \mathbb{C}^{p \times \ell}$, $q \geq \ell \geq p$, must satisfy two conditions:

1. \mathbf{L} has full row rank, that is $\text{rank}(\mathbf{L}) = p$, and same number of columns as \mathbf{X} .
2. $\mathcal{N}(\mathbf{X}) \cap \mathcal{N}(\mathbf{L}) = \{0\}$

where $\mathcal{N}(\cdot)$ denotes a null space of matrix. These two conditions are equivalent to the condition $\text{rank} \begin{pmatrix} \mathbf{X} \\ \mathbf{L} \end{pmatrix} = \ell$. Because of that they are necessary for the uniqueness of

the solution for problem 3.13. The following theorem gives a formal definition for GSVD of matrix pair [70].

Theorem 3.3.1 (GSVD). *Let matrix pair (\mathbf{X}, \mathbf{L}) satisfies two aforementioned conditions. Then there exist left orthogonal matrix $\mathbf{U} \in \mathbb{C}^{q \times \ell}$, unitary matrix $\mathbf{V} \in \mathbb{C}^{p \times p}$, and a nonsingular matrix $\mathbf{Y} \in \mathbb{C}^{\ell \times \ell}$ such that*

$$\mathbf{X} = \mathbf{U} \begin{pmatrix} \mathbf{D}_{\mathbf{X}} & 0 \\ 0 & \mathbf{I}_{\ell-p} \end{pmatrix} \mathbf{Y}^{-1} \quad (3.20)$$

$$\mathbf{L} = \mathbf{V} \begin{pmatrix} \mathbf{D}_{\mathbf{L}} & 0 \end{pmatrix} \mathbf{Y}^{-1}. \quad (3.21)$$

The diagonal elements of matrices $\mathbf{D}_{\mathbf{X}} = \text{diag}(\alpha_1, \alpha_2, \dots, \alpha_p)$ and $\mathbf{D}_{\mathbf{L}} = \text{diag}(\beta_1, \beta_2, \dots, \beta_p)$ satisfy the relations

$$0 \leq \alpha_1 \leq \alpha_2 \leq \dots \leq \alpha_p \leq 1 \quad (3.22)$$

$$1 \geq \beta_1 \geq \beta_2 \geq \dots \geq \beta_p \geq 0 \quad (3.23)$$

$$\alpha_k^2 + \beta_k^2 = 1, \quad k = 1, \dots, p. \quad (3.24)$$

Columns of the matrices \mathbf{U} and \mathbf{V} are the left generalized singular vectors, and the right generalized singular vectors are the columns of \mathbf{Y} , that is

$$\mathbf{Y} = \begin{pmatrix} \mathbf{y}_1 & \mathbf{y}_2 & \dots & \mathbf{y}_\ell \end{pmatrix}. \quad (3.25)$$

The generalized singular values of matrix pair (\mathbf{X}, \mathbf{L}) are defined as:

$$\gamma_k = \frac{\alpha_k}{\beta_k} \quad \text{for } k = 1, \dots, p. \quad (3.26)$$

It is easy to derive that GSVD is a generalization of SVD when matrix \mathbf{L} is equal to the identity matrix \mathbf{I} . For $\mathbf{L} = \mathbf{I}$ and $p = \ell$ we have

$$\mathbf{I} = \mathbf{V} \mathbf{D}_{\mathbf{L}} \mathbf{Y}^{-1} \Rightarrow \mathbf{D}_{\mathbf{L}}^{-1} \mathbf{V}^* = \mathbf{Y}^{-1} \Rightarrow \mathbf{X} = \mathbf{U} \mathbf{D}_{\mathbf{X}} \mathbf{D}_{\mathbf{L}}^{-1} \mathbf{V}^*.$$

Then, the SVD of matrix \mathbf{X} is given as:

$$\mathbf{X} = \mathbf{U} \text{diag} \left(\frac{\alpha_1}{\beta_1}, \dots, \frac{\alpha_p}{\beta_p} \right) \mathbf{V}^*,$$

and generalized singular values of (\mathbf{X}, \mathbf{I}) are equal to singular values of matrix \mathbf{X} with the opposite ordering.

The connection between normal and general singular values only exist when $\mathbf{L} = \mathbf{I}$ as described above. However, some relations regarding well and ill conditioned matrices can be derived for a general case.

It can be shown that, for a well conditioned matrix \mathbf{L} , the matrix \mathbf{Y} is well conditioned [34]. As a consequence, the ill-conditioning of the matrix \mathbf{X} is displayed on the diagonal matrix $\mathbf{D}_{\mathbf{X}}$. Since the relation

$$\gamma_k = \frac{\alpha_k}{\beta_k} = \frac{\alpha_k}{\sqrt{1 - \alpha_k^2}} \approx \alpha_k \quad (3.27)$$

holds for a small α_k , the generalized singular values defined with 3.26 must decay to zero as ordinary singular values do.

Chapter 4

Direct Regularization Methods

According to Hadamard conditions: a problem is well posed if it has a unique solution which depends continuously on the data. This means that small noise in the input measured data does not produce large errors in the solution. However, if one of this conditions is not satisfied, a problem is called ill posed. When using Moore-Penrose pseudoinverse to find a least squares solution of an ill posed problem, the smaller singular values together with the noise from the measured data, can have a detrimental effect on the solution. That is why the idea of direct regularization methods is to decrease the influence of the smallest singular values and corresponding singular vectors. In this chapter we describe a well known direct regularization methods: truncated SVD and GSVD, Tikhonov regularization in standard and general form and damped SVD and GSVD which are in next chapters used for regularization in ultrasound tomography.

Direct regularization methods that utilize SVD can be written in the form $\mathbf{y}_\lambda = \mathbf{X}_\lambda^\dagger \mathbf{b}$ where matrix $\mathbf{X}_\lambda^\dagger$ is the regularized inverse of matrix \mathbf{X} defined as:

$$\mathbf{X}_\lambda^\dagger = \mathbf{V} \begin{pmatrix} \boldsymbol{\Sigma}_\lambda^{-1} & \mathbf{0} \end{pmatrix} \mathbf{U}^* = \sum_{i=1}^{\ell} f_i(\lambda) \frac{1}{\sigma_i} \mathbf{v}_i \mathbf{u}_i^*. \quad (4.1)$$

The matrix $\boldsymbol{\Sigma}_\lambda^{-1}$ is diagonal matrix $\text{diag} \left(\frac{f_1(\lambda)}{\sigma_1}, \dots, \frac{f_\ell(\lambda)}{\sigma_\ell} \right)$. Filter factors, denoted with $f_i(\lambda)$, are responsible for minimizing the influence of smaller singular values on the calculated solution. They depend on the regularization parameter λ and define different methods.

In general, the regularized inverse $\mathbf{X}_\lambda^\dagger$ satisfies third and fourth Penrose condition:

$$1. (\mathbf{X}\mathbf{X}_\lambda^\dagger)^* = \mathbf{X}\mathbf{X}_\lambda^\dagger$$

$$\begin{aligned} (\mathbf{X}\mathbf{X}_\lambda^\dagger)^* &= (\mathbf{V} \begin{pmatrix} \boldsymbol{\Sigma}_\lambda^{-1} & \mathbf{0} \end{pmatrix} \mathbf{U}^*)^* \left(\mathbf{U} \begin{pmatrix} \boldsymbol{\Sigma} \\ \mathbf{0} \end{pmatrix} \mathbf{V}^* \right)^* = \mathbf{U} \begin{pmatrix} \boldsymbol{\Sigma}_\lambda^{-1} \\ \mathbf{0} \end{pmatrix} \begin{pmatrix} \boldsymbol{\Sigma} & \mathbf{0} \end{pmatrix} \mathbf{U}^* \\ &= \mathbf{U} \begin{pmatrix} \boldsymbol{\Sigma}_\lambda^{-1} \boldsymbol{\Sigma} & \mathbf{0} \\ \mathbf{0} & \mathbf{0} \end{pmatrix} \mathbf{U}^* = \mathbf{U} \begin{pmatrix} \boldsymbol{\Sigma} \boldsymbol{\Sigma}_\lambda^{-1} & \mathbf{0} \\ \mathbf{0} & \mathbf{0} \end{pmatrix} \mathbf{U}^* = \mathbf{U} \begin{pmatrix} \boldsymbol{\Sigma} \\ \mathbf{0} \end{pmatrix} \mathbf{V}^* \mathbf{V} \begin{pmatrix} \boldsymbol{\Sigma}_\lambda^{-1} & \mathbf{0} \end{pmatrix} \mathbf{U}^* \\ &= \mathbf{X}\mathbf{X}_\lambda^\dagger \end{aligned}$$

$$2. (\mathbf{X}_\lambda^\dagger \mathbf{X})^* = \mathbf{X}_\lambda^\dagger \mathbf{X}.$$

$$\begin{aligned} (\mathbf{X}_\lambda^\dagger \mathbf{X})^* &= (\mathbf{V}^*)^* \begin{pmatrix} \boldsymbol{\Sigma} & \mathbf{0} \end{pmatrix} \mathbf{U}^* \mathbf{U} \begin{pmatrix} \boldsymbol{\Sigma}_\lambda^{-1} \\ \mathbf{0} \end{pmatrix} \mathbf{V}^* = \mathbf{V} \begin{pmatrix} \boldsymbol{\Sigma} \boldsymbol{\Sigma}_\lambda^{-1} & \mathbf{0} \\ \mathbf{0} & \mathbf{0} \end{pmatrix} \mathbf{V}^* \\ &= \mathbf{V} \begin{pmatrix} \boldsymbol{\Sigma}_\lambda^{-1} & \mathbf{0} \end{pmatrix} \mathbf{U}^* \mathbf{U} \begin{pmatrix} \boldsymbol{\Sigma} \\ \mathbf{0} \end{pmatrix} \mathbf{V}^* = \mathbf{X}_\lambda^\dagger \mathbf{X}. \end{aligned}$$

The first and second Penrose conditions are discussed for each method separately in the following sections.

4.1 Truncated SVD and GSVD

Truncated singular value decomposition (TSVD) as a method of regularization for an ill-posed linear system (3.7) was discussed by Hansen in [30]. The idea of TSVD is to derive a new linear system by replacing matrix \mathbf{X} with the well-conditioned matrix \mathbf{X}_k defined in equation (3.5). The matrix \mathbf{X}_k is the best k-rank approximation for matrix \mathbf{X} as stated in Theorem 3.1.2. Then, a solution of new linear system is the TSVD solution \mathbf{y}_k of given ill-posed system (3.7) and it is defined as:

$$\mathbf{y}_k = \sum_{i=1}^k \frac{\mathbf{u}_i^T \mathbf{b}}{\sigma_i} \mathbf{v}_i. \quad (4.2)$$

The singular values are denoted with σ_i , and \mathbf{u}_i and \mathbf{v}_i , are left and right singular vectors as defined in Theorem 3.1.1.

The regularized inverse from equation (4.1) in the case of TSVD is defined as:

$$\mathbf{X}_k^\dagger = \mathbf{V} \begin{pmatrix} \boldsymbol{\Sigma}_k^{-1} & \mathbf{0} \end{pmatrix} \mathbf{U}^* = \sum_{i=1}^k \frac{1}{\sigma_i} \mathbf{v}_i \mathbf{u}_i^*, \quad (4.3)$$

where matrix $\Sigma_k^{-1} \in \mathbb{R}^{\ell \times \ell}$ is given as:

$$\Sigma_k^{-1} = \begin{pmatrix} \text{diag}\left(\frac{1}{\sigma_1}, \dots, \frac{1}{\sigma_k}\right) & \mathbf{0} \\ \mathbf{0} & \mathbf{0} \end{pmatrix}$$

The filter factors for the TSVD method are defined as:

$$f_i(k) = \begin{cases} 1 & \text{for } \sigma_i \geq \sigma_k \\ 0 & \text{for } \sigma_i < \sigma_k \end{cases}. \quad (4.4)$$

With this approach, the biggest k singular values are kept and the rest of smaller singular values and corresponding singular vectors are truncated. This results in decreasing the effect of the noise from the right side vector \mathbf{b} on the solution of linear system in equation (3.7).

We note that, for the TSVD method, the real regularization parameter λ is replaced with integer parameter k .

As already stated, in general, the regularized inverse satisfies third and fourth Penrose condition. However, in TSVD case, \mathbf{X}_k^\dagger also satisfies the second Penrose condition:

$$\begin{aligned} \mathbf{X}_k^\dagger \mathbf{X} \mathbf{X}_k^\dagger &= \mathbf{V} \begin{pmatrix} \Sigma_k^{-1} & \mathbf{0} \end{pmatrix} \mathbf{U}^* \mathbf{U} \begin{pmatrix} \Sigma \\ \mathbf{0} \end{pmatrix} \mathbf{V}^* \mathbf{V} \begin{pmatrix} \Sigma_k^{-1} & \mathbf{0} \end{pmatrix} \mathbf{U}^* \\ &= \mathbf{V} \begin{pmatrix} \Sigma_k^{-1} & \mathbf{0} \end{pmatrix} \begin{pmatrix} \Sigma \\ \mathbf{0} \end{pmatrix} \begin{pmatrix} \Sigma_k^{-1} & \mathbf{0} \end{pmatrix} \mathbf{U}^* = \mathbf{V} \Sigma_k^{-1} \Sigma \begin{pmatrix} \Sigma_k^{-1} & \mathbf{0} \end{pmatrix} \mathbf{U}^* \\ &= \mathbf{V} \begin{pmatrix} \mathbf{I}_k & \\ & \mathbf{0}_{\ell-k} \end{pmatrix} \begin{pmatrix} \Sigma_k^{-1} & \mathbf{0} \end{pmatrix} \mathbf{U}^* = \mathbf{V} \begin{pmatrix} \Sigma_k^{-1} & \mathbf{0} \end{pmatrix} \mathbf{U}^* = \mathbf{X}_k^\dagger \end{aligned}$$

The first condition is not satisfied because:

$$\begin{aligned} \mathbf{X} \mathbf{X}_k^\dagger \mathbf{X} &= \mathbf{U} \begin{pmatrix} \Sigma \\ \mathbf{0} \end{pmatrix} \mathbf{V}^* \mathbf{V} \begin{pmatrix} \Sigma_k^{-1} & \mathbf{0} \end{pmatrix} \mathbf{U}^* \mathbf{U} \begin{pmatrix} \Sigma \\ \mathbf{0} \end{pmatrix} \mathbf{V}^* \\ &= \mathbf{U} \begin{pmatrix} \Sigma \\ \mathbf{0} \end{pmatrix} \begin{pmatrix} \Sigma_k^{-1} & \mathbf{0} \end{pmatrix} \begin{pmatrix} \Sigma \\ \mathbf{0} \end{pmatrix} \mathbf{V}^* = \mathbf{U} \begin{pmatrix} \Sigma \Sigma_k^{-1} & \mathbf{0} \\ \mathbf{0} & \mathbf{0} \end{pmatrix} \begin{pmatrix} \Sigma \\ \mathbf{0} \end{pmatrix} \mathbf{V}^* \\ &= \mathbf{U} \begin{pmatrix} \Sigma \Sigma_k^{-1} \Sigma \\ \mathbf{0} \end{pmatrix} \mathbf{V}^* = \mathbf{X}_k \neq \mathbf{X} \end{aligned}$$

The following example presents the ill-posed linear system from example 3.2.2 solved using the TSVD method.

Example 4.1.1. We want to solve the linear system $\mathbf{X}\mathbf{y} = \tilde{\mathbf{b}}$ from the Example 3.2.2 using the TSVD method. Since the matrix \mathbf{X} has three singular values, the possible values for regularization parameter k are 1 and 2.

- For $k = 1$, only the biggest singular value $\sigma_1 = 0.2$ is used to calculate the solution.

Then, the TSVD solution is $\mathbf{y}_k = \begin{pmatrix} 0.089621849834053 \\ -0.002218345717926 \\ 0.106600877329206 \end{pmatrix}$ with relative error equal to 0.7392.

- For $k = 2$, first two singular values $\sigma_1 = 0.2$ and $\sigma_2 = 10^{-6}$ are used. Then, the

TSVD solution is $\mathbf{y}_k = \begin{pmatrix} 0.381207870431206 \\ -0.201913739862813 \\ -0.142697933712352 \end{pmatrix}$ with relative error equal to 1.0535.

Although the relative errors for TSVD solutions are high for this example, they are an improvement compared to the solution obtained with equation 3.11 in Example 3.2.2.

The problem for TSVD is how to choose the regularization parameter k , that is how to decide which singular values to keep and which to truncate. More on this topic is written in Chapter 5.

4.1.1 TGSVD

Truncated generalized singular value decomposition (TGSVD) method, [31], [34], is based on the same idea of truncating smaller values as aforementioned TSVD. However, the difference is that TGSVD employs a regularization matrix \mathbf{L} , described in Subsection 3.2.1. In addition, TGSVD solves the problem (3.14) instead of linear system (3.7). The GSVD of matrix pair (\mathbf{X}, \mathbf{L}) is used to calculate the solution and smallest generalized singular values and the corresponding generalized singular vectors are truncated.

The formula for TGSVD solution of problem (3.14) is derived as follows. First, in equation $\begin{pmatrix} \mathbf{X} \\ \mathbf{L} \end{pmatrix} \mathbf{y} = \begin{pmatrix} \mathbf{b} \\ \mathbf{0} \end{pmatrix}$, matrices \mathbf{X} and \mathbf{L} are replaced with the GSVD of matrix pair (\mathbf{X}, \mathbf{L}) defined in 3.20 and 3.21. Then we have

$$\begin{pmatrix} \mathbf{U} \begin{pmatrix} \mathbf{D}_{\mathbf{X}} & \mathbf{0} \\ \mathbf{0} & \mathbf{I}_{\ell-p} \end{pmatrix} \mathbf{Y}^{-1} \\ \mathbf{V} \begin{pmatrix} \mathbf{D}_{\mathbf{L}} & \mathbf{0} \end{pmatrix} \mathbf{Y}^{-1} \end{pmatrix} \mathbf{y} = \begin{pmatrix} \mathbf{b} \\ \mathbf{0} \end{pmatrix} \Rightarrow \mathbf{y} = \mathbf{Y} \begin{pmatrix} \mathbf{D}_{\mathbf{X}}^{-1} & \mathbf{0} \\ \mathbf{0} & \mathbf{I}_{\ell-p} \end{pmatrix} \mathbf{U}^* \mathbf{b}. \quad (4.5)$$

It is obvious that only matrices \mathbf{U} , $\mathbf{D}_{\mathbf{X}}$ and \mathbf{Y} have effect on the solution \mathbf{y} . The idea of TGSVD is to truncate smallest generalized values. We will use diagonal matrix $\mathbf{D}_{X_k}^{-1}$ defined as:

$$\mathbf{D}_{X_k}^{-1} = \begin{pmatrix} \mathbf{0} & \mathbf{0} \\ \mathbf{0} & \text{diag}(\alpha_{p-k+1}^{-1}, \dots, \alpha_p^{-1}) \end{pmatrix} \in \mathbb{R}^{p \times p} \quad (4.6)$$

to truncate lowest k values of α_i from the solution. Now, the TGSVD solution is defined as:

$$\mathbf{y}_k = \mathbf{X}_k^\dagger \mathbf{b}, \quad \mathbf{X}_k^\dagger = \mathbf{Y} \begin{pmatrix} \mathbf{D}_{X_k}^{-1} & \mathbf{0} \\ \mathbf{0} & \mathbf{I}_{\ell-p} \end{pmatrix} \mathbf{U}^*. \quad (4.7)$$

The matrix \mathbf{X}_k^\dagger can be interpreted as regularized inverse of matrix \mathbf{X} in the TGSVD case. It satisfies two Penrose conditions: $(\mathbf{X}\mathbf{X}_k^\dagger)^* = \mathbf{X}\mathbf{X}_k^\dagger$ and $\mathbf{X}_k^\dagger\mathbf{X}\mathbf{X}_k^\dagger = \mathbf{X}_k^\dagger$. These relations are easy to prove, similarly as it is in the TSVD case. However, the other two conditions are not satisfied:

1. $(\mathbf{X}_k^\dagger\mathbf{X})^* \neq \mathbf{X}_k^\dagger\mathbf{X}$

$$\begin{aligned} (\mathbf{X}_k^\dagger\mathbf{X})^* &= (\mathbf{Y}^{-1})^* \begin{pmatrix} \mathbf{D}_{\mathbf{X}} & \mathbf{0} \\ \mathbf{0} & \mathbf{I}_{\ell-p} \end{pmatrix} \begin{pmatrix} \mathbf{D}_{X_k}^{-1} & \mathbf{0} \\ \mathbf{0} & \mathbf{I}_{\ell-p} \end{pmatrix} \mathbf{Y}^* = \\ &(\mathbf{Y}^{-1})^* \begin{pmatrix} \mathbf{D}_{X_k}^{-1} & \mathbf{0} \\ \mathbf{0} & \mathbf{I}_{\ell-p} \end{pmatrix} \mathbf{U}^* \mathbf{U} \begin{pmatrix} \mathbf{D}_{\mathbf{X}} & \mathbf{0} \\ \mathbf{0} & \mathbf{I}_{\ell-p} \end{pmatrix} \mathbf{Y}^* \neq \mathbf{X}_k^\dagger\mathbf{X}, \end{aligned}$$

because \mathbf{Y} is not necessary an unitary matrix.

2. $\mathbf{X}\mathbf{X}_k^\dagger\mathbf{X} \neq \mathbf{X}$

$$\begin{aligned} \mathbf{X}\mathbf{X}_k^\dagger\mathbf{X} &= \mathbf{U} \begin{pmatrix} \mathbf{D}_{\mathbf{X}} & \mathbf{0} \\ \mathbf{0} & \mathbf{I}_{\ell-p} \end{pmatrix} \mathbf{Y}^{-1} \mathbf{Y} \begin{pmatrix} \mathbf{D}_{X_k}^{-1} & \mathbf{0} \\ \mathbf{0} & \mathbf{I}_{\ell-p} \end{pmatrix} \mathbf{U}^* \mathbf{U} \begin{pmatrix} \mathbf{D}_{\mathbf{X}} & \mathbf{0} \\ \mathbf{0} & \mathbf{I}_{\ell-p} \end{pmatrix} \mathbf{Y}^{-1} \\ &= \mathbf{U} \begin{pmatrix} \mathbf{D}_{\mathbf{X}} \mathbf{D}_{X_k}^{-1} \mathbf{D}_{\mathbf{X}} & \mathbf{0} \\ \mathbf{0} & \mathbf{I}_{\ell-p} \end{pmatrix} \mathbf{Y}^{-1} \neq \mathbf{U} \begin{pmatrix} \mathbf{D}_{\mathbf{X}} & \mathbf{0} \\ \mathbf{0} & \mathbf{I}_{\ell-p} \end{pmatrix} \mathbf{Y}^{-1} = \mathbf{X} \end{aligned}$$

The TGSVD solution from equation 4.7 can be expressed using filter factors similar to 4.2. The derivation of this expression follows from equations 4.7 and 4.6, by partitioning matrices \mathbf{Y} and \mathbf{U} to the first p and last $\ell - p$ columns as:

$$\begin{aligned} \mathbf{y}_k &= \mathbf{X}_k^\dagger \mathbf{b} = \begin{pmatrix} \mathbf{Y}_p & \mathbf{Y}_{\ell-p} \end{pmatrix} \cdot \begin{pmatrix} \mathbf{D}_{X_k}^{-1} & \mathbf{0} \\ \mathbf{0} & \mathbf{I}_{\ell-p} \end{pmatrix} \cdot \begin{pmatrix} \mathbf{U}_p^* \\ \mathbf{U}_{\ell-p}^* \end{pmatrix} \mathbf{b} \\ &= \mathbf{Y}_p \mathbf{D}_{X_k}^{-1} \mathbf{U}_p^* \mathbf{b} + \mathbf{Y}_{\ell-p} \mathbf{U}_{\ell-p}^* \mathbf{b} \end{aligned}$$

This yields an expression for the TGSVD solution as:

$$\mathbf{y}_k = \sum_{i=p-k+1}^p \frac{\mathbf{u}_i^* \mathbf{b}}{\alpha_i} \mathbf{y}_i + \sum_{i=p+1}^{\ell} (\mathbf{u}_i^* \mathbf{b}) \mathbf{y}_i. \quad (4.8)$$

The equation 4.8 can be written in the terms of sharp filter factors:

$$f_i(k) = \begin{cases} 1 & \text{for } \alpha_i \geq \alpha_k \\ 0 & \text{for } \alpha_i < \alpha_k \end{cases}. \quad (4.9)$$

Another way to defined a TGSVD solution is to use transformations form standard to general form [34].

In order to show the effects of regularization matrix \mathbf{L} within TGSVD, we solve the ill-posed linear system from Example 3.2.2.

Example 4.1.2. We want to solve the linear system $\mathbf{X}\mathbf{y} = \tilde{\mathbf{b}}$ given in Example 3.2.2 using the TGSVD method. Since this method requires regularization matrix \mathbf{L} , we use the matrix \mathbf{L}_1 defined in equation 3.15 for this purpose.

The matrix pair (\mathbf{X}, \mathbf{L}) has two generalized singular values

$$\gamma_1 = \frac{0.000000155573386}{0.99999999999988} \quad \text{and} \quad \gamma_2 = \frac{0.000001845960242}{0.999999999998296},$$

so we set regularization parameter k equal to 1. We would like to note that matrices \mathbf{U} i \mathbf{V} obtained with GSVD are different from those obtained with SVD, and they are

$$\mathbf{U} = \begin{pmatrix} -0.180834540312718 & -0.236776638230098 & -0.636634543773113 \\ 0.319158969349612 & 0.602405347441124 & -0.662199870668450 \\ -0.738067575123392 & -0.237292725674562 & -0.314250007747914 \\ 0.566297338740929 & -0.724387177761126 & -0.239655422621572 \end{pmatrix}$$

and

$$\mathbf{V} = \begin{pmatrix} 0.410172291592458 & -0.912008054355767 \\ -0.912008054355767 & -0.410172291592458 \end{pmatrix}.$$

Matrix \mathbf{Y} is given as:

$$\mathbf{Y} = \begin{pmatrix} -0.560874307343569 & -1.432157713852067 & -3.589778559998338 \\ -1.381218890528475 & 0.391858394856359 & -3.589778559998338 \\ 0.442797218183038 & 1.212202978039876 & -3.589778559998335 \end{pmatrix}.$$

Then, the TGSVD solution is $\mathbf{y}_k = \begin{pmatrix} 0.099999999985196 \\ 0.10000000004051 \\ 0.100000000012531 \end{pmatrix}$ with relative error equal to $1.1440 \cdot 10^{-10}$.

This relative error is much lower than errors of solutions obtained with the TSVD method and equation 3.11 in Example 3.2.2.

We would like to note that for this particular example, the usage of matrix \mathbf{L} has bigger effect on the improvement of the solution than the truncation. The reason for this is exact solution has constant values equal to 0.1, so first order derivative operator smooths the noise. When we set $k = 2$, there is no truncation. However, the solution is

$$\mathbf{y}_k = \begin{pmatrix} 0.100000000010212 \\ 0.100000000065656 \\ 0.099999999992781 \end{pmatrix} \text{ with relative error equal to } 3.8588 \cdot 10^{-10}.$$

The TGSVD method has the same problem as TSVD, that is how to decide which values to keep and which to truncate. More on this is given in Chapter 5.

4.2 Tikhonov Regularization

Tikhonov regularization is one of the best known direct regularization methods and is often used to solve discrete ill-posed problem $\mathbf{X}\mathbf{y} = \mathbf{b}$. Its formulation as an optimization problem is given as:

$$\min_{\mathbf{y} \in \mathbb{C}^n} \{ \|\mathbf{b} - \mathbf{X}\mathbf{y}\|_2^2 + \lambda^2 \|\mathbf{L}\mathbf{y}\|_2^2 \}, \quad (4.10)$$

while its two alternative forms are:

$$\min \left\| \begin{pmatrix} \mathbf{X} \\ \lambda \mathbf{L} \end{pmatrix} \mathbf{y} - \begin{pmatrix} \mathbf{b} \\ \mathbf{0} \end{pmatrix} \right\|_2 \quad \text{and} \quad (\mathbf{X}^* \mathbf{X} + \lambda^2 \mathbf{L}^* \mathbf{L}) \mathbf{y} = \mathbf{X}^* \mathbf{b}. \quad (4.11)$$

The method minimizes the residual $\mathbf{r} = \mathbf{b} - \mathbf{X}\mathbf{y}$ and controls the norm of vector $\mathbf{L}\mathbf{y}$ using positive regularization parameter λ . When matrix \mathbf{L} is equal to identity matrix \mathbf{I} then the method is in standard form. Otherwise, it is in general form. Common choices for regularization matrix \mathbf{L} are described in Subsection 3.2.1.

The Tikhonov solution is defined as:

$$\mathbf{y}_\lambda = \mathbf{X}_\lambda^\dagger \mathbf{b}, \quad \mathbf{X}_\lambda^\dagger = (\mathbf{X}^* \mathbf{X} + \lambda^2 \mathbf{L}^* \mathbf{L})^{-1} \mathbf{X}^*. \quad (4.12)$$

For this solution to be unique, condition $\mathcal{N}(\mathbf{X}) \cap \mathcal{N}(\mathbf{L}) = \{0\}$ must be satisfied. The same condition is also required for the existence of GSVD of matrix pair (\mathbf{X}, \mathbf{L}) as seen in Section 3.3.

4.2.1 Regularized inverse and filter factors

The matrix $\mathbf{X}_\lambda^\dagger$ is the regularized inverse of matrix \mathbf{X} in Tikhonov case. We can derive its alternative form, similar to those of TSVD (equation 4.3) and TGSVD (equation 4.7) which contains filter factors.

For Tikhonov regularization in standard form, we use the SVD of matrix \mathbf{X} to calculate the product $\mathbf{X}^* \mathbf{X} = \mathbf{V} \mathbf{\Sigma}^2 \mathbf{V}^*$ and set $\mathbf{L}^* \mathbf{L} = \mathbf{I}$. Then, it follows:

$$\begin{aligned} \mathbf{X}_\lambda^\dagger &= (\mathbf{V} \mathbf{\Sigma}^2 \mathbf{V}^* + \lambda^2 \mathbf{I})^{-1} \mathbf{V} \begin{pmatrix} \mathbf{\Sigma}^* & \mathbf{0} \end{pmatrix} \mathbf{U}^* = (\mathbf{V} \mathbf{\Sigma}^2 \mathbf{V}^* + \lambda^2 \mathbf{V} \mathbf{V}^*)^{-1} \mathbf{V} \begin{pmatrix} \mathbf{\Sigma} & \mathbf{0} \end{pmatrix} \mathbf{U}^* \\ &= (\mathbf{V} (\mathbf{\Sigma}^2 + \lambda^2 \mathbf{I}) \mathbf{V}^*)^{-1} \mathbf{V} \begin{pmatrix} \mathbf{\Sigma} & \mathbf{0} \end{pmatrix} \mathbf{U}^* = (\mathbf{V}^*)^{-1} (\mathbf{\Sigma}^2 + \lambda^2 \mathbf{I})^{-1} \begin{pmatrix} \mathbf{\Sigma} & \mathbf{0} \end{pmatrix} \mathbf{U}^* \\ &= \mathbf{V} \text{diag}((\sigma_1^2 + \lambda^2)^{-1}, \dots, (\sigma_\ell^2 + \lambda^2)^{-1}) \begin{pmatrix} \text{diag}(\sigma_1, \dots, \sigma_\ell) & \mathbf{0} \end{pmatrix} \mathbf{U}^* \\ &= \mathbf{V} \begin{pmatrix} \text{diag} \left(\frac{\sigma_1}{\sigma_1^2 + \lambda^2}, \dots, \frac{\sigma_\ell}{\sigma_\ell^2 + \lambda^2} \right) & \mathbf{0} \end{pmatrix} \mathbf{U}^* \end{aligned}$$

Comparing this derived form of $\mathbf{X}_\lambda^\dagger$ to the equation (4.1), we conclude $\frac{f_i(\lambda)}{\sigma_i} = \frac{\sigma_i}{\sigma_i^2 + \lambda^2}$. Then, the filter factors for Tikhonov regularization in standard form are:

$$f_i(\lambda) = \frac{\sigma_i^2}{\sigma_i^2 + \lambda^2} \quad \text{for all } i = 1, \dots, p. \quad (4.13)$$

The regularized solution \mathbf{y}_λ can be defined with filter factors as:

$$\mathbf{y}_\lambda = \mathbf{X}_\lambda^\dagger \mathbf{b} = \sum_{i=1}^{\ell} f_i(\lambda) \frac{\mathbf{u}_i^* \mathbf{b}}{\sigma_i} \mathbf{v}_i. \quad (4.14)$$

Using filter factors (4.13) contribution of smaller singular values $\sigma_i < \lambda$ and their corresponding singular vectors is neglected in \mathbf{y}_λ .

Regarding the Penrose conditions for $\mathbf{X}_\lambda^\dagger$, we already proved at the beginning of this chapter that two conditions holds: $(\mathbf{X}\mathbf{X}_\lambda^\dagger)^* = \mathbf{X}\mathbf{X}_\lambda^\dagger$ and $(\mathbf{X}_\lambda^\dagger\mathbf{X})^* = \mathbf{X}_\lambda^\dagger\mathbf{X}$. However, other two conditions are not satisfied.

Similar process of derivation is for Tikhonov regularization in general form. We replace matrices \mathbf{X} and \mathbf{L} with GSVD of matrix pair (\mathbf{X}, \mathbf{L}) and calculate products:

$$\begin{aligned} \mathbf{X}^* \mathbf{X} &= (\mathbf{Y}^{-1})^* \begin{pmatrix} \mathbf{D}_\mathbf{X} & \mathbf{0} \\ \mathbf{0} & \mathbf{I}_{\ell-p} \end{pmatrix} \mathbf{U}^* \mathbf{U} \begin{pmatrix} \mathbf{D}_\mathbf{X} & \mathbf{0} \\ \mathbf{0} & \mathbf{I}_{\ell-p} \end{pmatrix} \mathbf{Y}^{-1} \\ &= (\mathbf{Y}^{-1})^* \begin{pmatrix} \text{diag}(\alpha_1^2, \dots, \alpha_p^2) & \mathbf{0} \\ \mathbf{0} & \mathbf{I}_{\ell-p} \end{pmatrix} \mathbf{Y}^{-1}, \end{aligned}$$

$$\begin{aligned} \mathbf{L}^* \mathbf{L} &= (\mathbf{Y}^{-1})^* \begin{pmatrix} \mathbf{D}_\mathbf{L} \\ \mathbf{0} \end{pmatrix} \mathbf{V}^* \mathbf{V} \begin{pmatrix} \mathbf{D}_\mathbf{L} & \mathbf{0} \end{pmatrix} \mathbf{Y}^{-1} \\ &= (\mathbf{Y}^{-1})^* \begin{pmatrix} \text{diag}(\beta_1^2, \dots, \beta_p^2) & \mathbf{0} \\ \mathbf{0} & \mathbf{0} \end{pmatrix} \mathbf{Y}^{-1}. \end{aligned}$$

Then, the alternative form of regularized inverse $\mathbf{X}_\lambda^\dagger$ in Tikhonov case can be derived as:

$$\begin{aligned} \mathbf{X}_\lambda^\dagger &= (\mathbf{X}^* \mathbf{X} + \lambda^2 \mathbf{L}^* \mathbf{L})^{-1} \mathbf{X}^* \\ &= \left[(\mathbf{Y}^{-1})^* \left(\begin{pmatrix} \text{diag}(\alpha_1^2, \dots, \alpha_p^2) & \mathbf{0} \\ \mathbf{0} & \mathbf{I}_{\ell-p} \end{pmatrix} + \lambda^2 \begin{pmatrix} \text{diag}(\beta_1^2, \dots, \beta_p^2) & \mathbf{0} \\ \mathbf{0} & \mathbf{0} \end{pmatrix} \right) \mathbf{Y}^{-1} \right]^{-1} \mathbf{X}^* = \\ &\mathbf{Y} \begin{pmatrix} \text{diag}\left(\frac{1}{\alpha_1^2 + \lambda^2 \beta_1^2}, \dots, \frac{1}{\alpha_p^2 + \lambda^2 \beta_p^2}\right) & \mathbf{0} \\ \mathbf{0} & \mathbf{I}_{\ell-p} \end{pmatrix} ((\mathbf{Y}^{-1})^*)^{-1} (\mathbf{Y}^{-1})^* \begin{pmatrix} \text{diag}(\alpha_1, \dots, \alpha_p) & \mathbf{0} \\ \mathbf{0} & \mathbf{I}_{\ell-p} \end{pmatrix} \mathbf{U}^* \end{aligned}$$

This results in an alternative form of regularized inverse defined as:

$$\mathbf{X}_\lambda^\dagger = \mathbf{Y} \begin{pmatrix} \text{diag} \left(\frac{\alpha_1}{\alpha_1^2 + \lambda^2 \beta_1^2}, \dots, \frac{\alpha_p}{\alpha_p^2 + \lambda^2 \beta_p^2} \right) & \mathbf{0} \\ \mathbf{0} & \mathbf{I}_{\ell-p} \end{pmatrix} \mathbf{U}^* \quad (4.15)$$

From this new form, we can easily calculate the filter factors $f_i(\lambda)$ for the Tikhonov regularization in general form:

$$\frac{f_i(\lambda)}{\alpha_i} = \frac{\alpha_i}{\alpha_i^2 + \lambda^2 \beta_i^2} \Rightarrow f_i(\lambda) = \frac{\alpha_i^2}{\alpha_i^2 + \lambda^2 \beta_i^2} = \frac{\gamma_i^2}{\gamma_i^2 + \lambda^2} \quad \text{for all } i = 1, \dots, p. \quad (4.16)$$

The Tikhonov regularized solution in general form can be defined using filter factors as:

$$\mathbf{y}_\lambda = \sum_{i=1}^p f_i(\lambda) \frac{\mathbf{u}_i^* \mathbf{b}}{\alpha_i} \mathbf{y}_i + \sum_{i=p+1}^{\ell} (\mathbf{u}_i^* \mathbf{b}) \mathbf{y}_i \quad (4.17)$$

where \mathbf{y}_i are right singular vectors from Equation (3.25).

Regularized inverse $\mathbf{X}_\lambda^\dagger$ for Tikhonov regularization in general form only satisfies one condition: $(\mathbf{X}\mathbf{X}_\lambda^\dagger)^* = \mathbf{X}\mathbf{X}_\lambda^\dagger$. Other conditions fail to be satisfied as it is in the case of TGSVD and Tikhonov in standard form.

In the following example, the ill-posed linear system from example 3.2.2 is solved using Tikhonov regularization in standard and general form.

Example 4.2.1. We solve the linear system $\mathbf{X}\mathbf{y} = \tilde{\mathbf{b}}$ from Example 3.2.2 using Tikhonov regularization in standard and general form.

The solution in standard form requires SVD of matrix \mathbf{X} which is given in Example 3.2.2. The value of regularization parameter λ needs to satisfied the relation $\sigma_3 = 10^{-7} \leq \lambda \leq 0.2 = \sigma_1$.

1. For $\lambda = 10^{-7}$ the solution in standard form is $\mathbf{y}_\lambda = \begin{pmatrix} 0.082784283895891 \\ 0.057126917586478 \\ 0.113581473632773 \end{pmatrix}$ with relative error equal to 0.3174.

2. For $\lambda = 10^{-6}$ the solution in standard form is $\mathbf{y}_\lambda = \begin{pmatrix} 0.077697270098418 \\ 0.007029824639970 \\ 0.116815733267405 \end{pmatrix}$ with relative error equal to 0.6911.

3. For $\lambda = 0.2$ the solution in standard form is $\mathbf{y}_\lambda = \begin{pmatrix} 0.044810218297817 \\ -0.001109155368095 \\ 0.053299598176296 \end{pmatrix}$ with relative error equal to 1.7848.

For the general form case, solution requires GSVD of matrix pair (\mathbf{X}, \mathbf{L}) given in Example 4.1.2.

For $\lambda = \frac{0.000001845960242}{0.999999999998296}$ the solution in general form is $\mathbf{y}_\lambda = \begin{pmatrix} 0.09999999992774 \\ 0.10000000002460 \\ 0.100000000006126 \end{pmatrix}$

with relative error equal to $5.6507 \cdot 10^{-11}$.

For $\lambda = \frac{0.000000155573386}{0.99999999999998}$ the solution in general form is $\mathbf{y}_\lambda = \begin{pmatrix} 0.09999999997808 \\ 0.100000000034825 \\ 0.100000000002568 \end{pmatrix}$

with relative error equal to $2.0200 \cdot 10^{-10}$.

In this example Tikhonov regularization in general form produced solution with much lower relative error than standard form. This happened because the exact solution vector has constant values and regularization matrix \mathbf{L} smooths the noise. For this same example TGSVD obtained better solution than TSVD as seen before.

The main challenge with Tikhonov regularization in more complex examples is an adequate selection of parameter λ , since the choice is largely dependent on the problem being solved.

4.3 Damped SVD and GSVD

Idea of decreasing the influence of smallest singular values was also proposed by Ekstrom and Rhodes in [17]. They damped the smallest singular values using filter factors defined as:

$$f_i = \frac{\sigma_i}{\sigma_i + \lambda}. \quad (4.18)$$

These are smooth factors, as opposed to TSVDs sharp filter factors and similar to those of Tikhonov regularization. The DSVD solution is defined with formula

$$\mathbf{y}_\lambda = \sum_{i=1}^{\ell} \frac{\sigma_i}{\sigma_i + \lambda} \cdot \frac{\mathbf{u}_i^* \mathbf{b}}{\sigma_i} \mathbf{v}_i. \quad (4.19)$$

Following the aforementioned idea of damping smaller singular values instead of truncating them, Hansen in [32] described The Damped Generalized SVD (DGSVD). The filter factors for DGSVD are:

$$f_i = \frac{\alpha_i}{\alpha_i + \lambda \beta_i}, \quad i = 1, 2, \dots, p. \quad (4.20)$$

and the DGSVD solution is defined as:

$$\mathbf{y}_\lambda = \sum_{i=1}^p \frac{\alpha_i}{\alpha_i + \lambda \beta_i} \cdot \frac{\mathbf{u}_i^* \mathbf{b}}{\alpha_i} \mathbf{y}_i + \sum_{i=p+1}^{\ell} (\mathbf{u}_i^* \mathbf{b}) \mathbf{y}_i. \quad (4.21)$$

In this way, a generalized singular values smaller than λ are damped much faster than the bigger ones. It is necessary to use regularization parameter $\lambda \in \mathbb{R}^+$ suited for given problem.

Since there is similarity between D(G)SVD and Tikhonov regularization regarding the filter factors, regularized inverse $\mathbf{X}_\lambda^\dagger$ is defined in similar way and the same Penrose conditions are satisfied.

Example 4.3.1. We solve the linear system $\mathbf{X}\mathbf{y} = \tilde{\mathbf{b}}$ from Example 3.2.2 using DSVD and DGSVD.

Since DSVD and Tikhonov regularization in standard form both utilize SVD of matrix \mathbf{X} and have similar filter factors, candidates for the regularization parameter λ are same.

1. For $\lambda = 10^{-7}$ the solution in standard form is $\mathbf{y}_\lambda = \begin{pmatrix} 0.084771996846320 \\ 0.055765584333117 \\ 0.111881936779997 \end{pmatrix}$ with

relative error equal to 0.3196.

2. For $\lambda = 10^{-6}$ the solution in standard form is $\mathbf{y}_\lambda = \begin{pmatrix} 0.080525408487807 \\ 0.013949012599734 \\ 0.114581128353726 \end{pmatrix}$ with

relative error equal to 0.6354.

3. For $\lambda = 0.2$ the solution in standard form is $\mathbf{y}_\lambda = \begin{pmatrix} 0.044810113068864 \\ -0.001109028637699 \\ 0.053299689281974 \end{pmatrix}$ with relative error equal to 1.7848.

The GSVD of matrix pair (\mathbf{X}, \mathbf{L}) is utilized both by DGSVD and Tikhonov regularization in general form. Because of that, they have same candidates for λ .

For $\lambda = \frac{0.000001845960242}{0.99999999998296}$ the solution in general form is $\mathbf{y}_\lambda = \begin{pmatrix} 0.099999999994542 \\ 0.100000000006814 \\ 0.100000000004730 \end{pmatrix}$

with relative error equal to $5.732656561564236 \cdot 10^{-11}$.

For $\lambda = \frac{0.000000155573386}{0.99999999999988}$ the solution in general form is $\mathbf{y}_\lambda = \begin{pmatrix} 0.099999999998854 \\ 0.100000000034539 \\ 0.100000000001682 \end{pmatrix}$

with relative error equal to $1.997540846063769 \cdot 10^{-10}$.

These results produced by DSVD and DGSVD are very similar to the results produced by Tikhonov regularization in standard and general form.

However, the DSVD and DGSVD have the same issue as aforementioned methods, how to choose properly the regularization parameter $\lambda \in \mathbb{R}^+$, so that $\|\mathbf{b} - \mathbf{X}\mathbf{y}\|_2$ remains small and the solution \mathbf{y} is not noise dominated.

4.4 Regularization in UT with TSVD and TGSVD

In this section we compare the TSVD and TGSVD methods for the regularization of inverse problem within iterations of DBI. The aim is to investigate whether the inclusion of regularization matrix \mathbf{L} , which is the part of TGSVD, improves the reconstruction of scattering function from the noisy data.

Our simulation of UT, general guidelines are described in Section 2.5, has $M = 128$ transducers positioned equidistantly from one another, surrounding the ROI. Only $M_t = 32$ of the 128 transducers, one at a time, transmitted a sound wave at a frequency of $f = 500$ kHz. All the transducers received the echoes from every transmission and the background medium is loss-free. The ROI is a square with dimensions $40 \text{ mm} \times 40 \text{ mm}$.

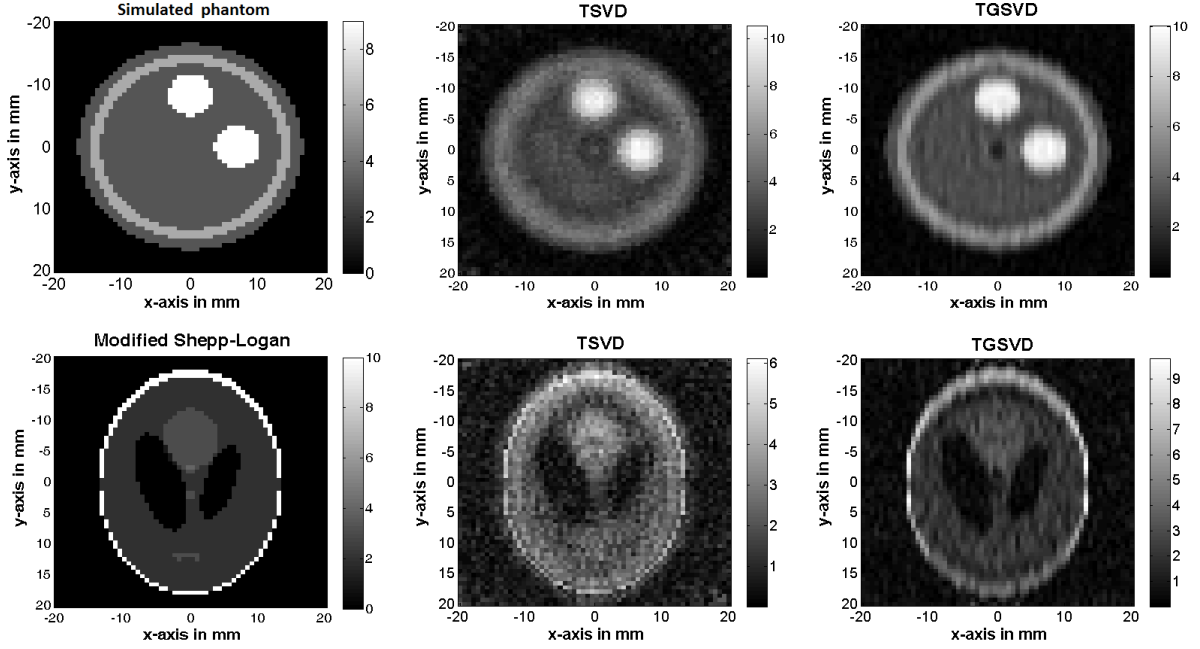


Figure 4.1: Exact phantom (left) and reconstruction after 10 iterations of DBI with TSVD (center) and TGSVD (right).

Table 4.1: RE- ℓ_2 of reconstructed scattering function

Method	Simulated phantom	Modified Shepp-Logan
TSVD	0.2693	0.6226
TGSVD	0.2014	0.5295

Two phantoms are used for the scattering object, simulated phantom and modified Shepp-Logan phantom, shown in left column of the Figure 4.1. The gray scale image of the true ROI is discretized with $N = 60 \times 60$ pixels. Other groups constructed the problem as an underdetermined system and found the approximate solution of the scattering function [27]. However, we constructed an overdetermined linear system within the inverse scattering section of the DBI algorithm. The number of unknowns is 60×60 which is less than the number of equations 128×32 . In order for our experiment to be more realistic, vector \mathbf{b} has a signal-to-noise ratio (SNR) of 30 dB.

We initialized the DBI method with Born approximation and then ran 10 iterations.

In each iteration, for the inverse scattering part, two different algorithms are utilized, TSVD and TGSVD.

In order to obtain quantitative measurement for quality of reconstruction with the DBI method, we calculate the relative ℓ_2 norm error (RE- ℓ_2) for the reconstructed scattering function "s" as:

$$\text{RE-}\ell_2 = \frac{\|\mathbf{s} - \widehat{\mathbf{s}}\|_2}{\|\mathbf{s}\|_2}. \quad (4.22)$$

The reconstructed images using TSVD and TGSVD are shown in Figure 4.1 and the results for RE- ℓ_2 are shown in Table 6.1. It is visible that for both phantoms, TGSVD provides lower error. The usage of regularization matrix \mathbf{L} in TGSVD smoothed the solution to give a better image quality. This is shown in Figure 4.2 where slice plots of tested phantoms are compared. These plots were obtained from the reconstructed ROI after 10 iterations of DBI. For the simulated phantom we took vertical and horizontal line of the reconstructed phantom with fixed x-axis $x = 3.3$ mm and y-axis at $y = -1.33$ mm, respectively. For the modified Shepp-Logan we took vertical line with fixed x-axis at $x = 13.33$ mm and horizontal line with fixed y-axis at $y = -2.66$ mm. The TGSVD provided smoother solution and more reliable reconstruction of the edges, while TSVD failed to detect larger changes in the speed of sound contrast.

However, a problem with the aforementioned truncation techniques is the determination of the truncated parameter in Equations (4.2) and (4.7). Here, we choose k to be position where the highest drop in singular values occurred. More on the options for choosing the regularization parameter is presented in Chapter 5.

4.4.1 Conclusions

The simulation reveals that TGSVD outperforms TSVD when it is used for regularization within the inverse problem where the right side (\mathbf{b}) contain errors. This outcome can be attributed to the smoothing property of the matrix \mathbf{L} which causes a reduction in the noise. TGSVD, unlike TSVD, calculates the generalized singular values of the matrix pair (\mathbf{X}, \mathbf{L}) so that both matrices are equally represented which results in solution with less error.

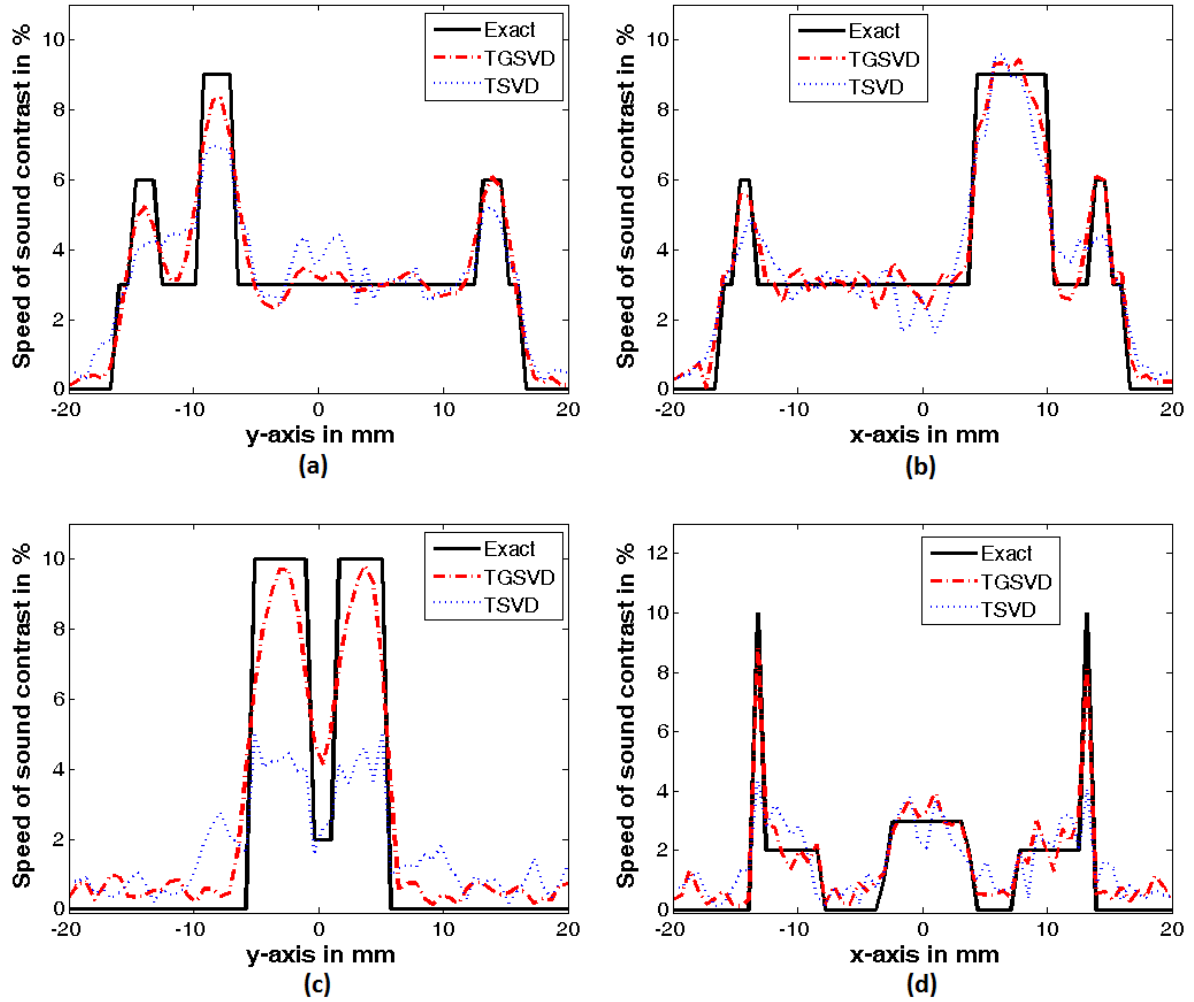


Figure 4.2: Slice plots of the scattering function after 10 iterations of DBI when TSVD and TGSVD are used for regularization. (a) Vertical slice at $x = 3.3$ mm, and (b) horizontal slice at $y = -1.33$ mm for the simulated phantom. (c) Vertical slice at $x = 13.33$ mm, and (d) horizontal slice at $y = -2.66$ mm for the modified Shepp-Logan phantom.

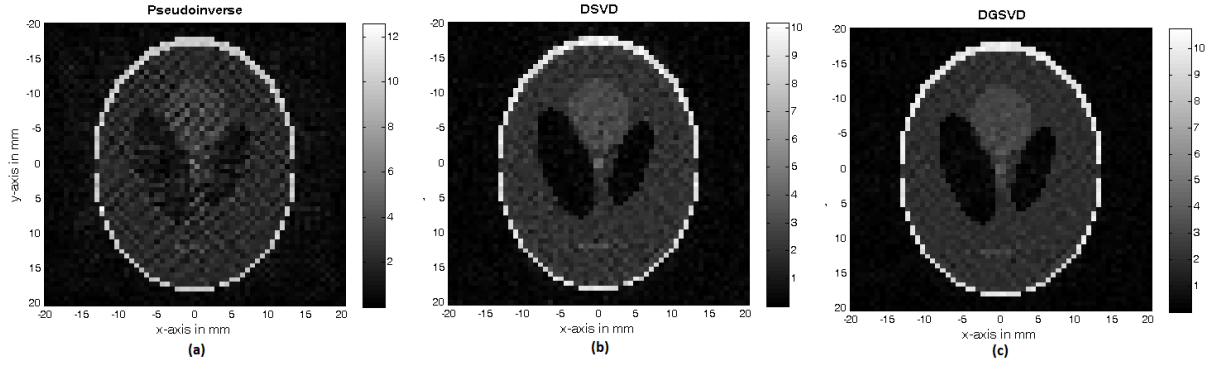


Figure 4.3: Reconstruction of the ROI after 6 iterations of DBI with (a) Pseudoinverse, (b) DSVD and (c) DGSVD, (SNR=30dB).

4.5 Regularization in UT with DSVD and DGSVD

For the purpose of testing the regularization properties of the methods DSVD and DGSVD, we reconstructed a grayscale image of the Modified Shepp-Logan phantom as our region of interest (ROI). Since the main focus is the reconstruction of velocity values, a grayscale image is an optimal way to present those values. We discretized ROI with $N = 60 \times 60$ pixels with $h = \frac{\lambda_0}{4.5}$. To construct a model problem for the DBI method, we assumed a circular array of 128 equidistant transducers surrounding the ROI. We transmit at a frequency of $f = 500$ kHz from each of the 32 transducers, one at a time, while all 128 transducers act as receivers. The radius of the circle is $r = 100$ mm and the background medium has a constant wavenumber $k_o = 2.122$. Thus, every time one transducer is transmitting, we collect the data from all of them. This leads to 32×128 equations and because the number of unknowns pixels is 3600, we constructed an overdetermined linear system. We tested the algorithms with added noise of $\text{SNR} = 30$ dB to the right hand side 'b'.

To numerically determined which of the methods is the best, we calculate relative ℓ_2 norm error of the scattering function as defined in the Equation (4.22). We choose the 1000th singular value as the parameter λ for DSVD and DGSVD. It is visible that DGSVD is much better in restoring the image than use of the pseudoinverse. When compared to DSVD, DGSVD produces pixel values that are closer to the original. Figure 4.3 are the reconstructed images of the ROI after 6 DBI iterations. Figure 4.4 shows

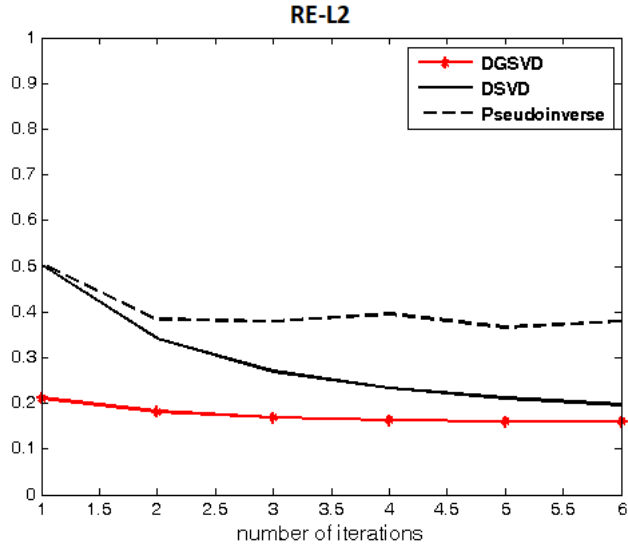


Figure 4.4: Plots of RE- ℓ_2 for scattering function during 6 iterations of DBI, $f=500\text{kHz}$.

the plots of relative error RE- ℓ_2 for 6 iterations of DBI in all three cases and confirms that DGSVD is better than DSVD or pseudoinverse. The results of the experiment show that gradual damping of the generalized singular values results in a better image quality and a more accurate approximation of the scattering function. Because, in our setting, the singular values are small and decay to zero gradually, we have an ill-posed problem and the pseudoinverse solution is noise dominated. In this way, damping decreases the influence of the small singular values on the solution. The DGSVD produces the best image and outperforms DSVD and pseudoinverse because, in addition to the damping, it reduces the value of $\|\mathbf{L}\mathbf{y}\|_2$ where \mathbf{L} is a first derivative operator, thereby smoothing the solution \mathbf{y}_λ in (4.21).

4.5.1 Conclusions

The smaller singular values of the matrix \mathbf{X} in system (3.7) cause the solution to be contaminated by noise and can lead to a poorly reconstructed image. In this section, we propose damping those values using the DGSVD method. In that way, not only is the noise contribution to the solution decreased, but also the regularization matrix \mathbf{L} insures a smooth solution \mathbf{y}_λ in (4.21). Our tests show that DGSVD regularization provides a higher quality solution than the DSVD regularization or the direct solution using the

Moore-Penrose pseudoinverse. Our choice for λ for these tests has been purely heuristic, thus a better approach for choosing λ is necessary.

Chapter 5

Choosing the Regularization Parameters

Direct regularization methods described in Chapter 4 are efficient in solving an inverse problem only if appropriate regularization parameter is chosen. For the TSVD and the TGSVD method, an integer value k will determine which of the smallest (generalized) singular values will be omitted. In the case of Tikhonov in standard and general form, DSVD and DGSVD, a positive real number λ is responsible for damping the influence of the smallest (generalized) singular values on the solution.

In this chapter we present well known algorithms for choosing the regularization parameter: generalized cross validation (GCV) and L-curve. Then, we derive our adaptive algorithm for determining λ based on the error resulted from the noise and signal loss.

We utilize Tikhonov regularization methods in standard and general form to solve the ill posed inverse part of the DBI method. Since the performance of these methods greatly depends on the choice of regularization parameter λ , in numerical results our adaptive algorithm is compared to GCV and L-curve.

5.1 Standard Methods for Choosing Regularization Parameter

5.1.1 Generalized Cross validation (GCV)

Generalized cross validation (GCV) was introduced in [22] and it was used to find parameter for the Tikhonov regularization in the standard form. The parameter λ is chosen to be the value that minimizes the GCV function defined as:

$$\text{GCV}(\lambda) = \frac{\|\mathbf{X}\mathbf{y}_\lambda - \mathbf{b}\|_2^2}{\left(\text{trace}(\mathbf{I} - \mathbf{X}\mathbf{X}_\lambda^\dagger)\right)^2} \quad (5.1)$$

where the matrix $\mathbf{X}_\lambda^\dagger$ is defined in (4.12) for standard and in (4.15) for general form. The GCV function is composed of two inversely proportional parts, residual norm $\|\mathbf{X}\mathbf{y}_\lambda - \mathbf{b}\|_2^2$ and $\left(\text{trace}(\mathbf{I} - \mathbf{X}\mathbf{X}_\lambda^\dagger)\right)^{-2}$. The idea of the GCV method is that the regularized solution predicts the missing element b_i of the vector \mathbf{b} [34]. The denominator in Equation 5.1 can be replaced with the following [34]

$$\text{trace}(\mathbf{I} - \mathbf{X}\mathbf{X}_\lambda^\dagger) = q - (\ell - p) - \sum_{i=1}^p f_i \quad (5.2)$$

where f_i are filter factors for the corresponding method. From (5.2) it is obvious that $\left(\text{trace}(\mathbf{I} - \mathbf{X}\mathbf{X}_\lambda^\dagger)\right)^{-2}$ achieves minimal value for the largest possible λ . In addition, this value increases if (generalized) singular values of matrix \mathbf{X} increases.

5.1.2 L-curve

The L-curve algorithm [35] is designed to balance the residual norm $\|\mathbf{b} - \mathbf{X}\mathbf{y}_\lambda\|_2$ with the norm of the solution $\|\mathbf{y}_\lambda\|_2$ for Tikhonov in standard form, or seminorm $\|\mathbf{L}\mathbf{y}_\lambda\|_2$ for the general form case. These two parts are in most cases inversely proportional, so the curve defined as:

$$(\zeta(\lambda), \eta(\lambda)) = (\log \|\mathbf{b} - \mathbf{X}\mathbf{y}_\lambda\|_2, \log \|\mathbf{L}\mathbf{y}_\lambda\|_2) \quad (5.3)$$

has distinct L shape. The value of λ that maximizes the curvature

$$\kappa(\lambda) = \frac{\eta'(\lambda)\zeta''(\lambda) - \zeta'(\lambda)\eta''(\lambda)}{((\eta'(\lambda))^2 + (\zeta'(\lambda))^2)^{3/2}} \quad (5.4)$$

is defined as the L-curve's corner [33] and is chosen to be the regularization parameter. In this way, the compromise between minimization of residual norm and solution seminorm is achieved.

5.2 Adaptive Method based on Signal-loss and Noise Error

The adaptive algorithm based on the signal loss and noise error was used for determining the truncation parameter k for TSVD in [26] and TTLS in [9] and in Section 6.2. The parameter is found as a solution of the following minimization problem:

$$k = \min_{t \in \{1, 2, \dots, \ell\}} \left\{ \mathbf{b}^* (\mathbf{I} - \mathbf{X}\mathbf{X}_t^\dagger) \mathbf{b} + \sigma^2 \cdot \sum_{i=1}^t \frac{1}{\sigma_i^2} \right\} \quad (5.5)$$

where the matrix \mathbf{X}_t^\dagger is obtained from Equation (3.6) by replacing upper bound of summation with t . The rank of the matrix \mathbf{X} is denoted with ℓ , σ^2 is the variance of Gaussian white noise in the measured vector \mathbf{b} , and the σ_i are the singular values of \mathbf{X} . The left part of the argument in Equation (5.5) is named the signal loss error and the right part is noise error. Inspired by this idea, we develop an adaptive algorithm for both the standard and generalized form of Tikhonov regularization that estimates the norm of the noise, denoted with $\|\mathbf{e}\|_2$, rather than its variance. If we overestimate the norm of the error at the beginning of the algorithm, the DBI method simply requires more iterations to converge to the appropriate solution. The reason for this is that estimation of norm of the error, $\|\mathbf{e}_{DBI}^{(i)}\|_2$, is adaptively decreased in each iteration of DBI as:

$$\|\mathbf{e}_{DBI}^{(i)}\|_2 = \|\mathbf{e}\|_2 \cdot \frac{\|\mathbf{b}_{DBI}^{(i)}\|_2}{\|\mathbf{b}_{DBI}^{(i-1)}\|_2}, \quad (5.6)$$

where $\mathbf{b}_{DBI}^{(i)}$ denotes the right side vector of the inverse problem within the i^{th} iteration of DBI.

The following is the theoretical background for our algorithm. Since the measured vector \mathbf{b} holds errors \mathbf{e} , it follows:

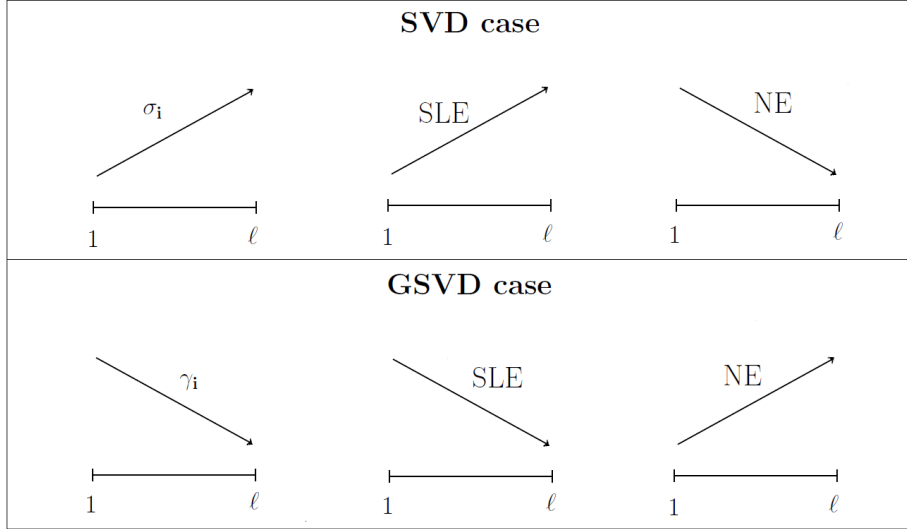


Figure 5.1: Decrease and increase of (generalized) singular values, Signal loss error (SLE) and Noise error (NE) in the proposed adaptive method.

$$\mathbf{X}\mathbf{y} \approx \mathbf{b} \Rightarrow \mathbf{y}_\lambda = \mathbf{X}_\lambda^\dagger \mathbf{b} = \mathbf{X}_\lambda^\dagger \mathbf{b}_{exact} + \mathbf{X}_\lambda^\dagger \mathbf{e}.$$

We define Noise Error (NE) as:

$$\text{NE}(\lambda) = \left\| \mathbf{X}_\lambda^\dagger \mathbf{e} \right\|_2. \quad (5.7)$$

In order to find effective formula for calculation of $\text{NE}(\lambda)$, we derive the following. First, for the SVD case, using the definition of $\mathbf{X}_\lambda^\dagger$ and the fact that matrices \mathbf{U} and \mathbf{V} are left orthogonal (i.e. $\mathbf{U}^* \mathbf{U} = \mathbf{V}^* \mathbf{V} = \mathbf{I}$ and $\|\mathbf{U}\|_2 = \|\mathbf{V}\|_2 = 1$), we have

$$\left\| \mathbf{X}_\lambda^\dagger \mathbf{e} \right\|_2 = \left\| \mathbf{V} \begin{pmatrix} f_1/\sigma_1 & & 0 \\ & \ddots & \\ 0 & & f_\ell/\sigma_\ell \end{pmatrix} \mathbf{U}^* \mathbf{e} \right\|_2 \leq \left\| \begin{pmatrix} f_1/\sigma_1 & & 0 \\ & \ddots & \\ 0 & & f_\ell/\sigma_\ell \end{pmatrix} \right\|_2 \cdot \|\mathbf{e}\|_2. \quad (5.8)$$

The upper bound for the noise error is given as:

$$\text{NE}_{\text{SVD}}(\lambda) \leq \max_i \left\{ \frac{f_i}{\sigma_i} \right\} \|\mathbf{e}\|_2 = \max_i \left\{ \frac{\sigma_i}{\sigma_i^2 + \lambda^2} \right\} \cdot \|\mathbf{e}\|_2. \quad (5.9)$$

For the GSVD case, we have:

$$\begin{aligned}
\|\mathbf{X}_\lambda^\dagger \mathbf{e}\|_2 &= \left\| \mathbf{Y} \begin{pmatrix} f_1/\alpha_1 & & 0 \\ & \ddots & \\ & & f_\ell/\alpha_\ell \\ 0 & & & \mathbf{I}_{\ell-p} \end{pmatrix} \mathbf{U}^* \mathbf{e} \right\|_2 \\
&\leq \|\mathbf{Y}\|_2 \left\| \begin{pmatrix} f_1/\alpha_1 & & 0 \\ & \ddots & \\ & & f_\ell/\alpha_\ell \\ 0 & & & \mathbf{I}_{\ell-p} \end{pmatrix} \right\|_2 \cdot \|\mathbf{e}\|_2,
\end{aligned} \tag{5.10}$$

leading to the upper bound

$$\text{NE}_{\text{GSVD}}(\lambda) \leq \|\mathbf{Y}\|_2 \cdot \max_i \left\{ \frac{\alpha_i}{\alpha_i^2 + \beta_i^2 \lambda^2}, 1 \right\} \cdot \|\mathbf{e}\|_2. \tag{5.11}$$

For the Signal Loss Error (SLE), we calculate the norm of the residual vector $\mathbf{r} = \mathbf{b} - \mathbf{X}\mathbf{y}_\lambda$ as:

$$\|\mathbf{b} - \mathbf{X}\mathbf{y}_\lambda\|_2^2 = \left\| (\mathbf{I} - \mathbf{X}\mathbf{X}_\lambda^\dagger) \mathbf{b} \right\|_2^2 = \mathbf{b}^* (\mathbf{I} - \mathbf{X}\mathbf{X}_\lambda^\dagger)^* (\mathbf{I} - \mathbf{X}\mathbf{X}_\lambda^\dagger) \mathbf{b}.$$

Since $(\mathbf{X}\mathbf{X}_\lambda^\dagger)^* = \mathbf{X}\mathbf{X}_\lambda^\dagger$, we define SLE as:

$$\text{SLE}(\lambda) = \sqrt{\mathbf{b}^* (\mathbf{I} - \mathbf{X}\mathbf{X}_\lambda^\dagger)^2 \mathbf{b}}. \tag{5.12}$$

Remark 5.2.1. The regularized inverse \mathbf{X}_k^\dagger in the case of TSVD and TGSVD satisfies Penrose condition $\mathbf{X}_k^\dagger \mathbf{X}\mathbf{X}_k^\dagger = \mathbf{X}_k^\dagger$, as seen in Chapter 4. Using this condition, we have

$$(\mathbf{I} - \mathbf{X}\mathbf{X}_k^\dagger)^2 = \mathbf{I} - \mathbf{X}\mathbf{X}_k^\dagger - \mathbf{X}\mathbf{X}_k^\dagger + \mathbf{X}\mathbf{X}_k^\dagger \mathbf{X}\mathbf{X}_k^\dagger = \mathbf{I} - \mathbf{X}\mathbf{X}_k^\dagger,$$

so the expression for SLE in the case TSVD and TGSVD is

$$\text{SLE}(\lambda) = \sqrt{\mathbf{b}^* (\mathbf{I} - \mathbf{X}\mathbf{X}_\lambda^\dagger) \mathbf{b}}. \tag{5.13}$$

In order to effectively calculate $\text{SLE}(\lambda)$, the product $\mathbf{X}\mathbf{X}_\lambda^\dagger$ can be replaced with the simpler form as:

$$\mathbf{X}\mathbf{X}_\lambda^\dagger = \mathbf{U} \begin{pmatrix} f_1 & & & \\ & \ddots & & \\ & & f_p & \\ & & & \mathbf{I}_{\ell-p} \end{pmatrix} \mathbf{U}^*. \quad (5.14)$$

Using Equations (5.12) and (5.14), we derive:

$$\text{SLE} = \mathbf{b}^* \left(\mathbf{I} - 2\mathbf{U} \begin{pmatrix} f_1 & & & \\ & \ddots & & \\ & & f_p & \\ & & & \mathbf{I}_{\ell-p} \end{pmatrix} \mathbf{U}^* + \mathbf{U} \begin{pmatrix} f_1^2 & & & \\ & \ddots & & \\ & & f_p^2 & \\ & & & \mathbf{I}_{\ell-p} \end{pmatrix} \mathbf{U}^* \right) \mathbf{b} \quad (5.15)$$

The $\text{SLE}_{(\text{G})\text{SVD}}$ can be calculated as:

$$\text{SLE}_{(\text{G})\text{SVD}}^2(\lambda) = \mathbf{b}^*\mathbf{b} + (\mathbf{U}^*\mathbf{b})^* \begin{pmatrix} f_1^2 - 2f_1 & & & \\ & \ddots & & \\ & & f_p^2 - 2f_p & \\ & & & \mathbf{I}_{\ell-p} \end{pmatrix} \mathbf{U}^*\mathbf{b}. \quad (5.16)$$

We note that in SVD case is $\ell = p$. The errors thus defined behave in an inverse proportion. With increasing the λ , SLE increases while NE decrease, as it is shown in Figure 5.1. The regularization parameter is found by minimizing the following cost function

$$\lambda = \min_{\lambda_i} \{ |\text{SLE}_{(\text{G})\text{SVD}}(\lambda_i) - \text{NE}_{(\text{G})\text{SVD}}(\lambda_i)| \}. \quad (5.17)$$

The candidates λ_i are chosen among (generalized) singular values since they need to satisfy the condition. More precisely, in our adaptive algorithm, we create a set of 400 candidates for λ_i that are uniformly distributed between the largest and the smallest (generalized) singular value. It is important that the value of λ_i does not exceed this range. Otherwise, the Tikhonov regularization will not be effective. We decided to chose 400 candidates as it is similarly implemented in the codes for GCV and L-curve from [34]. However, this number is optional.

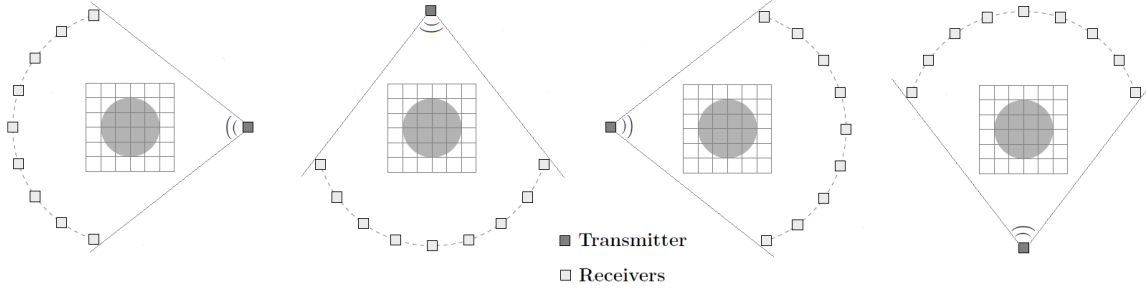


Figure 5.2: Presentation of the limited aperture setting where the wave is emitted from 64 different positions and collected with 57 receivers for the simulated phantom and 63 for the breast phantom.

5.3 Numerical results

To test the DBI with the aforementioned regularization methods, we simulated 128 equidistant transducers surrounding the ROI as shown in Figure 2.1. Two different settings were created. The first one is the full aperture setting where 32 out of 128 transducers emitted the ultrasound wave, one at a time, at a frequency of $f = 1$ MHz which corresponds to a wavelength $\lambda_0 = 1.4823$ mm in the background medium. The echo data was collected from all 128 transducers. The second setting is limited aperture setting where data was collected from limited number of transducers (receivers) as shown in Figure 5.2. We changed the position of the transmitter counterclockwise and the positions of receivers were changing accordingly. The reason why we created this setting is that it should reduce the computational time and the time needed to collect the data if it were to be used in the experimental environment.

The reconstruction of two different grayscale images of the ROI, shown in Figure 5.3, were preformed. First one is the simulated phantom, where the central oval has the value of contrast of 3%, and the rest of them are 5%, 8% and 9%. The second one is breast phantom which was extracted from numerical phantoms database [51].

Numbers of transmitters (M_t) and receivers (M_r) used in the full and limited aperture setting, with the domain size and the length of one pixel (w) are presented in Table 5.1. Since the DBI method is iterative, we used the Born approximation to initialize it and then we ran 10 iterations. Two different noise levels were tested, 20 dB and 30 dB.

For the regularization of the inverse problem, we used Tikhonov regularization meth-

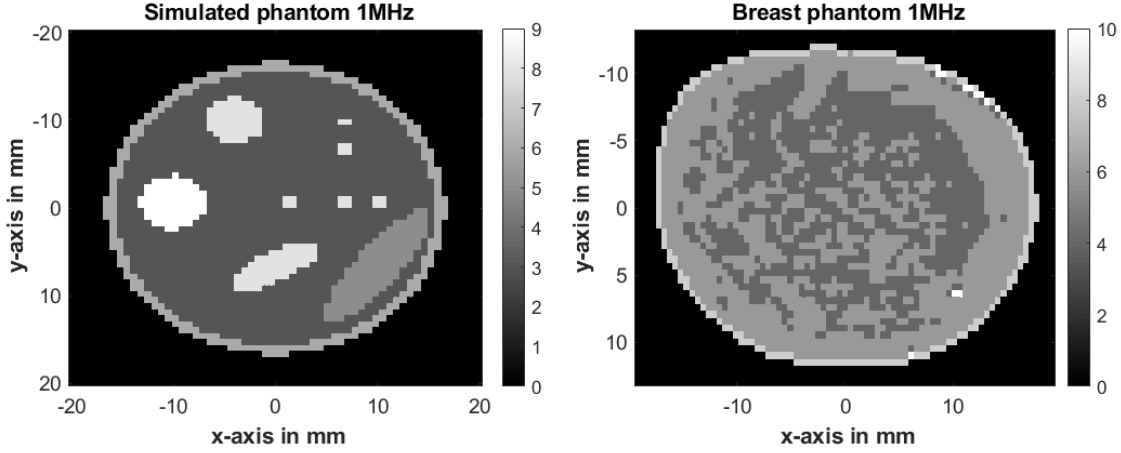


Figure 5.3: Exact simulated phantom and breast phantom used in simulations with frequency of 1MHz. The distribution of speed of sound is shown as percentage increase over background medium.

Table 5.1: Number of transmitters (M_t) and receivers (M_r) used in full and limited aperture setting.

Scattering object	Frequency	No. of pixels	w	Setting	M_t	M_r
Simulated phantom	1 MHz	60×60	0.67	Full aperture	32	128
				Limited aperture	64	57
Breast phantom	1 MHz	52×77	0.5	Full aperture	32	128
				Limited aperture	64	63

ods in standard and general form. Since these methods require regularization parameter λ , we utilized three different algorithms for obtaining the regularization parameter: L-curve, GCV and our proposed adaptive algorithm. All numerical tests were performed in MATLAB (The Mathworks Inc., Natick, MA, USA) with a four core processor Intel I7 with 32 GB of RAM. In order to quantitatively measure the quality of the reconstructed image, we calculated the relative error of the reconstructed scattering function in ℓ_2 norm ($RE-\ell_2$) as defined in the Equation (4.22). We have described in Section 2.4 that the iterations of the DBI method stops when the relative error for the calculated scattered field drops below prescribed tolerance. However, in order to analyze weather the DBI is converging or diverging with each method, we have decided to look at the problem differently. We ran 10 iterations of the DBI for all presented cases (each regularization method with different algorithms to choose the regularization parameter λ).

Table 5.2: RE- ℓ_2 for Born approximation and after 10 iterations of DBI in full aperture setting.

Scattering object	Tikhonov form	SNR	L-curve	GCV	Adaptive
			Born \rightarrow DBI	Born \rightarrow DBI	Born \rightarrow DBI
Simulated phantom	Standard	30 dB	0.2897 \rightarrow 1.2387	0.1910 \rightarrow 0.1851	0.2113 \rightarrow 0.1597
		20 dB	0.5379 \rightarrow 2.2043	0.2831 \rightarrow 0.2845	0.3871 \rightarrow 0.2580
	General	30 dB	0.2988 \rightarrow 1.2230	0.2215 \rightarrow 0.2124	0.2282 \rightarrow 0.1731
		20 dB	0.5066 \rightarrow 2.4191	0.3088 \rightarrow 0.3088	0.3252 \rightarrow 0.2875
Breast phantom	Standard	30 dB	0.2511 \rightarrow 7.4295	0.2293 \rightarrow 0.2266	0.2268 \rightarrow 0.2086
		20 dB	0.4512 \rightarrow 8.0587	0.3014 \rightarrow 0.3042	0.3404 \rightarrow 0.2960
	General	30 dB	0.2224 \rightarrow 7.2417	0.2065 \rightarrow 0.2049	0.2144 \rightarrow 0.1684
		20 dB	0.3723 \rightarrow 8.3439	0.2666 \rightarrow 0.2664	0.2919 \rightarrow 0.2568

Table 5.2 shows the values of RE- ℓ_2 for Born approximation and the final 10th iteration of DBI for all tested cases in the full aperture setting. Although all three algorithms for finding λ produced RE- ℓ_2 less than 0.55 for the Born approximation, only our proposed adaptive algorithm has significantly decreased RE- ℓ_2 after 10 iterations of DBI in regard to initial Born approximation. GCV has obtained good regularization parameter λ for Born, however, it failed to provide improvement by using the DBI method. On the other hand, L-curve produced the values of RE- ℓ_2 for DBI that are greater than 1. It is visible from Table 5.2 that the lowest values of RE- ℓ_2 in the 10th iteration of DBI for all tested cases are achieved by using our proposed adaptive algorithm.

Values of RE- ℓ_2 through 10 iterations of DBI for the full and limited aperture settings are presented in Figure 5.4. Cases shown in this plots are Tikhonov in standard and general form with regularization parameters λ obtained using GCV and the proposed adaptive algorithm. We did not include results for the L-curve algorithm as the values of RE- ℓ_2 were much greater than the limits of vertical axis which is visible from Table 5.2. It is obvious that the proposed adaptive algorithm provided the lowest relative error, while GCV failed to provide appropriate λ for the DBI method. In addition, Tikhonov in standard form produced lower error for the simulated phantom, while the general form worked better for the breast phantom. Figure 5.5 shows values of parameter λ obtained with three tested algorithms during 10 iterations of DBI for simulated phantom. We did

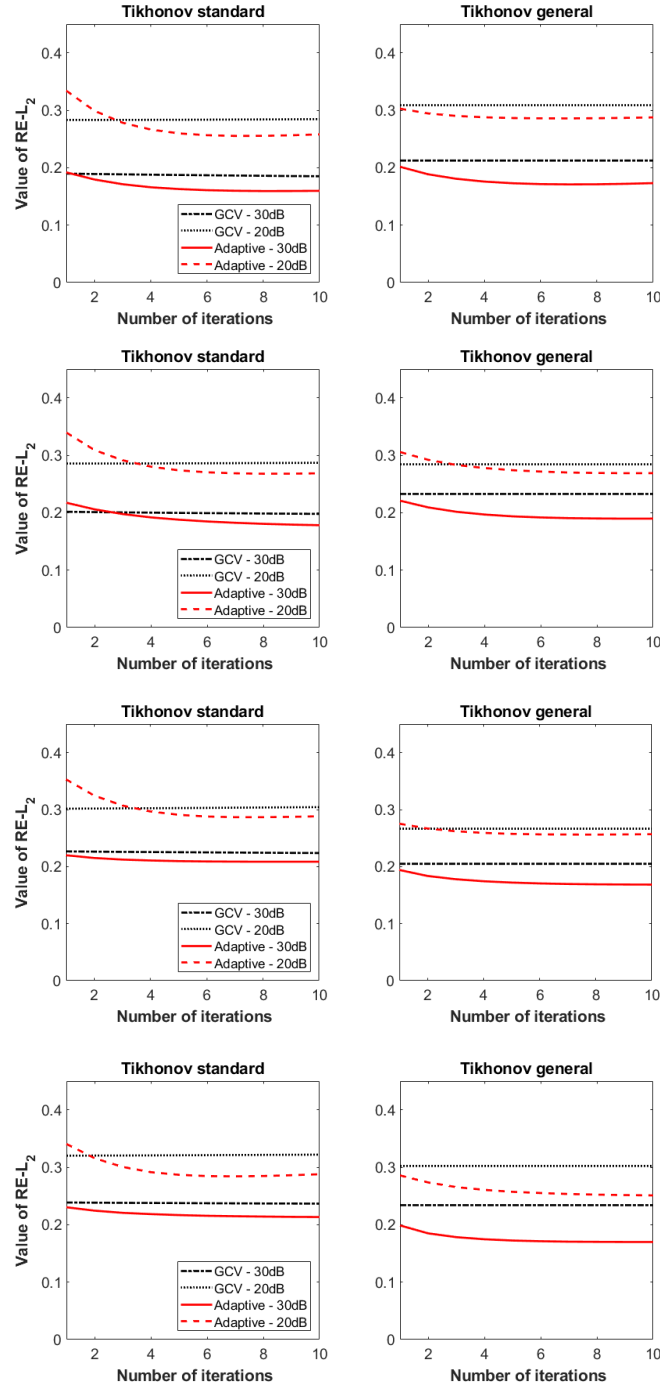


Figure 5.4: Plots of the relative error ($\text{RE-}\ell_2$) for the scattering function during 10 iterations of DBI for simulated (top four images) and breast phantom (bottom four images) in the full and limited aperture setting. The frequency is $f = 1$ MHz and tested noise levels are 20 and 30 dB, respectively. All combinations between Tikhonov regularization in standard (left) and in general form (right) with algorithms for obtaining the parameter (GCV, L-curve and adaptive) are tested. However, the results for the L-curve are not included in these plots since the values of $\text{RE-}\ell_2$ are larger than 1.

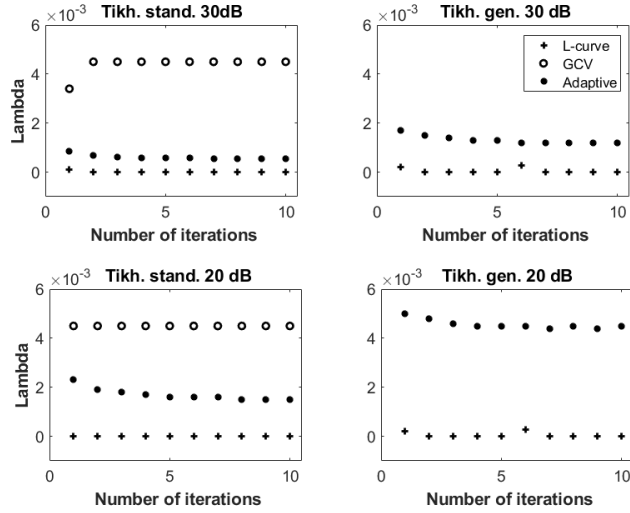


Figure 5.5: Values of regularization parameter λ during 10 iterations of DBI obtained with three different algorithms: L-curve, GCV and the proposed adaptive algorithm. The scattering object is simulated phantom and noise levels are 30 (top images) and 20 dB (bottom images). Values provided with the GCV algorithm for Tikhonov in general form weren't included in the graphs since they were too large, 100.2864 for 30 dB and 100.3179 for 20 dB.

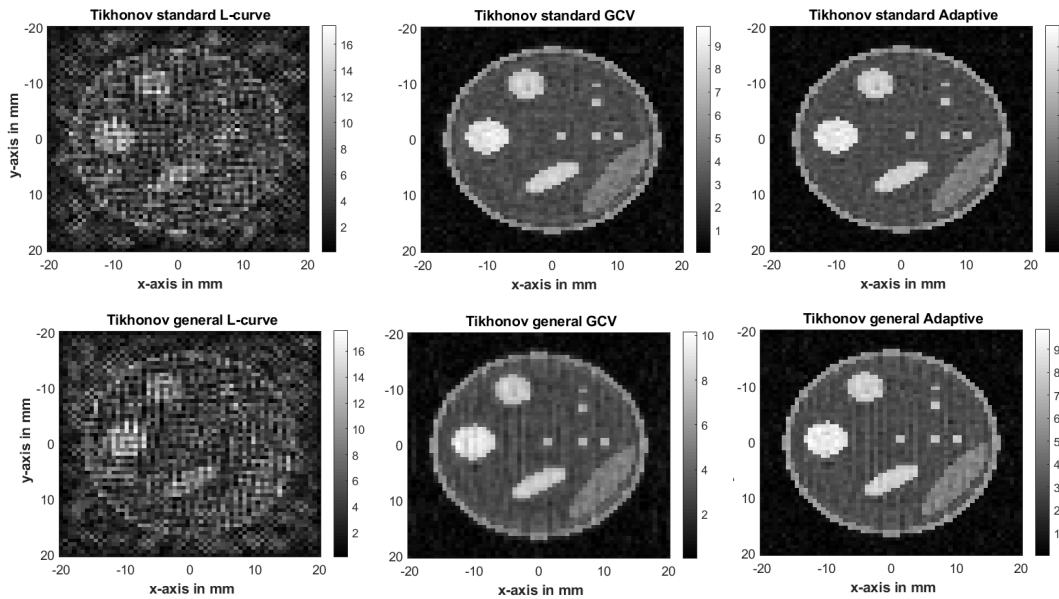


Figure 5.6: The reconstructed images of simulated phantom after 10 iterations of DBI for 30 dB noise. Methods used for regularization are Tikhonov in standard (top) and general (bottom) form, while λ is obtained with L-curve (left), GCV (middle) and proposed adaptive algorithm (right). The frequency used is 1 MHz.

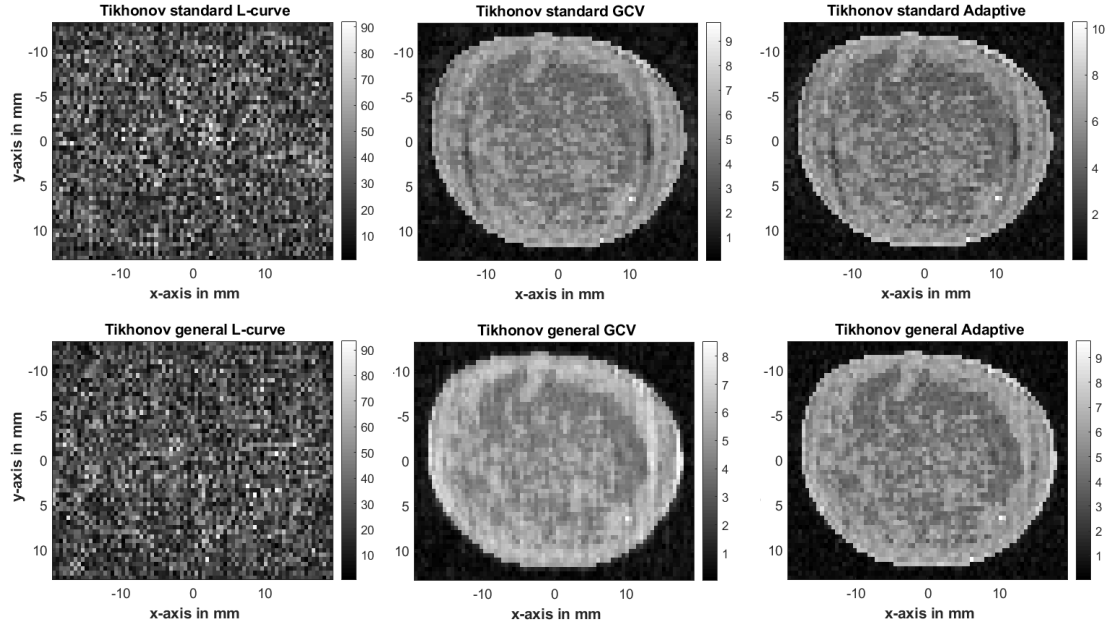
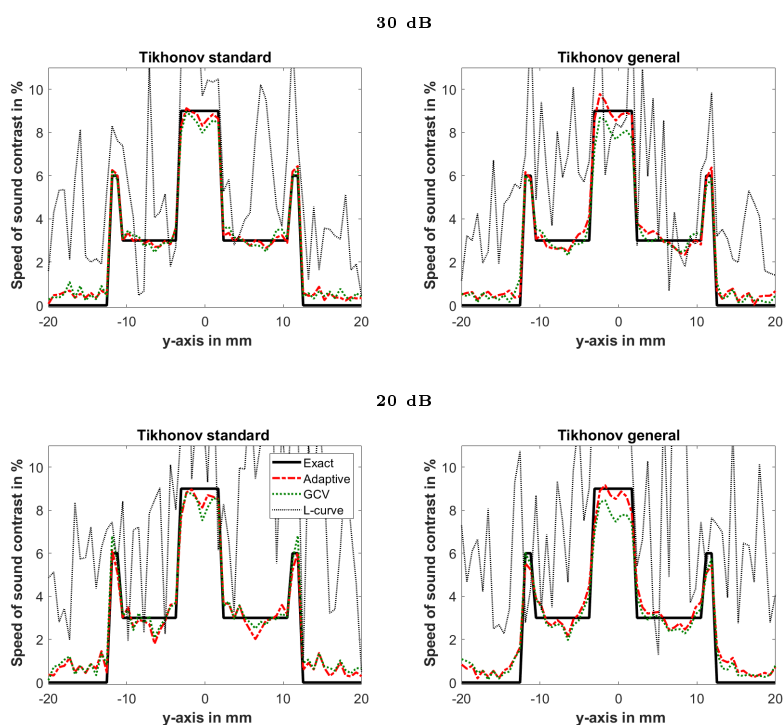


Figure 5.7: The reconstructed images of breast phantom after 10 iterations of DBI for 30 dB noise. Methods used for regularization are Tikhonov in standard (top) and general (bottom) form, while λ is obtained with L-curve (left), GCV (middle) and proposed adaptive algorithm (right). The frequency used is 1 MHz.

not include values provided with the GCV algorithm for Tikhonov in general form since they were larger compared to the limits of vertical axis. We would like to note that the values were the same in each iteration, that is, 100.2864 for 30 dB and 100.3179 for 20 dB noise level. The regularization parameter λ obtained with the L-curve is shown to be the smallest which indicates they are not suitable for a given problem. Parameters obtained with GCV tend to be much larger than those obtain with other algorithms. As shown, parameters obtained using the adaptive algorithm are gradually decreasing with each iteration of DBI. We would like to note that, although we presented values of λ only for simulated phantom in Figure 5.5, similar situation occurred for the breast phantom.

Reconstructed images of simulated and breast phantom with 30 dB noise after 10 iterations of DBI are shown in Figures 5.6 and 5.7 respectively. All combinations of regularization methods and algorithms for obtaining the regularization parameter λ are presented. It is noticeable that L-curve failed to provide a visible reconstructed image from each original form (simulated and breast phantom images). In addition, when our proposed adaptive algorithm is used, images are clearer and the scatterer are more distinct

Simulated phantom - Full aperture



Breast phantom - Full aperture

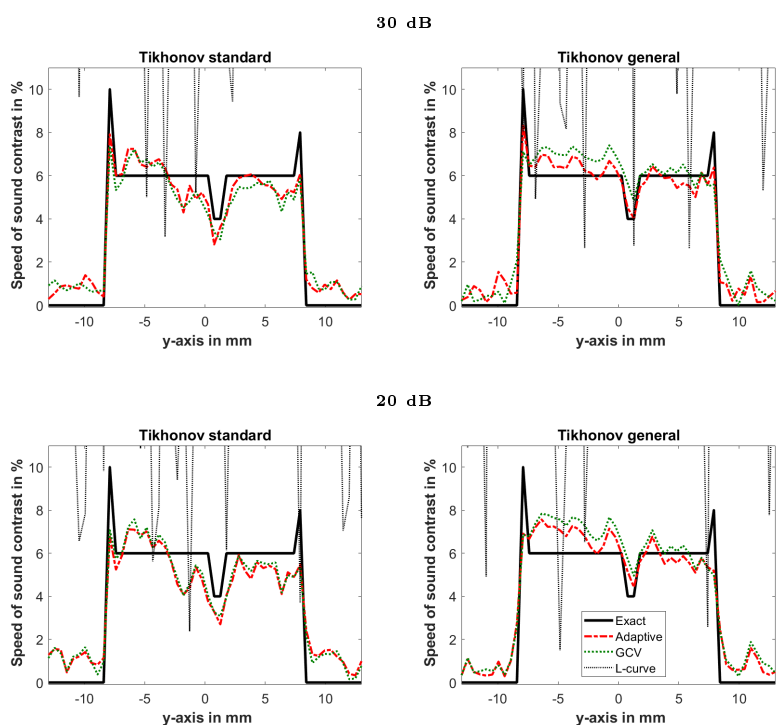
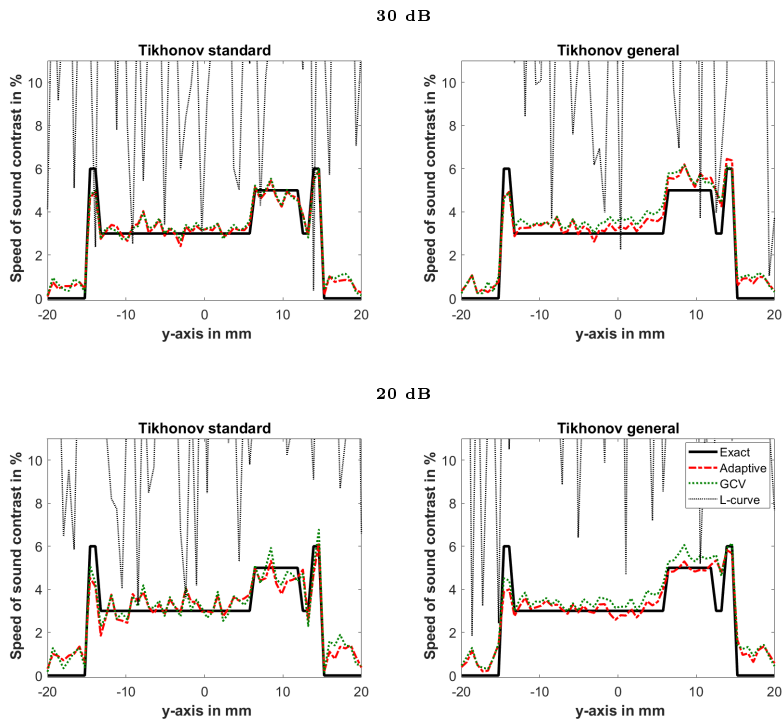


Figure 5.8: Vertical slice plot at $x = -10.72$ mm of simulated phantom (top four) and at $x = 13.5$ mm of breast phantom (bottom four) after 10 iterations of DBI for frequency of 1 MHz in full aperture setting. Inverse problem is regularized with Tikhonov in standard form (left) and general form (right).

Simulated phantom - Limited aperture



Breast phantom - Limited aperture

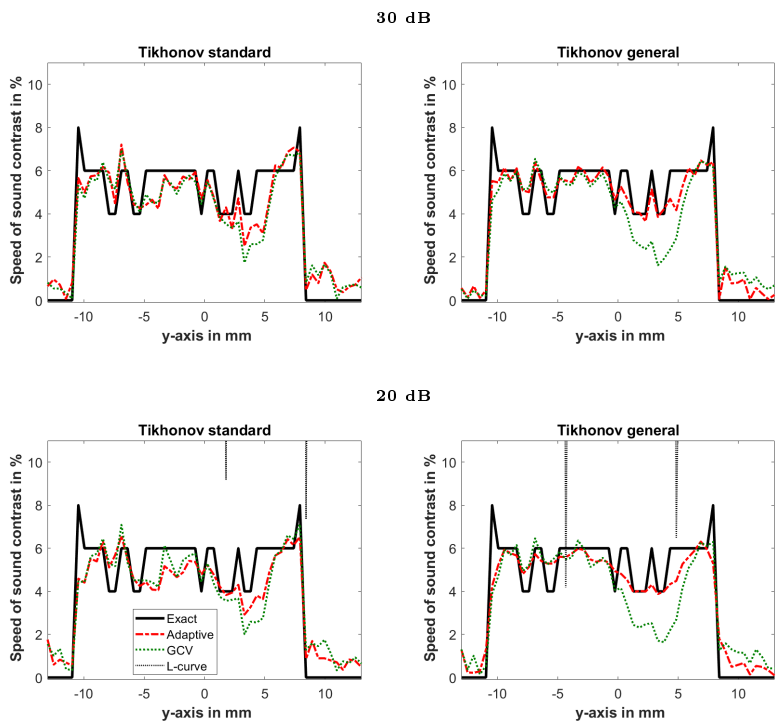


Figure 5.9: Vertical slice plot at $x = 8.04$ mm of simulated phantom (top four) and at $x = -12$ mm of breast phantom (bottom four) after 10 iterations of DBI in limited aperture setting. Inverse problem is regularized with Tikhonov in standard form (left) and general form (right).

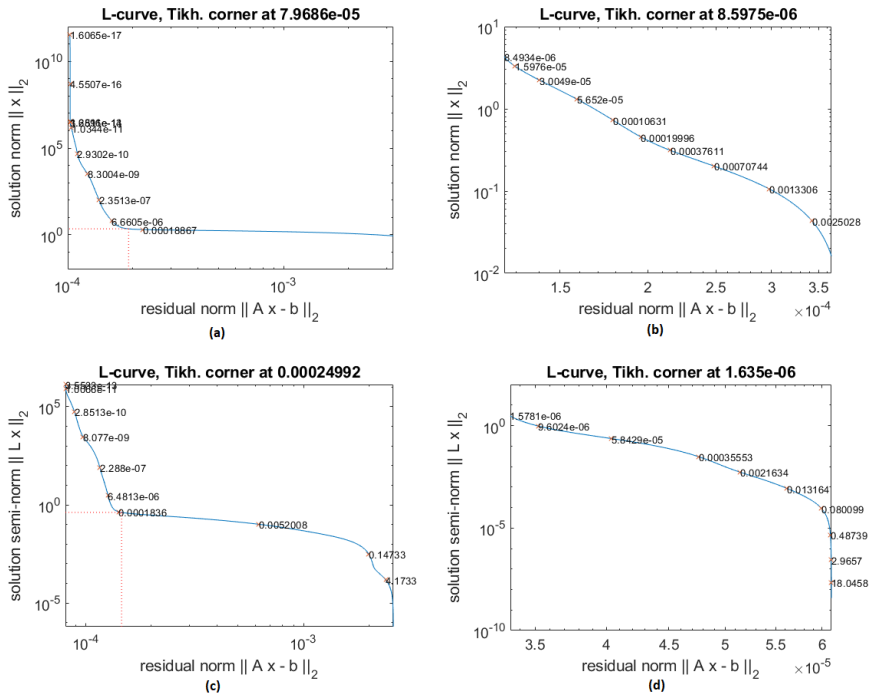
than with GCV (exact values are shown earlier in Table 5.2 and Figure 5.4). Furthermore, to show the benefit of using our proposed adaptive algorithm, we compared the slice plots side by side of tested phantoms as shown in Figures 5.8 and 5.9. These plots were obtained from the reconstructed ROI after 10 iterations of DBI. Top four images of Figure 5.8 show the slice plots of the vertical line with fixed x-axis at -10.72 mm that we took from the simulated phantom in the full aperture setting. In addition, for the breast phantom, we took the vertical line fixed at $x=13.5$ mm as presented in bottom four images on Figure 5.8. For the limited aperture setting, top four images on Figure 5.9 show the slice plot of the vertical line fixed at $x=8.04$ mm for the simulated phantom. For the breast phantom, we took vertical line at $x= -12$ mm, presented in bottom four images on Figure 5.9. Results obtained with L-curve are not visible in the images for 30 dB and only glitches are visible for 20dB. The reason for this is that those values are much larger than the scale on the axis. These plots show the effect of the inhomogeneity on the reconstruction of the ROI. It is obvious that, for the Tikhonov in general form, the proposed adaptive algorithm is able to track the changes of the image values more precisely than GCV and L-curve. For Tikhonov in standard form the differences are slightly lower, however, the adaptive algorithm is still better.

These results validated the benefit of using our proposed adaptive algorithm over L-curve and GCV for choosing the regularization parameter λ . This λ is essential for Tikhonov regularization incorporated within the DBI method. Although L-curve and GCV algorithms are effective for a variety of problems, including some cases of Born approximation (Table 5.2), they failed when utilized within the DBI method, resulting in a lower image quality comparable to our proposed algorithm.

All three tested algorithms are composed of two parts. The first one is the residual norm $\|\mathbf{b} - \mathbf{X}\mathbf{y}_\lambda\|_2$ which is a common feature for all three algorithms. It achieves its minimum for the smallest possible λ and we referred to it as signal loss error. However, the second part is different for these three algorithms and it achieves its minimum for the largest possible λ . Therefore, depending on this second part, algorithms will choose different values for regularization parameter λ .

The L-curve algorithm tends to obtain a very small regularization parameter λ in each iteration as shown in Figure 5.5. As a consequence, the solution is underregularized and

L-curve plot



Plot of GCV function

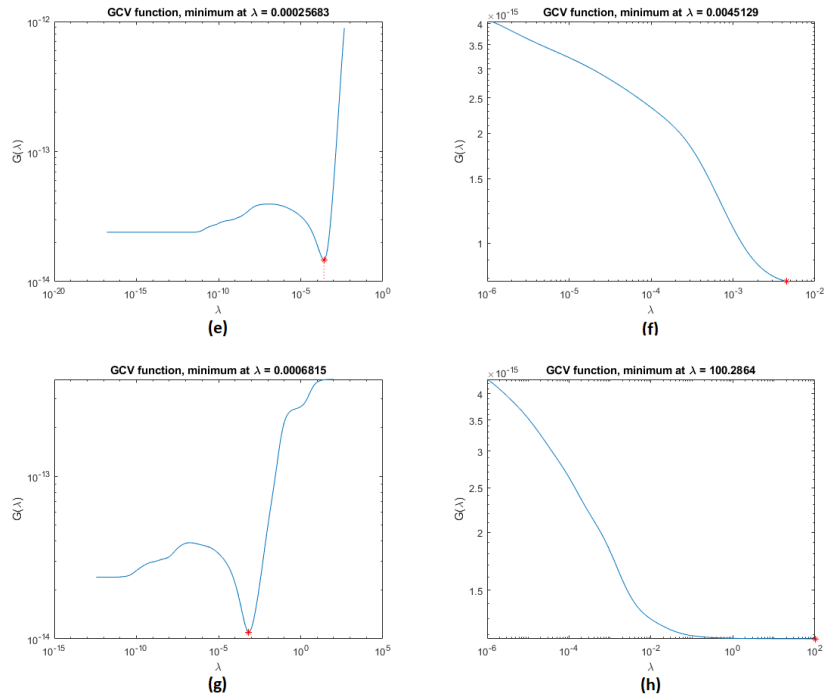


Figure 5.10: L-curve plot (top four) and plot of the GCV function (bottom four) used for finding regularization parameter λ when Tikhonov in standard (a,b,e,f) and general form (c,d,g,h) is used for regularization in Born approximation (a,c,e,g) and in DBI (b,d,f,h) for simulated phantom. L-curve and GCV plots in the case of breast phantom are not included in this Figure since they are very similar to the presented plots for the simulated phantom.

DBI diverged in both cases of noise values (20 and 30 dB) as shown in Table 5.2 and Figures 5.6 and 5.7. In the case of Born approximation, the curve has distinctive L shape (Figure 5.10 (a) and (c)). This reveals that there is a balancing between residual and solution norms and none of them is dominant. That is why, in this case, the obtained regularization parameter λ using L-curve provides a solution with acceptable relative error as already explained. However, for the regularization within the iteration of the DBI method, the curve doesn't have the L shape (Figure 5.10 (b) and (d)). The reason for this is that the second part ($\|\mathbf{y}_\lambda\|_2$) for Tikhonov regularization in standard form is equal to $\|\Delta\mathbf{s}\|_2$ inside the DBI method. This value, $\|\mathbf{y}_\lambda\|_2$, is already very small compared to the residual norm so it has been neglected during the process of minimization. Accordingly, the obtained parameter λ has a small value with each iteration as it only minimized the residual norm. For the general form case, $\|\mathbf{L}\Delta\mathbf{s}\|_2$ is even smaller, which results in a choice of much smaller value of λ that negatively affects the image quality.

On the other hand, the problem with GCV is that the value of the obtained regularization parameter λ is too high as shown in Figure 5.5. Because of that, when the inverse part (Equation (2.16)) was solved using the obtained λ , the solution (the update for the scattering function $\Delta\hat{\mathbf{s}}$) was overregularized and approximately equal to 0 within iterations inside the DBI method. As a result, the relative error (RE- ℓ_2) always has a constant value as shown in Table 5.2 and Figure 5.4. In the case of Born approximation, the GCV function has a local minimum somewhere in the middle of the graph as shown in Figure 5.10 (e) and (g). For the DBI case, the GCV function is monotonically decreasing and the minimum function value is achieved at the end of the x-axis as shown in Figure 5.10 (f) and (h). This happened because the value of of the second part of Equation (5.1), $\left(\text{trace}(\mathbf{I} - \mathbf{X}\mathbf{X}_\lambda^\dagger)\right)^{-2}$, increased during iterations of the DBI method compared to its previous value in the Born approximation. So, when we minimize the GCV function, we actually are minimizing $\left(\text{trace}(\mathbf{I} - \mathbf{X}\mathbf{X}_\lambda^\dagger)\right)^{-2}$ as it achieves much higher values than the residual norm $\|\mathbf{b} - \mathbf{X}\mathbf{y}_\lambda\|_2$. This leads to chose the highest possible value of λ . The performance of L-curve and GCV algorithms when used inside the DBI method was examined in [42]. Though, they have used different test phantoms and different basis functions for discretization.

The best results are achieved when regularization parameter λ is chosen using our

proposed adaptive algorithm. The value of the parameter is neither too large nor too small, as shown in Figure 5.5. It provides an optimal balance between overregularized and underregularized solutions. As a consequence, the DBI method converged in all tested cases. Our proposed algorithm starts with a rough estimate of the norm of the noise for Born approximation. Then, our algorithm benefits from the design of the DBI method since in each iteration the discrepancy between the measured and the calculated data is reduced. We use this information to decrease the estimate of the noise which we called the noise error. Its value is neither too high nor too low compared to the residual norm, unlike in L-curve or GCV case. That is why both parts of our algorithm are minimized and as a consequence, it chooses a better value for λ which results in a higher quality reconstructed images.

In some cases for the Born approximation, GCV provided lower value for RE- ℓ_2 than the adaptive algorithm as visible in Table 5.2. However, this was due to an initial overestimation of the noise norm in the proposed algorithm which has been adjusted within the iterations of the DBI method. In addition, inside the DBI method, GCV failed to provide an appropriate choice of λ . However, our proposed algorithm succeeded to decrease the relative error, RE- ℓ_2 , with each iteration, resulting in the lowest relative error in all tested cases and better reconstructed images.

Figures 5.6 and 5.7 also confirmed the benefit of using our proposed algorithm for choosing the regularization parameter λ . We would like to note that although Tikhonov in standard form produced slightly better reconstruction for simulated phantom, Tikhonov in general form proved to have better reconstruction image when more realistic medium was used (breast phantom) as shown in Figure 5.7.

The slice plots presented in Figures 5.8 and 5.9 provided a valuable insight in the quality of the reconstructed images. In most of the tested cases, our adaptive algorithm achieved a better reconstruction of the presented phantoms. In addition, it captured the sudden change in the values much better as we can see in Figure 5.8. It is also visible that the reconstructed breast phantom in limited aperture setting (Figure 5.9) was closest to the ground truth when our adaptive algorithm was employed for Tikhonov in general form, while GCV failed to reconstruct values when rapid change occurs from $y = -5$ mm to $y = 5$ mm.

Chapter 6

Different Approaches to Total Least Squares

Total least squares (TLS) is a method of fitting that has been known in the statistic under the names orthogonal regression or errors in variable regression. It was introduced in the field of numerical analysis by Golub and Van Loan in [23] where they proposed an algorithm for solving TLS problem using singular value decomposition. Regularization properties of truncated TLS were demonstrated in [18] making it a desirable regularization method.

A short overview of TLS is presented in Section 6.1. The difference between least squares method and TLS is that, in addition to the noise in the measured data, TLS also assumes errors in the operator matrix \mathbf{X} . The TLS approach could be beneficial for regularization of inverse problem within DBI method since matrix \mathbf{X} is composed of approximations for the Green's functions and the total field. Therefore it is a reasonable assumption that \mathbf{X} is given with errors. Section 6.2 presents adaptive truncated total least squares, where truncation parameter k is found using similar idea as described in Chapter 5. Regularized TLS (RTLS) method is presented in Section 6.3. This is a modification of Tikhonov regularization, presented in Chapter 4 where it solves the least squares problem, to solve the total least squares problem. In Section 6.4 we describe RTLS-Newton method where the problem of finding parameters for RTLS is solved using Newton method. In addition, numerical results comparing TLS and RTLS-Newton, when utilized for regularization in UT, are presented. Finally, projection based regularized total

least squares method is described in Section 6.5 and its robustness to increased noise levels is compared with TLS.

6.1 Truncated Total Least Squares

The total least squares (TLS) method is suited for solving the overdetermined linear system given in Equation (3.7) when errors are considered both in system matrix \mathbf{X} and the right-hand side vector \mathbf{b} . The idea of TLS is to find matrix $\widehat{\mathbf{X}}$ and vector $\widehat{\mathbf{b}}$ as a small perturbations of \mathbf{X} and \mathbf{b} , that is

$$\min_{\widehat{\mathbf{X}}, \widehat{\mathbf{b}}} \left\| (\mathbf{X}, \mathbf{b}) - (\widehat{\mathbf{X}}, \widehat{\mathbf{b}}) \right\|_F^2 \quad (6.1)$$

with the condition $\widehat{\mathbf{b}} \in \mathcal{R}(\widehat{\mathbf{X}})$ satisfied, where $\mathcal{R}(\widehat{\mathbf{X}})$ denotes the range of matrix $\widehat{\mathbf{X}}$ and $\|\cdot\|_F$ denotes the Frobenius norm. We will include in the following the basic TLS method, more details can be found in reference [69]. From Equation (3.7) it follows

$$(\mathbf{X}, \mathbf{b}) \begin{pmatrix} \mathbf{y} \\ -1 \end{pmatrix} = 0. \quad (6.2)$$

In order for the last equation to hold, vector $\begin{pmatrix} \mathbf{y} \\ -1 \end{pmatrix}$ must be an element of the null space of the matrix (\mathbf{X}, \mathbf{b}) . However, when this matrix has full rank, its null space contains only zero vector and this requirement cannot be satisfied. Accordingly, singular value decomposition (SVD) of augmented matrix $(\mathbf{X}, \mathbf{b}) = \mathbf{U}\Sigma\mathbf{V}^* = \sum_{i=1}^{N+1} \sigma_i \mathbf{u}_i \mathbf{v}_i^*$ is used

to obtain matrix $(\widehat{\mathbf{X}}, \widehat{\mathbf{b}}) = \sum_{i=1}^N \sigma_i \mathbf{u}_i \mathbf{v}_i^*$ with null space spanned with vector \mathbf{v}_{N+1} . In addition, according to Theorem 3.1.2, matrix $(\widehat{\mathbf{X}}, \widehat{\mathbf{b}})$ is the best rank- N approximation of matrix (\mathbf{X}, \mathbf{b}) in the Frobenius norm. The minimum-norm TLS solution is now obtained as:

$$\mathbf{y}_{TLS} = \frac{-1}{\mathbf{v}_{N+1, N+1}} \cdot \begin{pmatrix} \mathbf{v}_{1, N+1} \\ \vdots \\ \mathbf{v}_{N, N+1} \end{pmatrix} \quad (6.3)$$

where $\mathbf{v}_{i, N+1}$ denotes i^{th} element of vector \mathbf{v}_{N+1} . It is obvious that this method produces a solution of a slightly perturbed linear system $\widehat{\mathbf{X}}\mathbf{y} = \widehat{\mathbf{b}}$. When matrix \mathbf{X} has singular

values that decay gradually to zero, the problem is ill-posed, so truncation parameter k needs to be used to produce the solution. In this case, we refer to the method as truncated total least squares (TTLS) [18].

Here, we will present a short overview of the method, more details can be found in [18] and [69]. The first step is to find SVD of the augmented matrix (\mathbf{X}, \mathbf{b}) .

The second step is to choose the truncation parameter k that satisfies two conditions, $\sigma_k > \sigma_{k+1}$ and $\mathbf{V}_{22} \neq 0$, where the matrix \mathbf{V}_{22} is obtained from partitioning the matrix $\mathbf{V} \in \mathbb{C}^{(N+1) \times (N+1)}$ as:

$$\mathbf{V} = \begin{matrix} & k & N - k + 1 \\ \begin{matrix} N \\ 1 \end{matrix} & \begin{pmatrix} \mathbf{V}_{11} & \mathbf{V}_{12} \\ \mathbf{V}_{21} & \mathbf{V}_{22} \end{pmatrix} \end{matrix}.$$

Following the same idea, the solution belongs to a null space which is spanned by the last $N - k + 1$ columns of the matrix \mathbf{V} and the minimum-norm TTLS solution can be found as

$$\mathbf{y}_{TTLS} = -\mathbf{V}_{12} \mathbf{V}_{22}^\dagger = -\frac{\mathbf{V}_{12} \mathbf{V}_{22}^*}{\|\mathbf{V}_{22}\|_2^2},$$

where \mathbf{V}_{22}^\dagger denotes the pseudoinverse of \mathbf{V}_{22} . The parameter k is responsible for the truncation of the smallest singular values that can be highly affected by noise.

In order to show regularization properties of TTLS, its form as direct regularization method was introduced in [18] using filter factors defined as:

$$f_i = \sum_{j=k+1}^{N+1} \frac{v_{N+1,j}^2}{\|\mathbf{V}_{22}\|_2^2} \cdot \frac{\bar{\sigma}_i^2}{\bar{\sigma}_i^2 - \sigma_j^2} = \sum_{j=1}^k \frac{v_{N+1,j}^2}{\|\mathbf{V}_{22}\|_2^2} \cdot \frac{\bar{\sigma}_i^2}{\sigma_j^2 - \bar{\sigma}_i^2} \quad (6.4)$$

where $\bar{\sigma}_1 > \dots > \bar{\sigma}_N$ are singular values of matrix \mathbf{X} .

However, there are several problems with the TTLS method:

1. TTLS solution can be sensitive to noise, so additional regularization may be required.
2. TTLS requires the complete SVD of matrix (\mathbf{X}, \mathbf{b}) which can be time consuming for large matrices.

3. Different methods of a choice for parameter k have been proposed (GCV [42], [22], L-curve[42], [35]), but they increase the computational cost and none of them suits all cases of the problems solved using TTLS.

6.2 Adaptive truncated total least squares

In order to increase the effectiveness of the DBI and TTLS, we adopt appropriate algorithm for searching the truncation parameter k in each iteration of DBI. It is based on minimizing the following expression:

$$k = \min_{\ell \in \{1, \dots, n\}} \left\{ \mathbf{b} \left(\mathbf{I} - (\mathbf{X}, \mathbf{b}) (\mathbf{X}, \mathbf{b})_{\ell}^{\dagger} \right) \mathbf{b}^* + \sigma^2 \sum_{i=1}^{\ell} \frac{1}{\sigma_i^2} \right\} \quad (6.5)$$

where σ^2 is the variance of the Gaussian white noise, σ_i are singular values of matrix (\mathbf{X}, \mathbf{b}) , while $(\mathbf{X}, \mathbf{b})_{\ell}^{\dagger}$ is defined as:

$$(\mathbf{X}, \mathbf{b})_{\ell}^{\dagger} = \sum_{i=1}^{\ell} \frac{1}{\sigma_i} \mathbf{v}_i \mathbf{u}_i^*.$$

Since we are finding the truncation parameter k for the TTLS, the SVD of the augmented matrix (\mathbf{X}, \mathbf{b}) is used. First part of the argument in Equation (6.5) presents the signal loss error and it decreases when more singular values are used, while the second part is noise error and it decreases when less singular values is used. In this way the optimal parameter for TTLS is used in each iteration of DBI resulting with balance between this two errors.

6.2.1 Numerical results

To test the DBI with TTLS as a regularization method, we simulated 128 equidistant transducers surrounding the ROI. We have 32 out of 128 transmitting the wave, one at a

Table 6.1: Values of truncation parameter obtained using adaptive method

Iteration	1	2	3	4	5	6	7	8	9	10
$k =$	1415	1854	1698	2501	2261	2196	2170	2901	2598	2452

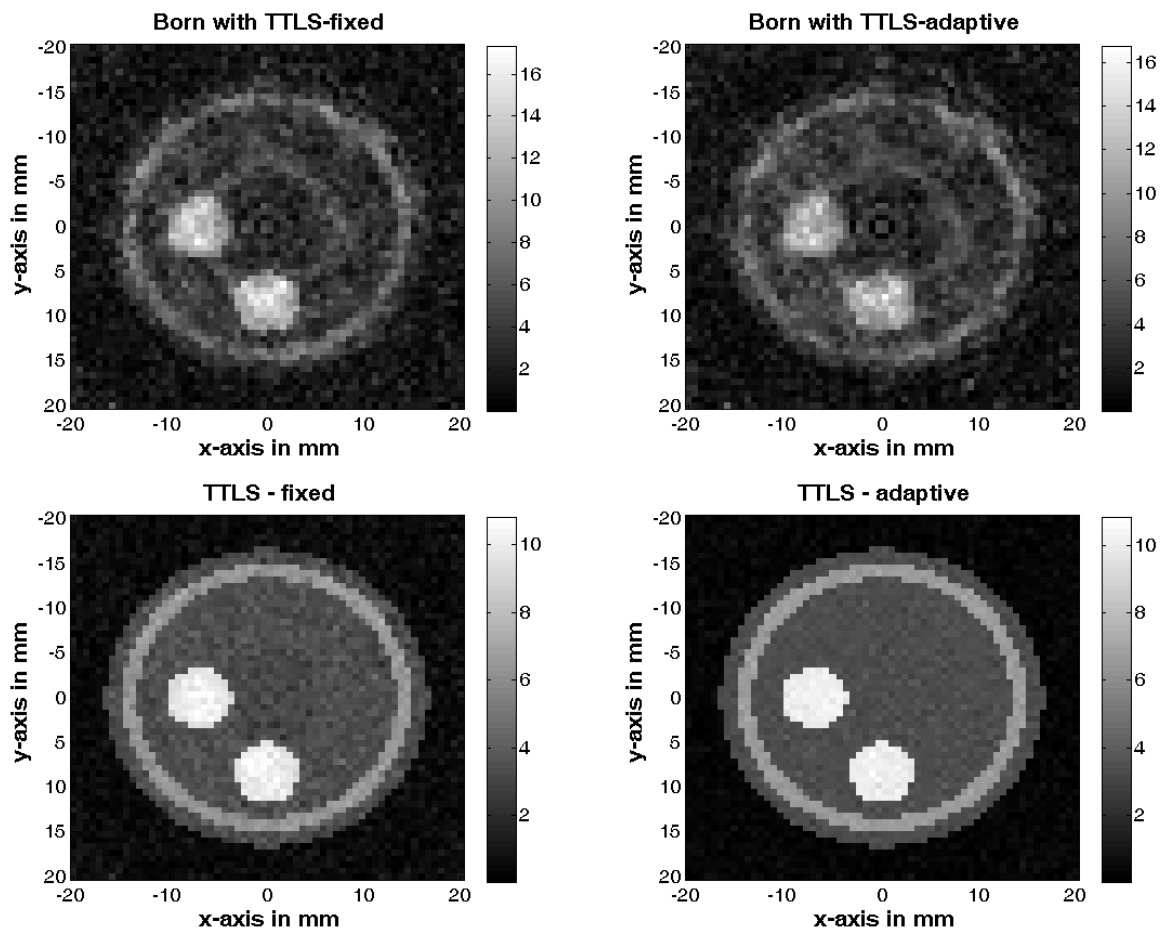


Figure 6.1: Reconstructed phantom using Born approximation (top) and after 10 iterations of DBI (bottom).

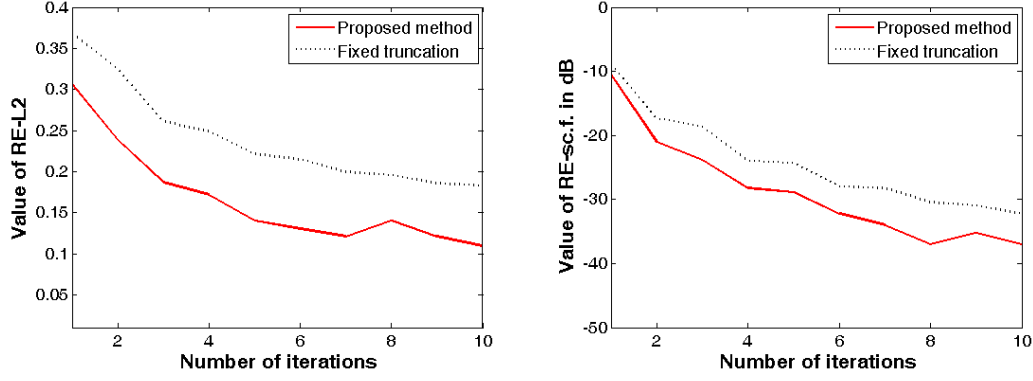


Figure 6.2: Plots of relative errors for scattering function (left) and scattered field (right).

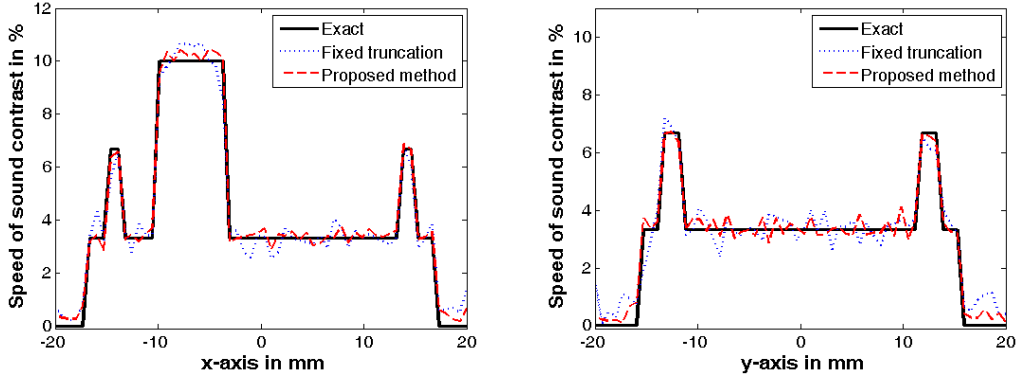


Figure 6.3: Slice plots of scattering function after 10 iterations of DBI. Horizontal slice at $y = 0$ mm (left) and vertical slice at $x = 6.67$ mm (right).

time, at a frequency of $f = 1$ MHz which is corresponding to a wavenumber $k_0 = 4.244$ and wavelength $\lambda_0 = 1.4823$ mm in the background medium. All 128 transducers are used for receiving the echo data. The dimension of the ROI is $13.5\lambda_0 \times 13.5\lambda_0$, and it is discretized with 60×60 cells. The focus was mainly on the inverse problem where the system of linear equations $\mathbf{X} \cdot \mathbf{y} = \mathbf{b}$, $\mathbf{X} \in \mathbb{C}^{4096 \times 3600}$ and $\mathbf{b} \in \mathbb{C}^{4096}$, is ill-posed.

A noise of 30 dB is added to the right side vector \mathbf{b} to mimic the realistic settings and test the regularization properties of the method. We first tested TTLS with fixed $k = 1000$ and we name it TTLS-fixed. Then, we used the proposed adaptive algorithm to obtain k , which we referred to as TTLS-adaptive. The values for k in each iteration of DBI are presented in Table 6.1. We can see that in the first few iterations of DBI

the value of the parameter is lower and TTLS is truncating more singular values. Latter in the iterations, the value increases because some errors have already been eliminated from the data and there is no need for removing more singular values. Reconstructed images of ROI after 10 iterations of DBI for both methods are presented in Figure 6.1. We measured the relative ℓ_2 norm error (RE- ℓ_2) as defined in the Equation (4.22). The relative error (RE) for the calculated scattered field $\boldsymbol{\psi}_s^{(i)}$ in the i^{th} iteration of the DBI is defined as:

$$\text{RE-sc. f.} = \frac{\|\boldsymbol{\psi}_s - \boldsymbol{\psi}_s^i\|_2}{\|\boldsymbol{\psi}_s\|_2}. \quad (6.6)$$

The standard approach is to use RE-sc. f. for termination of the DBI when it drops below a prescribed value, or it can be used to predict the divergence of an algorithm. Here, we used 10 iterations of the DBI and observed how this error behaved. It is shown in Figure 6.2 that relative error using TTLS-adaptive is less than error using TTLS-fixed. In order to prove whether the reconstruction detects tissue disorders, we observe the slice plots of the scattering function after 10 iterations of DBI, presented in Figure 6.3. We can see that for both horizontal slice plot at $y = 0$ mm and vertical slice plot at $x = 6.67$ mm, TTLS-adaptive is closer to the ground truth than TTLS-fixed.

6.2.2 Conclusions

We simulated the process of UT and tested TTLS method for the regularization of the inverse problem in each iteration of the DBI method where the truncation parameter is obtained using adaptive algorithm. It proved to give a good balance between minimizing the noise of 30 dB in the data and keeping received information as much as possible. The proposed adaptive algorithm provided lower relative error which resulted in better quality reconstruction image over fixing the value of the parameter for all iterations. These tests have shown that the efficiency of the regularization methods largely depends on the appropriate choice of truncation (regularization) parameter, which coincides with the conclusions from Chapter 5.

6.3 Regularized Total Least Squares

Since the TTLS solution can be sensitive to noise, additional regularization can be provided by incorporating constraint $\|\mathbf{Ly}\|_2 \leq \delta$. The variable δ comes from a knowledge of the underlying physical model and the regularization matrix \mathbf{L} is introduced in Chapter 3. This results in a method that combines features of TLS and Tikhonov regularization and is known as regularized total least squares (RTLS), described in [21] and [64]. Its formulation is given as:

$$\min \left\| (\mathbf{X}\mathbf{b}) - (\widehat{\mathbf{X}}\widehat{\mathbf{b}}) \right\|_F \quad \text{s.t.} \quad \|\mathbf{Ly}\|_2 \leq \delta \quad (6.7)$$

with the condition $\widehat{\mathbf{b}} \in \mathcal{R}(\widehat{\mathbf{X}})$ satisfied. One way to solve problem 6.7 is to find solution of the linear system:

$$(\mathbf{X}^T\mathbf{X} + \mu_1\mathbf{L}^T\mathbf{L} - \mu_2\mathbf{I})\mathbf{y} = \mathbf{X}^T\mathbf{b}. \quad (6.8)$$

The theorem which proves that a solution of (6.7) is also a solution of (6.8) can be found in [21]. The parameters μ_1 and μ_2 are given as:

$$\mu_1 = \eta(1 + \|\mathbf{y}\|_2^2) \quad \text{and} \quad \mu_2 = \frac{\|\mathbf{b} - \mathbf{Xy}\|_2^2}{1 + \|\mathbf{y}\|_2^2},$$

and the variable η is the Lagrange multiplier from

$$\mathcal{L}(\widehat{\mathbf{X}}, \mathbf{y}, \eta) = \|\mathbf{X} - \widehat{\mathbf{X}}\|_F^2 + \|\mathbf{b} - \widehat{\mathbf{b}}\|_2^2 + \eta(\|\mathbf{Ly}\|_2^2 - \delta^2).$$

In [25] is shown that the solution of 6.8 can be found by solving the eigenvalue problem:

$$\begin{pmatrix} \mathbf{X}^T\mathbf{X} + \mu_1\mathbf{L}^T\mathbf{L} - \mu_2\mathbf{I} & \mathbf{X}^T\mathbf{b} \\ \mathbf{b}^T\mathbf{X} & \mathbf{b}^T\mathbf{b} - \mu_2 - \mu_1\delta \end{pmatrix} \begin{pmatrix} \mathbf{y} \\ -1 \end{pmatrix} = \mu_2 \begin{pmatrix} \mathbf{y} \\ -1 \end{pmatrix} \quad (6.9)$$

The main difficulty of RTLS is that the unknown parameters μ_1 and μ_2 depend on the solution \mathbf{y} which is also unknown. Some ways of finding μ_1 and μ_2 are presented in [21] and [64] and we will write more on this in the next subsection.

In order for formulas to be more concise in the following sections, we introduce:

$$\mathbf{M}(\mu_1, \mu_2) = (\mathbf{X}^T\mathbf{X} + \mu_1\mathbf{L}^T\mathbf{L} - \mu_2\mathbf{I}), \quad (6.10)$$

and notation $\boldsymbol{\mu} = \begin{pmatrix} \mu_1 \\ \mu_2 \end{pmatrix}$ and $\mathbf{M}(\boldsymbol{\mu}) = \mathbf{M}(\mu_1, \mu_2)$.

6.4 RTLS-Newton

As described in previous section, the main problem of RTLS is that the unknown solution \mathbf{y} and the unknown parameters μ_1 and μ_2 are interdependent. One efficient way to solve this problem is presented by Lee et al. in [47]. Here, a short overview of their iterative method is presented. We name the method RTLS-Newton.

A well conditioned system of nonlinear equations

$$\begin{cases} \phi_1(\mu_1, \mu_2) = \frac{1}{\delta} - \frac{1}{\|\mathbf{L}\mathbf{y}\|_2} = 0 \\ \phi_2(\mu_1, \mu_2) = \mathbf{b}^T \mathbf{b} - \mu_2 - \mu_1 \|\mathbf{L}\mathbf{y}\|_2^2 - \mathbf{b}^T \mathbf{X}\mathbf{y} = 0 \end{cases} \Rightarrow \phi(\boldsymbol{\mu}) = \mathbf{0} \quad (6.11)$$

is derived. This system has a nonsingular Jacobian

$$J_\phi(\boldsymbol{\mu}) = \begin{pmatrix} \frac{\partial \phi_1}{\partial \mu_1} & \frac{\partial \phi_1}{\partial \mu_2} \\ \frac{\partial \phi_2}{\partial \mu_1} & \frac{\partial \phi_2}{\partial \mu_2} \end{pmatrix} = \begin{pmatrix} -2\lambda \mathbf{y}^T \mathbf{L}^T \mathbf{L} \frac{\partial \mathbf{y}}{\partial \mu_1} & -1 - \|\mathbf{y}\|_2^2 + 2\mu_1 \mathbf{y}^T \frac{\partial \mathbf{y}}{\partial \mu_1} \\ -\frac{\mathbf{y}^T \mathbf{L}^T \mathbf{L} \frac{\partial \mathbf{y}}{\partial \mu_1}}{\|\mathbf{L}\mathbf{y}\|_2^3} & \frac{\mathbf{y}^T \frac{\partial \mathbf{y}}{\partial \mu_1}}{\|\mathbf{L}\mathbf{y}\|_2^3} \end{pmatrix} \quad (6.12)$$

that can be computed inexpensively.

Then, a system 6.11 is solved iteratively using the Newton's method.

It generates a sequence $(\boldsymbol{\mu}^k)$ defined with:

$$J_\phi(\boldsymbol{\mu}^k) \cdot (\boldsymbol{\mu}^{k+1} - \boldsymbol{\mu}^k) = -\phi(\boldsymbol{\mu}^k). \quad (6.13)$$

The advantage of the method is fast convergence to a solution from any starting vector $\boldsymbol{\mu}^0$ that is close enough to a real solution.

The RTLS-Newton method is presented in Algorithm 2.

6.4.1 Numerical results

In order to test the advantages of using RTLS-Newton over TTLS for regularization within iterations of DBI, the following experiment is conducted. We simulated a system of 128 transducers positioned around the ROI as it is presented in Figure 2.1. Our ROI is a 20 mm \times 20 mm square and inside is the modified Shepp-Logan phantom which is a standard domain for testing in tomography. The sound wave is transmitted at the frequency of $f = 2$ MHz which is corresponding to the wavenumber $k_o = 8$ of the background medium. The ROI is discretized with 60 \times 60 cells, making the reconstructed

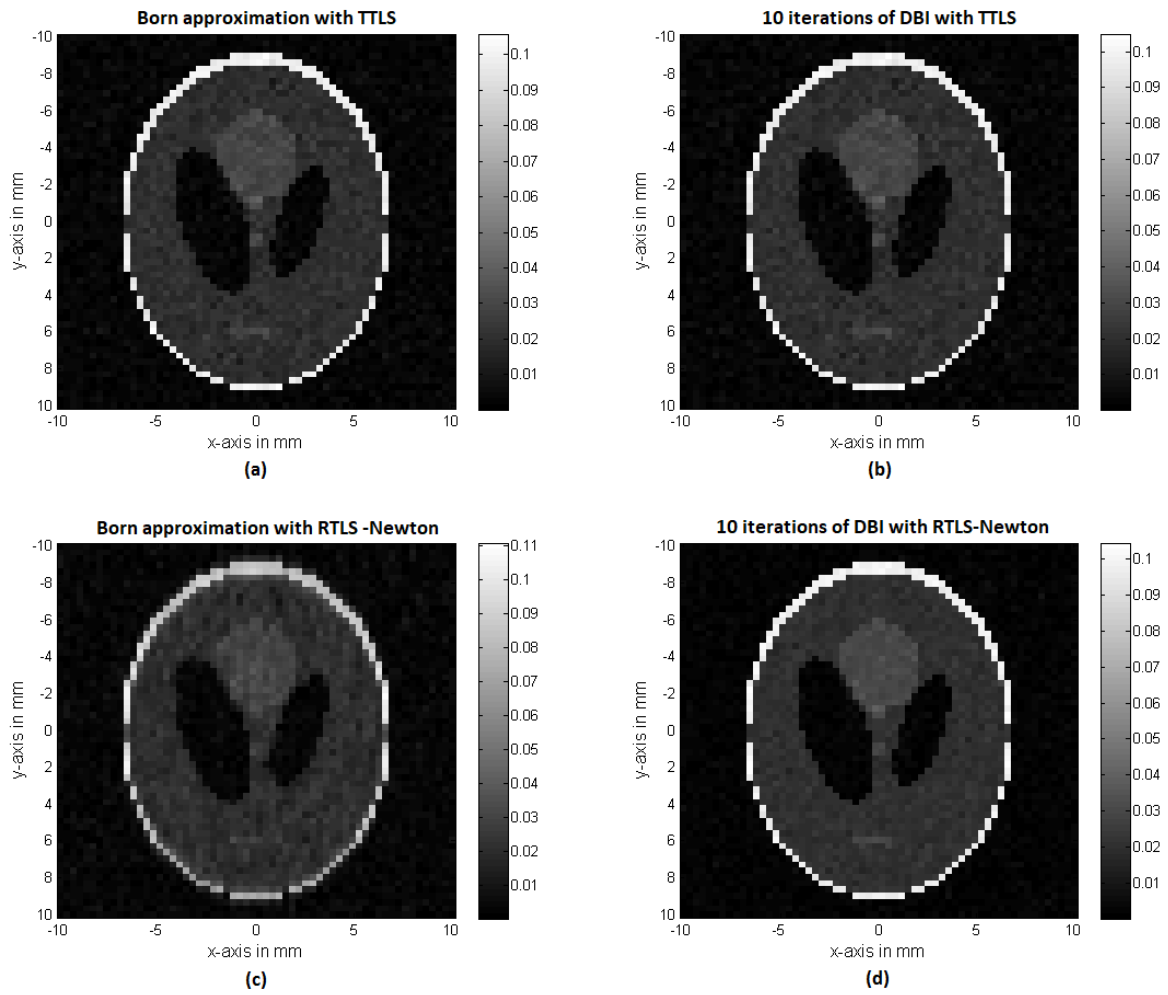


Figure 6.4: The reconstructed ROI in the **first setting** when a noise of SNR=30dB is added to the right side **b**. Reconstruction with Born approximation when (a) TTLS and (c) RTLS-Newton are used for regularization. The ROI after 10 iterations of the DBI using (b) **TTLS** and (d) **RTLS-Newton**. The frequency is $f = 2$ MHz.

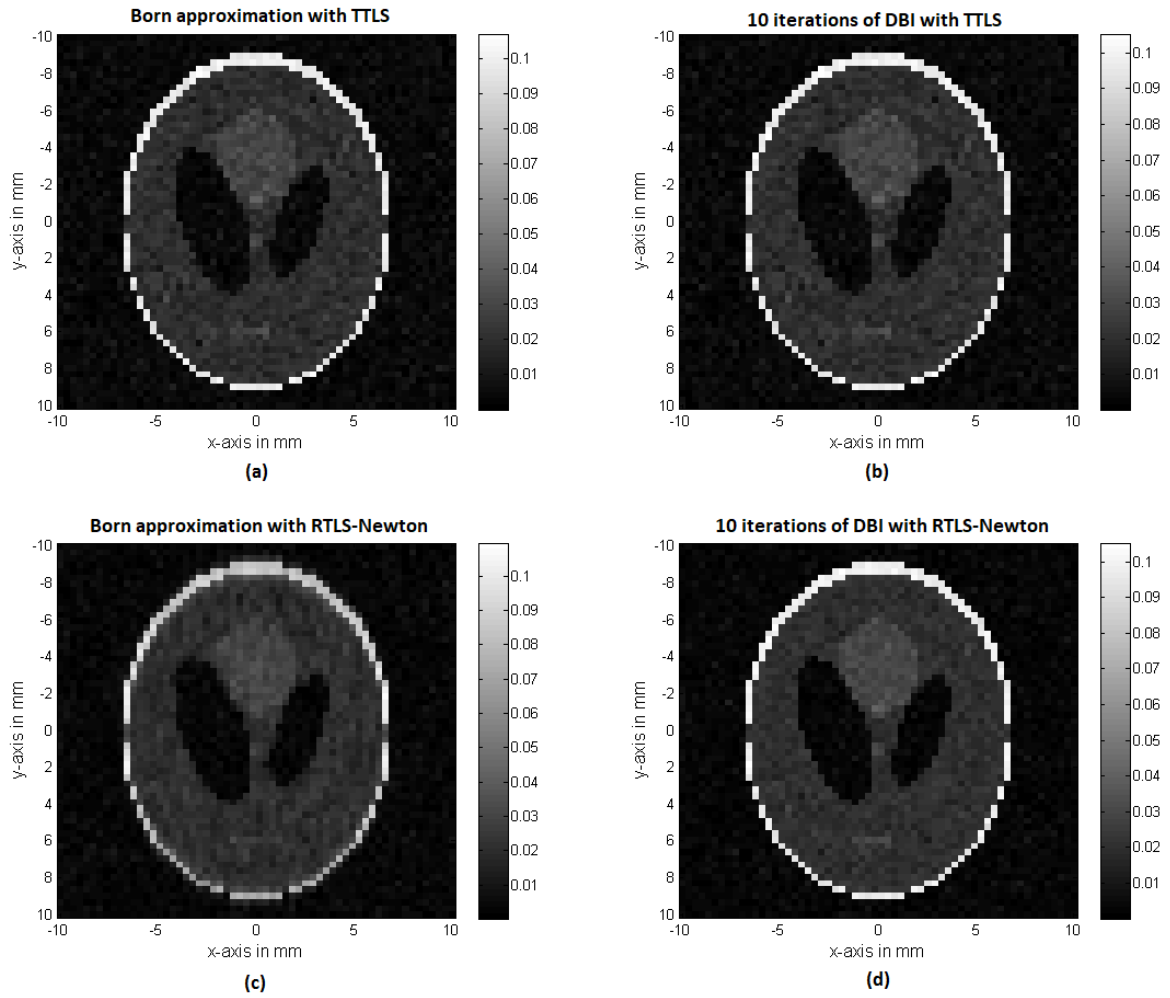


Figure 6.5: The **second setting** considers errors in \mathbf{X} and \mathbf{b} . The frequency is $f = 2$ MHz and the noise is SNR=30dB. Reconstruction of ROI using (a) Born approximation and (b) 10 iterations of DBI with **TTLS**. Reconstruction using (a) Born approximation and (b) 10 iterations of DBI with **RTLS-Newton**.

Algorithm 2 Algorithm for RTLS - Newton

- 1: Input \mathbf{X} , \mathbf{L} , \mathbf{b} , $\boldsymbol{\mu}^0$, tol
 - 2: $k = 0$
 - 3: Solve $\mathbf{M}(\boldsymbol{\mu}^0) \cdot \mathbf{y}^0 = \mathbf{X}^T \mathbf{b}$
 - 4: Set $\delta = \|\mathbf{L}\mathbf{y}^0\|_2$
 - 5: **While** RE \geq tol
 - Solve $\mathbf{M}(\boldsymbol{\mu}^k) \mathbf{y}_\mu^k = -\mathbf{L}^T \mathbf{L} \mathbf{y}^k$
 - Set the system $\phi(\boldsymbol{\mu}^k)$
 - Compute $J_\phi(\boldsymbol{\mu})$
 - Solve $J_\phi(\boldsymbol{\mu}^k) \cdot \Delta(\boldsymbol{\mu}^k) = -\phi(\boldsymbol{\mu}^k)$
 - Set $\boldsymbol{\mu}^{k+1} = \boldsymbol{\mu}^k + \alpha_k \Delta \boldsymbol{\mu}^k$
 - Solve $\mathbf{M}(\boldsymbol{\mu}^{k+1}) \mathbf{y}^{k+1} = \mathbf{X}^T \mathbf{b}$
 - RE = $\frac{\|\mathbf{y}^{k+1} - \mathbf{y}^k\|_2}{\|\mathbf{y}^k\|_2}$
 - $k = k + 1$
 - 6: return \mathbf{y}^k
-

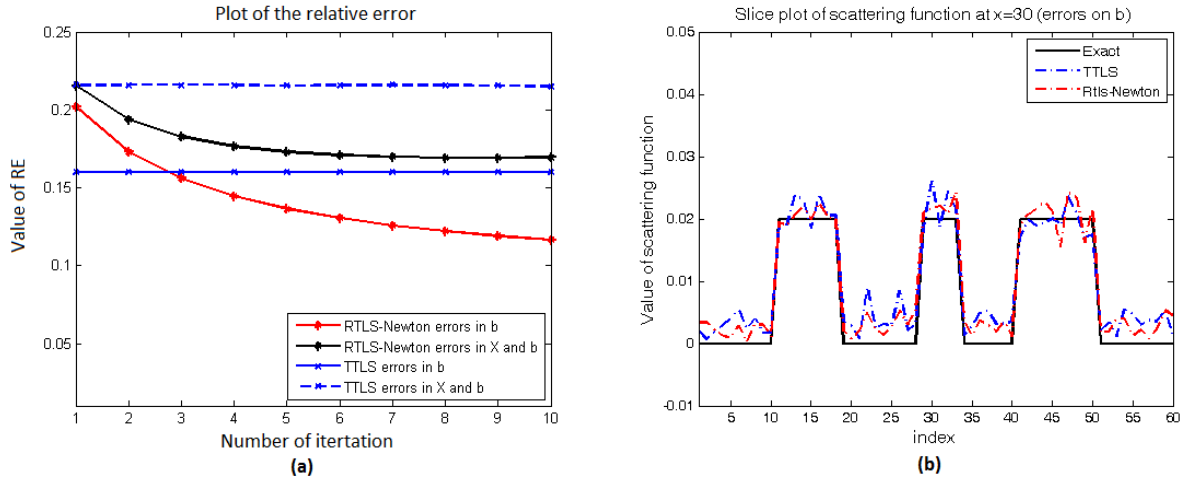


Figure 6.6: (a) Plots of relative errors for the scattering function during 10 iterations of the DBI in both settings with TTLs and RTLS-Newton. (b) Slice plots of the exact and reconstructed scattering functions in the first setting (noise in \mathbf{b}) after 10 iterations of the DBI with TTLs and RTLS-Newton

image of 3600 pixels. To overcome the problem of 3600 unknowns, we transmitted the wave from 32 transducers (one at the time) and collected the data from all 128 of them, making it 4096 equations leading to the overdetermined system $\mathbf{X}\mathbf{y} = \mathbf{b}$. We created two settings, in the first one the noise of SNR= 30 dB is added to the vector \mathbf{b} , and in the second one the errors are also in the matrix \mathbf{X} with the noise in \mathbf{b} . To numerically compare the quality of the reconstructed image, we calculated the relative error in ℓ_2 norm for the approximation of the scattering function $\hat{\mathbf{s}}$ as defined in the Equation (4.22). We first ran the Born approximation using both algorithms, TTLS and RTLS-Newton. We also measured the execution time for each of them. The algorithm RTLS-Newton was 10 times faster than the TTLS. We expected that, since the TTLS needs singular value decomposition which is time consuming. Using Born approximation as a initialization, we ran 10 iterations of the DBI. In Tab. 6.2 are presented relative errors for the scattering function in both settings after Born approximation and after 10 iterations of DBI.

Table 6.2: $RE - \ell_2$ for the reconstructed scattering function $\hat{\mathbf{s}}$ using Born approximation and after 10 iterations of the DBI in both settings.

Method	1 st setting (errors in \mathbf{b})		2 nd setting (errors in \mathbf{X} & \mathbf{b})	
	TTLS	RTLS-Newton	TTLS	RTLS-Newton
Born:	0.1630	0.2674	0.2201	0.2733
DBI (10 iter.)	0.1598	0.1166	0.2151	0.1694

Although the TTLS produces smaller error for Born, the RTLS-Newton decreases the error after 10 iterations of DBI for both settings. The reconstructed images of ROI are shown in Figure 6.4 and 6.5. Again, it is obvious that the regularization with RTLS-Newton produces better quality images. Figure 6.6 contains the plots of relative errors for scattering function for 10 iterations of DBI. We can see that RTLS-Newton is decreasing the error during iterations, while TTLS isn't making any significant improvement. The same figure also has the slice plots for the scattering function after 10 iterations of DBI for the first setting with aforementioned methods.

A comparison between RTLS-Newton and Tikhonov regularization in general form is presented in Section 6.6. The regularization parameter λ for the Tikhonov method is obtained with our adaptive algorithm (presented in Section 5.2).

6.5 Projection Based Regularized Total Least Squares

Another approach in solving the RTLS problem is the projection based regularized total least squares (PB-RTLS) presented in [46].

In order to speed up the execution time, PB-RTLS solves RTLS problem by projecting the matrices \mathbf{X} and \mathbf{L} onto the lower dimensional subspace \mathcal{S}_k spanned by the left orthogonal matrix $\mathbf{V}_k \in \mathbb{R}^{n \times k}$. Thus, all calculations are done with \mathbf{XV}_k and \mathbf{LV}_k , resulting in dimension reduction and faster computations. The problem being solved with PB-RTLS is formulated as:

$$\min_{\hat{\mathbf{x}}, \mathbf{y}^k} \left(\left\| \mathbf{b} - \hat{\mathbf{X}}\mathbf{V}_k\mathbf{y}^k \right\|_2^2 + \left\| \mathbf{XV}_k - \hat{\mathbf{X}}\mathbf{V}_k \right\|_F^2 \right) \quad \text{s.t.} \quad \|\mathbf{LV}_k\mathbf{y}^k\|_2 \leq \delta, \quad (6.14)$$

similarly as optimization problem in Equation (6.1) with added constraint and projected matrices.

To avoid the calculation of the SVD, the solution of (6.14) can be found using a formula similar to that in Equation (6.8) by solving the system:

$$\mathbf{V}_k^T \mathbf{M}(\mu_1, \mu_2) \mathbf{V}_k \mathbf{y}^k = \mathbf{V}_k^T \mathbf{X}^T \mathbf{b}. \quad (6.15)$$

We put $\boldsymbol{\mu} = \begin{pmatrix} \mu_1 \\ \mu_2 \end{pmatrix}$. To find $\boldsymbol{\mu}$, a well conditioned system of nonlinear equations $\phi_k(\boldsymbol{\mu})$ described as:

$$\phi_k(\boldsymbol{\mu}) = \begin{pmatrix} \frac{1}{\delta} - \frac{1}{\|\mathbf{LV}_k\mathbf{y}^k\|_2} \\ \mathbf{b}^T \mathbf{b} - \mu_2 - \mu_1 \|\mathbf{LV}_k\mathbf{y}^k\|_2^2 - \mathbf{b}^T \mathbf{XV}_k\mathbf{y}^k \end{pmatrix} = \mathbf{0} \quad (6.16)$$

with a nonsingular Jacobian

$$J_{\phi_k}(\boldsymbol{\mu}) = \begin{pmatrix} -2\mu_1(\mathbf{y}^k)^T (\mathbf{LV}_k)^T \mathbf{LV}_k \frac{\partial \mathbf{y}^k}{\partial \mu_1} & -1 - \|\mathbf{y}^k\|_2^2 + 2\mu_1(\mathbf{y}^k)^T \frac{\partial \mathbf{y}^k}{\partial \mu_1} \\ \frac{(\mathbf{y}^k)^T (\mathbf{LV}_k)^T \mathbf{LV}_k \frac{\partial \mathbf{y}^k}{\partial \mu_1}}{\|\mathbf{LV}_k\mathbf{y}^k\|_2^3} & \frac{(\mathbf{y}^k)^T \frac{\partial \mathbf{y}^k}{\partial \mu_1}}{\|\mathbf{LV}_k\mathbf{y}^k\|_2^3} \end{pmatrix} \quad (6.17)$$

was derived in [46], similar as for the RTLS-Newton. The first equation of the system (6.16) follows from the request $\|\mathbf{LV}_k\mathbf{y}^k\|_2 \leq \delta$, while the second one follows from the

Equation (6.15) with more complex derivation which details can be found in [46]. An iterative process is used to solve a nonlinear system in Equation (6.16) by first solving the system $J_{\phi_k}(\boldsymbol{\mu}^k) \cdot \Delta\boldsymbol{\mu}^k = -\phi_k(\boldsymbol{\mu}^k)$ and then updating $\boldsymbol{\mu}^{k+1} = \boldsymbol{\mu}^k + \Delta\boldsymbol{\mu}^k$. In this way, the RTLS problem is solved without using the singular value decomposition. In addition, an integrated parameter search inside the algorithm is provided so there is no need for the extra work in detection of truncation parameters as is necessary for TTLS.

The dimension k of the subspace \mathcal{S}_k expands dynamically by using a generalized Krylov subspace expansion. The expansion of \mathcal{S}_k to \mathcal{S}_{k+1} occurs when solution \mathbf{y}^k isn't converging. The matrix \mathbf{V}_k is then transformed to $\mathbf{V}_{k+1} = (\mathbf{V}_k, \mathbf{v}_{k+1})$ by adding the column

$$\mathbf{v}_{k+1} = \alpha_k(\mathbf{I} - \mathbf{V}_k\mathbf{V}_k^T)\mathbf{r}_k,$$

where $\mathbf{r}_k = \mathbf{X}^T\mathbf{b} - \mathbf{M}(\mu_1, \mu_2)\mathbf{V}_k\mathbf{y}^k$ and α_k is a scalar such that $\|\mathbf{v}_{k+1}\|_2 = 1$. The final solution of the problem is $\mathbf{y} = \mathbf{V}_k\mathbf{y}^k$ and the whole pseudocode of PB-RTLS is presented in Algorithm 3. We note that in our tests, presented in Section 6.5.1, the matrix form of the first order derivative operator, defined in Equation 3.15, is used for matrix \mathbf{L} .

6.5.1 Numerical Results

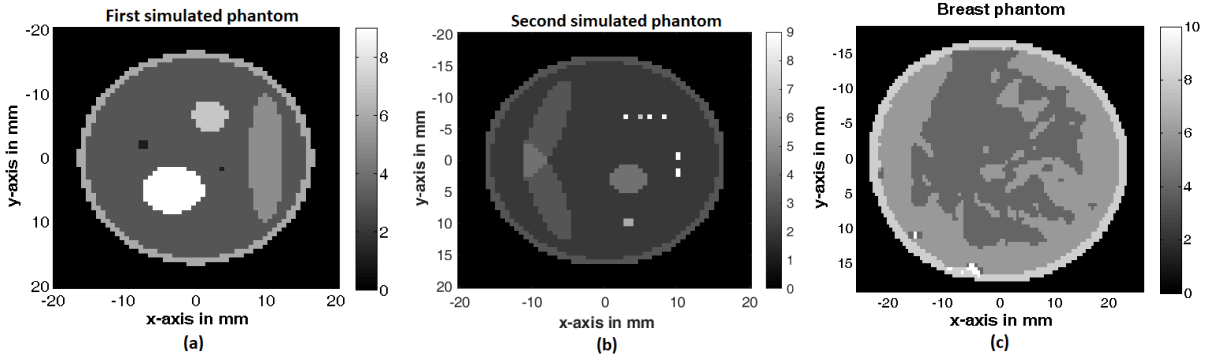


Figure 6.7: Exact (a) first simulated, (b) second simulated and (c) breast phantom used in our simulations of UT. The distribution of speed of sound is shown as percentage increase over background medium.

We simulate an environment of 128 transducers surrounding the region of interest (ROI) as shown in Figure 2.1. The ultrasound wave is excited at frequency of 2 MHz, one at a time, and all 128 transducers were used as receivers. We created three different

Algorithm 3 Algorithm for PB-RTLS

- 1: Input \mathbf{X} , \mathbf{L} , \mathbf{b} , $\boldsymbol{\mu}^1$, tol
 - 2: $k = 1$
 - 3: Solve $\mathbf{M}(\boldsymbol{\mu}^1) \cdot \mathbf{v}_1 = \mathbf{X}^T \mathbf{b}$
 - 4: Set $\mathbf{V}_1 = [\mathbf{v}_1]$
 - 5: Solve $(\mathbf{V}_1^T \mathbf{M}(\boldsymbol{\mu}^1) \mathbf{V}_1) \mathbf{y}^1 = \mathbf{V}_1^T (\mathbf{X}^T \mathbf{b})$
 - 6: Set $\delta = \|\mathbf{L} \mathbf{V}_1 \mathbf{y}^1\|_2$
 - 7: **While** ERR \geq tol
 - 8: Set the system $\phi_k(\boldsymbol{\mu}^k)$
 - 9: Compute $J_{\phi_k}(\boldsymbol{\mu}^k)$
 - 10: Solve $J_{\phi_k}(\boldsymbol{\mu}^k) \cdot \Delta \boldsymbol{\mu}^k = -\phi_k(\boldsymbol{\mu}^k)$
 - 11: Set $\boldsymbol{\mu}^{k+1} = \boldsymbol{\mu}^k + \Delta \boldsymbol{\mu}^k$
 - 12: Set $\mathbf{r}^k = \mathbf{M}(\boldsymbol{\mu}^k) \mathbf{V}_k \mathbf{y}^k - \mathbf{X}^T \mathbf{b}$
 - 13: Set $\mathbf{v}_{k+1} = \mathbf{r}^k - \mathbf{V}_k \mathbf{V}_k^T \mathbf{r}^k$, $\mathbf{v}_{k+1} = \frac{\mathbf{v}_{k+1}}{\|\mathbf{v}_{k+1}\|_2}$
 - 14: Set $\mathbf{V}_{k+1} = (\mathbf{V}_k \mathbf{v}_{k+1})$
 - 15: Solve $\mathbf{V}_{k+1}^T \mathbf{M}(\boldsymbol{\mu}^{k+1}) \mathbf{V}_{k+1} \mathbf{y}^{k+1} = \mathbf{V}_{k+1}^T \mathbf{X}^T \mathbf{b}$
 - 16: ERR = $\frac{\|\mathbf{V}_{k+1} \mathbf{y}^{k+1} - \mathbf{V}_k \mathbf{y}^k\|_2}{\|\mathbf{V}_k \mathbf{y}^k\|_2}$
 - 17: $k = k + 1$
 - 18: Return $\mathbf{y} = \mathbf{V}_k \mathbf{y}^k$
-

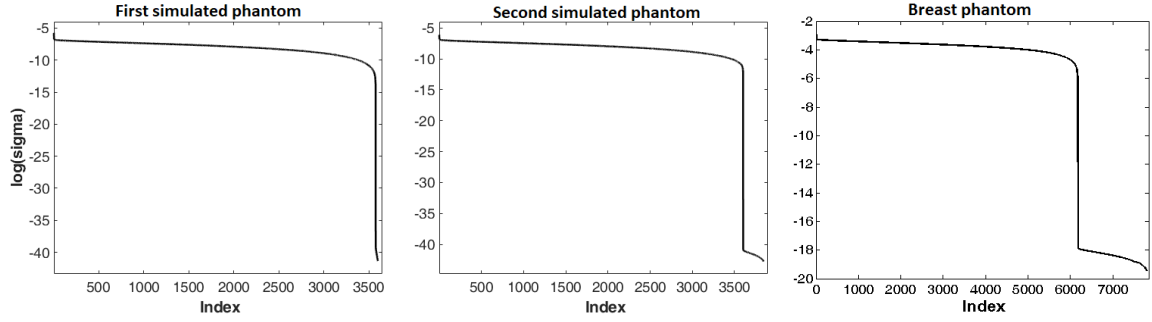


Figure 6.8: Plots for SVD of operator matrix in Born approximation for first simulated (left), second simulated (middle) and breast phantom (right).

settings for our tests with added Gaussian noise of 20, 25 and 30 dB on ψ_{s_m} respectively.

The area of the ROI was discretized into $C \times D$ pixels and three different phantoms (first simulated, second simulated and breast phantom) were tested as scattering object. First simulated phantom is shown in Figure 6.7 (a) with dimensions $40 \text{ mm} \times 40 \text{ mm}$ ($53.33\lambda_0 \times 53.33\lambda_0$) and 60×60 pixels. It consists of a cylinder which has a contrast of 3% and is surrounded with a ring that has a contrast of 6%. Inside it are three ovals with different shapes and contrast percentages (5%, 7% and 9%). We would like to note that all of these contrast percentage are the percentage increase over the background medium. The second simulated phantom contains small scattering objects, visible in Figure 6.7 (b). The smallest objects have contrast of 9%, while other two objects have contrast increase of 4% and 6%. In addition, there are two intersecting ovals with contrast of 3%. The phantom is discretized with 62×62 pixels. However, it is the same size as the first simulated phantom. For the simulation to be more realistic, we have decided to use a breast phantom obtained from the database described in [51], shown in Figure 6.7 (c). The dimensions are $37.5 \text{ mm} \times 52 \text{ mm}$ ($50\lambda_0 \times 69.33\lambda_0$) and 75×104 pixels. With the aim of providing more data than the number of unknown pixels for the simulated phantoms, we have used 32 transducers, one at a time, as transmitters of total 128 transducers. However, to maintain the overdetermined system, we have used 64 transmitters in a case of breast phantom, since it has larger number of pixels. We are able to process these amount of data since PB-RTLS is not time consuming and TTLS only requires calculation of SVD.

We used Born approximation to find the first estimate of the scattering function and

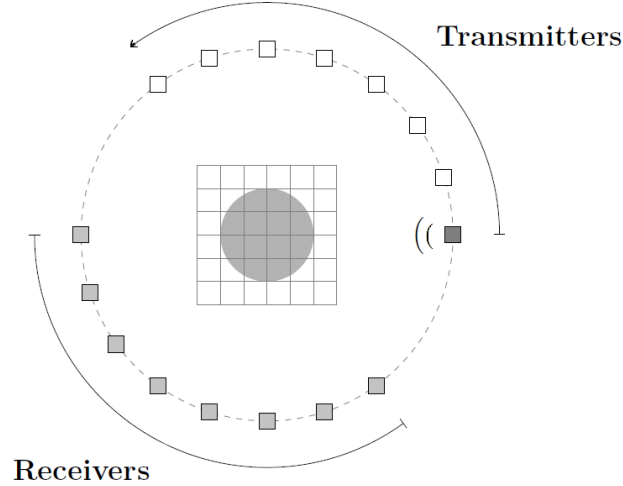


Figure 6.9: Position of transmitters and receivers in the limited aperture setting. The ultrasound wave is excited from transmitters counterclockwise, one at a time, and the echo is received with the receivers. For the first (second) simulated phantom, we have used 60 (62) transmitters on the one side and 60 (62) receivers on the other side. For the breast phantom, 88 transmitters and 89 receivers were used.

then we had our DBI method ran for 10 iterations. The necessity for the regularization is visible in the SVD plots (Figure 6.8) since the larger singular values are significantly bigger than the smallest one. We used these plots to determine the truncation parameter k in TTLS for both simulated and breast phantoms. The values were 3510, 3200 and 6000 respectively. All simulations and test were preformed in MATLAB (The Mathworks Inc., Natick, MA, USA) with a four core processor Intel I7 with 32 GB of RAM.

In addition to the full aperture setting, where all 128 transducers were used as receivers, we created a limited aperture setting, presented in Figure 6.9, where the receivers are located on one side of the scattering object and transmitters are on the other side. The transmitters excited the wave counterclockwise, one at a time, and all receivers received the echo simultaneously. The positions of the 128 transducers didn't change from the previous full aperture setting. We would like to emphasize that the size of first simulated phantom is 60×60 pixels and second simulated phantom is 62×62 . We used 60 transmitters on the one side and 60 receivers on the other side for the first simulated phantom. For the second phantom, we used 62 transmitters and 62 receivers. Since the breast phantom is composed of more pixels (75×104), we used 88 of transducers as a

transmitters and 89 as a receivers. For the first and second simulated phantoms we don't have overlap between transmitters and receivers. However, for the breast phantom we have overlap in order to ensure an overdetermined system. Tests for all phantoms were performed with 30 dB noise.

Table 6.3: RE- ℓ_2 for the reconstructed scattering function using Born approximation in Full and Limited aperture setting.

Scattering object	Setting	SNR	TTLS	PB-RTLS
First simulated phantom	Full aperture	30 dB	0.7279	0.2038
		25 dB	0.8468	0.2117
		20 dB	0.9185	0.3078
	Limited aperture	30 dB	0.7313	0.2132
Second simulated phantom	Full aperture	30 dB	0.4223	0.1903
		25 dB	0.5461	0.1996
		20 dB	0.7539	0.3176
	Limited aperture	30 dB	0.4524	0.2083
Breast phantom	Full aperture	30 dB	1.3697	0.2098
		25 dB	1.7353	0.2269
		20 dB	2.0638	0.3104
	Limited aperture	30 dB	1.9967	0.2213

6.5.2 Reconstruction with Born approximation and DBI

We compared the performance of TTLS and PB-RTLS method for the Born approximation and DBI in the full aperture setting. In order to measure numerically the quality of reconstruction, we calculated the relative error (RE- ℓ_2) for the scattering function as defined in the Equation (4.22).

Regularization with PB-RTLS provided smaller relative error for the Born approximation than TTLS in all tested cases as seen in Table 6.3. In addition, PB-RTLS maintained values of RE- ℓ_2 lower than 0.32 when SNR decreased from 30 dB to 20 dB, while TTLS was worse in all cases. The plots of RE- ℓ_2 for DBI of the simulated phantom, Figure 6.10 (a), demonstrates that PB-RTLS gives much smaller relative error than TTLS for all three tested values of SNR. In addition, only 7 iterations of DBI were required for the

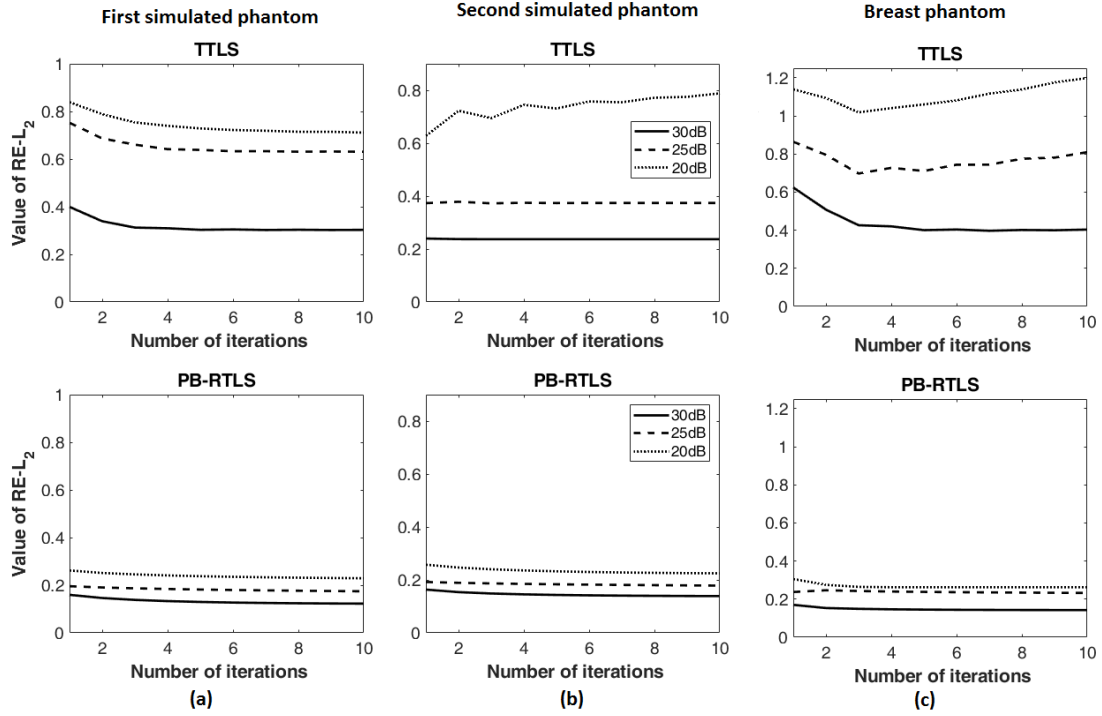


Figure 6.10: Plots of the relative error $RE-\ell_2$ during the 10 iterations of the DBI method for (a) first simulated, (b) second simulated and (c) breast phantom in the full aperture setting.

relative error to be below 0.125 when SNR is 30 dB. For the second simulated phantom, PB-RTLS also provided lower $RE-\ell_2$ than TTLS. Plots of $RE-\ell_2$ for the breast phantom, have similar behavior, shown in Figure 6.10 (c) except TTLS diverged after 3 iterations when SNR is 25 and 20 dB, and is almost constant after 5 iterations when SNR is 30 dB. Reconstructed images after 10 iterations of DBI for all phantoms with SNR=30 dB are shown in Figure 6.11, where it is visible that PB-RTLS provided better regularization, resulting in a better quality image that has higher resolution and more visible edges than the results from TTLS.

Another criteria used to measure the quality of reconstruction is the contrast percentage slice plot of the reconstructed image in the last iteration of DBI. Slice plots for all phantoms with 30, 25 and 20 dB SNR are shown in Figure 6.12. The y-axis represents the value of the scattering function, which holds information about contrast level, and x-axis represents the dimension of the ROI. We took horizontal line, fixed at $y=-1.33$ mm for the first simulated phantom, at $y=2.58$ mm for the second simulated phantom and at $y=11.25$ mm for the breast phantom. The contrast percentage slice plots in Figure 6.12

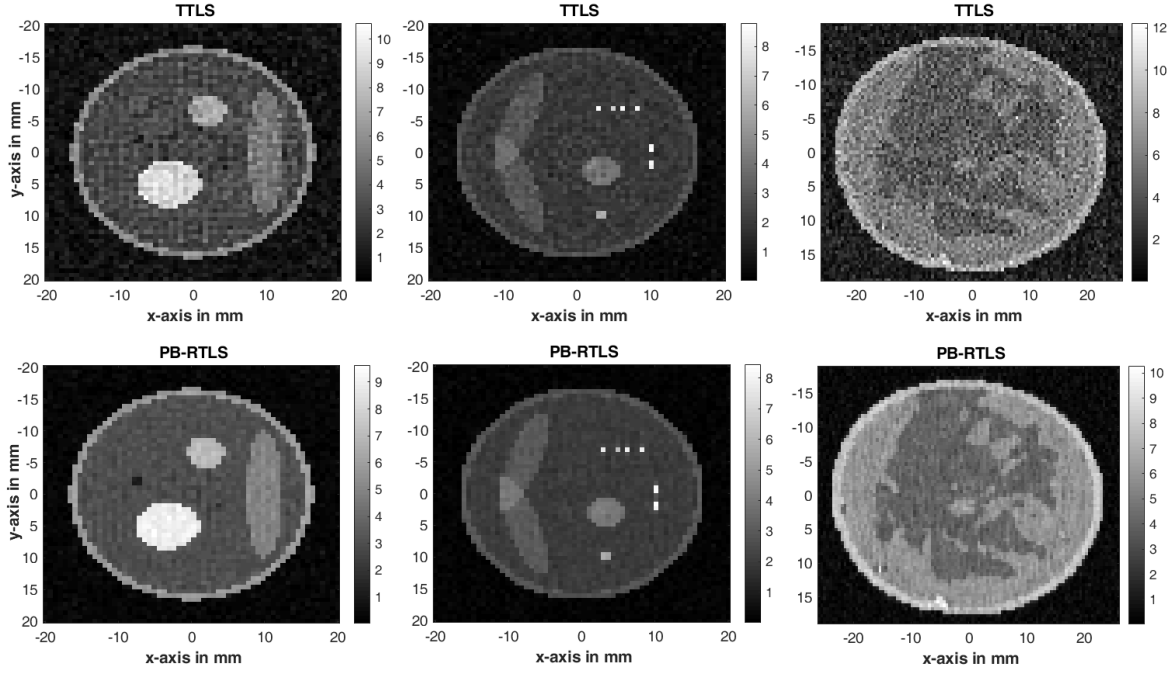


Figure 6.11: Reconstructions of first simulated (top), second simulated (middle) and breast phantom (bottom) after 10 iterations of DBI using **TTLS** (top row) and **PB-RTLS** (bottom row) in the **Full aperture** setting. The frequency is $f = 2$ MHz with a 30 dB SNR.

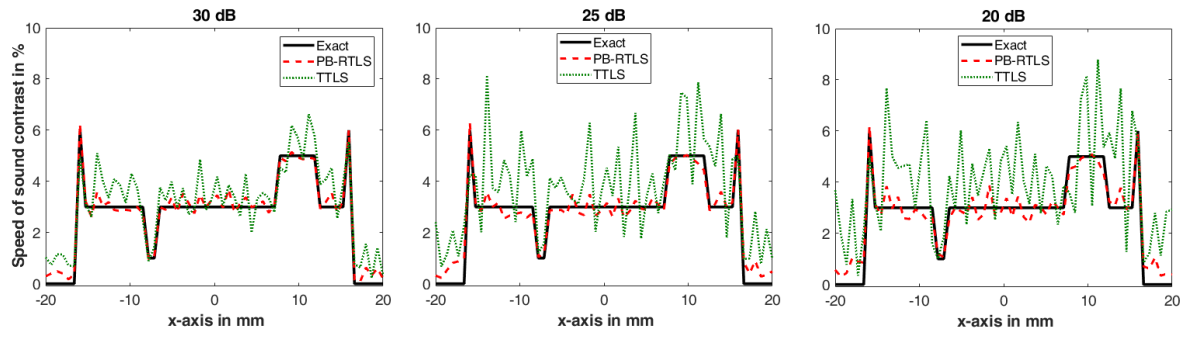
show that the PB-RTLS has values that are much more closer to the exact image and they are far less affected by noise for the lower SNR than the TTLS.

We also performed tests for the limited aperture setting with SNR equal to 30 dB for all three phantoms. Values for the truncation parameter k were 3395 for first simulated, 3660 for second simulated and 6620 for breast phantom. $RE-\ell_2$ values for Born approximation, presented in Table 6.3, and plots of $RE-\ell_2$, presented in Figure 6.13, show that PB-RTLS produces lower relative error than TTLS for all tested cases. Reconstructed images after 10 iterations of DBI for all phantoms are shown in Figure 6.14, and same as in the full aperture setting shown in Figure 6.11, PB-RTLS provided better regularization than TTLS which resulted in high quality images with clear composition.

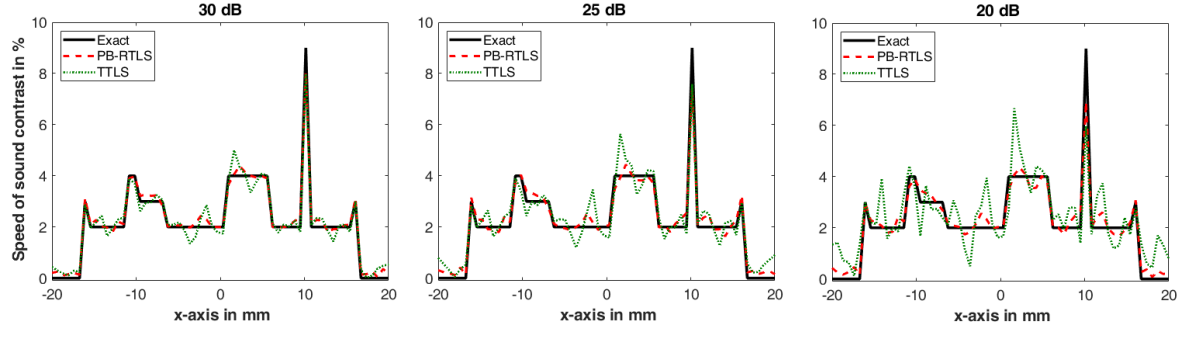
In addition to comparing the reconstruction accuracy, we also compared the execution time. The PB-RTLS method was six times faster in both tested cases (simulated and breast phantom) than TTLS. This was expected since PB-RTLS is solving the problem on lower dimensional subspace and is avoiding the calculation of SVD.

These results confirmed the privilege of using our proposed method (PB-RTLS) over

First simulated phantom



Second simulated phantom



Breast phantom

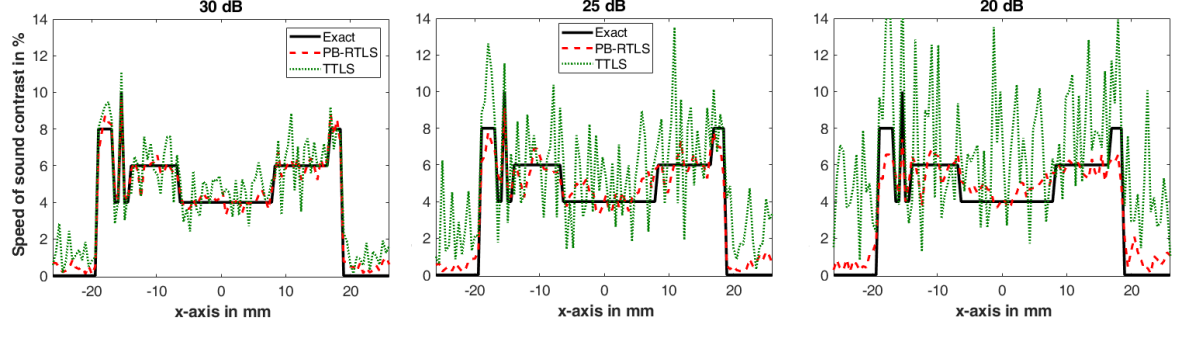


Figure 6.12: Slice plots in the **Full aperture** setting for first simulated phantom at $y=-1.33$ mm (top), second simulated phantom at $y=2.58$ mm (middle) and breast phantom at $y=11.25$ mm (bottom).

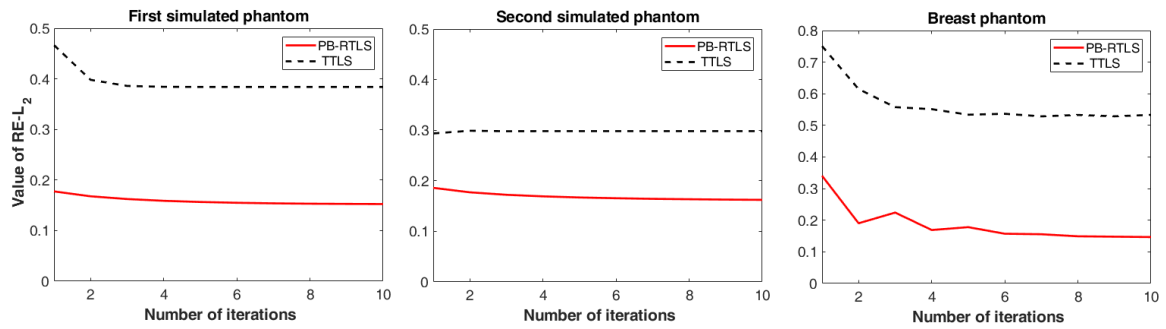


Figure 6.13: Plots of the relative error $RE\text{-}l_2$ during the 10 iterations of the DBI method in the **Limited aperture** setting with 30 dB noise for first simulated (left), second simulated (middle) and breast phantom (right).

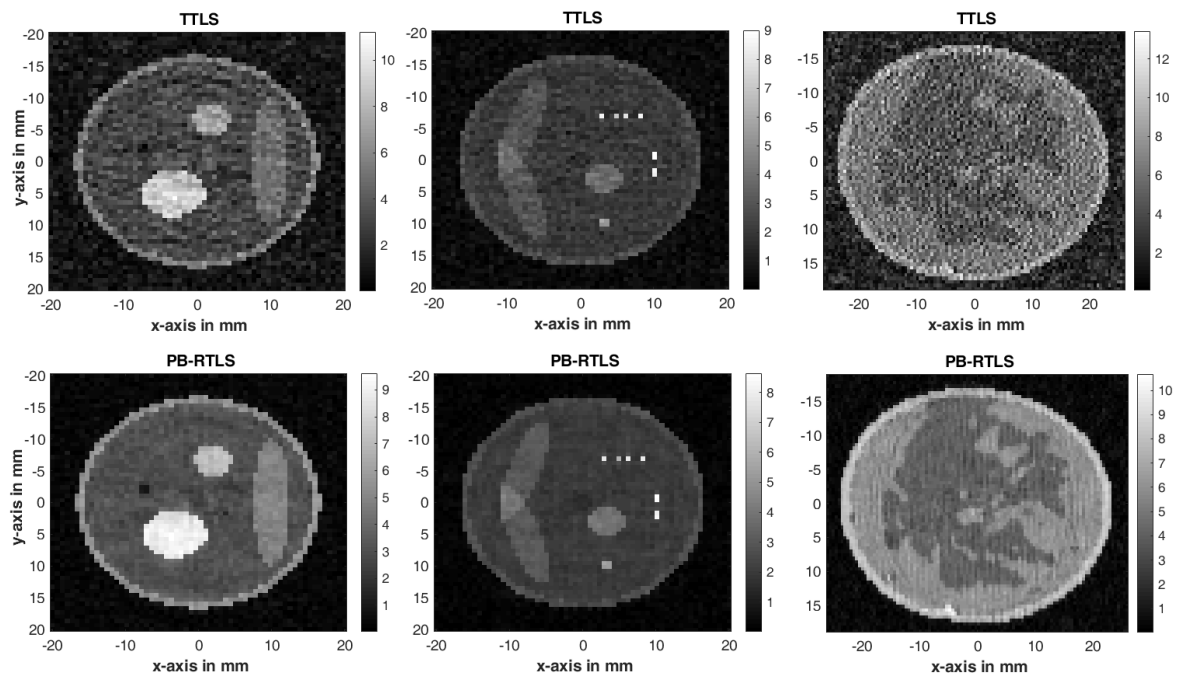


Figure 6.14: Reconstructions of first simulated (left), second simulated (middle) and breast phantom (right) after 10 iterations of DBI using **TTLS** (top row) and **PB-RTLS** (bottom row) in the **Limited aperture** setting. The frequency is $f = 2$ MHz with a 30 dB SNR.

TTLS in solving the inverse problem with either Born approximation or DBI. Although the regularization properties of the TTLS method have been reported in several papers [18], [50], we have proved that using PB-RTLS produced a higher quality image than TTLS. Another drawback of the TTLS is on the choice of the k parameter. There are some methods that can provide a regularization parameter such as GCV [22], [42], Discrepancy principle [34] or L-curve [35], [42], but they add more computational time. However, PB-RTLS is avoiding the calculation of this truncation parameter, and instead has two parameters μ_1 and μ_2 that only need arbitrary starting values. Then, during the iterations, PB-RTLS is correcting these values based on the problem being solved making the DBI method to converge as seen in previous section.

Since in our simulation we used noisy data (20, 25 and 30 dB), the tested PB-RTLS method, which employs discrete version of the first order derivative operator, obtained the additional smoothness of the solution. All of the tested phantoms had parts with constant velocity values, so an improvement in the reconstruction of contrast profiles was expected. In this way, in each iteration the relative error was decreased, resulting in the convergence of the DBI method that results in a high quality reconstructed ultrasound image. This is clearly shown, as we mentioned earlier, in plots for the RE- ℓ_2 (Figure 6.10) error and final reconstructed images (Figure 6.11) respectively. In addition, from Figure 6.10, it is visible that PB-RTLS ensures smaller relative error for all tested values of SNR, unlike TTLS. That can be attributed to the influence of the matrix \mathbf{L} that has been used in PB-RTLS. The same influence is also seen in the slice plots (Figure 6.12). We used first order derivative operator which works as a smoother of the solution. It is obvious that the values of the TTLS are much noisier than our proposed method. More precisely, on Figure 6.12 for 30 dB (left) is visible that PB-RTLS well reconstructed for each local minimum and local maximum values, while TTLS was 1 and 2% off expected. In addition, when noise of 20 or 25 dB is used, the quality of reconstructed images with TTLS deteriorated. For the limited aperture setting when 30 dB SNR is used, PB-RTLS also provided better reconstruction of all phantoms than TTLS. In addition, PB-RTLS is also suited for solving linear systems where the matrix \mathbf{X} is subject to errors, so this desirable characteristic of TTLS is not lost when it is replaced by PB-RTLS.

To the best of our knowledge, the only reported use of TTLS in UT was on simulated

phantom in [9], [10], [50] and [76]. However, in our performed tests TTLS diverged in the case of second simulated phantom for low SNR (20 dB). Moreover, we tested the performance of TTLS on a more realistic domain (breast phantom [51]) and TTLS diverged after 3 iterations when SNR is 20 and 25 dB (Figure 6.10 (c)) because medium is highly scattering. This gives us indication that it will not be suited for more complex mediums. Regularization with PB-RTLS proven to be better because it implicitly combined the effects of both TTLS and Tikhonov.

We would like to note that in Section 6.4 we have proved that another regularization method (RTLS-Newton) yields a better reconstructed image than TTLS. The RTLS-Newton method is implemented as an eigenvalue problem (avoiding the explicit calculation of the SVD) and is using Newton method to find regularization parameters. However, implementation of RTLS in this section is different. The proposed method PB-RTLS projects the problem onto lower dimensional subspace, making the calculations easier which results on less execution time. In addition, the effects of the regularizations are different because of this dimension reduction.

When we described the DBI method, we mentioned that the iterations should stop when the relative error of the calculated scattered field is below a prescribed threshold. However, for our simulation we ran 10 iterations of DBI. The reason for this is the threshold is only an arbitrary number, if we set it to high, iterations will stop much earlier and there would be no way of telling how well the reconstruction algorithm can be. It is noticeable that we could save on execution time by terminating the iterations earlier. As we can see in Figure 6.10, PB-RTLS has approximately reached lower value for $RE-\ell_2$ after 4 iterations for most settings and the decrease after that wasn't significant.

6.5.3 Conclusions

To conclude, the main advantages of the proposed PB-RTLS method over TTLS are:

1. Employing regularization matrix \mathbf{L} that impose additional smoothness on the solution, proving to be useful when lower SNR level is introduced, such as 20 and 25 dB.
2. Integrated search for regularization parameters μ_1 and μ_2 inside the algorithm so no

other method is used for parameter choice. In addition, μ_1 is controlling the matrix \mathbf{L} to avoid oversmoothing the solution.

3. Algorithm has at least six times less computational time since the calculation of SVD is avoided and the problem is projected onto lower dimensional subspace.

6.6 Comparison between Adaptive algorithm, RTLS-Newton and PB-RTLS

Through this dissertation, three methods have shown to be effective for regularization of the inverse problem in UT. These methods are: Tikhonov regularization in general form where the regularization parameter λ is obtained using our adaptive method (presented in Section 5.2), RTLS-Newton (presented in Section 6.4) and PB-RTLS (presented in Section 6.5).

In this section, we compare aforementioned methods with each other and analyze their advantages and disadvantages. A common feature of all three methods is the usage of regularization matrix \mathbf{L} , which has proved to be useful in Sections 4.4 and 4.5. The difference between methods is that RTLS-Newton and PB-RTLS assume the errors both in matrix operator \mathbf{X} and measured vector \mathbf{b} , while Tikhonov regularization considers only errors in \mathbf{b} . In addition, it is expected that PB-RTLS and RTLS-Newton are much faster since they avoid calculation of SVD or GSVD which can be time consuming.

Table 6.4: RE- ℓ_2 for Born approximation and after 10 iterations of DBI.

SNR	PB-RTLS	RTLS-Newton	Tikh. gen. Adaptive
	Born \rightarrow DBI	Born \rightarrow DBI	Born \rightarrow DBI
30 dB	0.2038 \rightarrow 0.1226	0.2491 \rightarrow 0.1359	0.2065 \rightarrow 0.1219
25 dB	0.2117 \rightarrow 0.1743	0.3079 \rightarrow 0.1999	0.2397 \rightarrow 0.1627
20 dB	0.3078 \rightarrow 0.2290	0.3380 \rightarrow 0.2421	0.2733 \rightarrow 0.2189

To test aforementioned methods, we used the same simulation of UT in full aperture setting as presented in Section 6.5.1. The goal was to reconstruct the first simulated phantom, shown in Figure 6.7 (a), using the DBI method in three different cases. Each

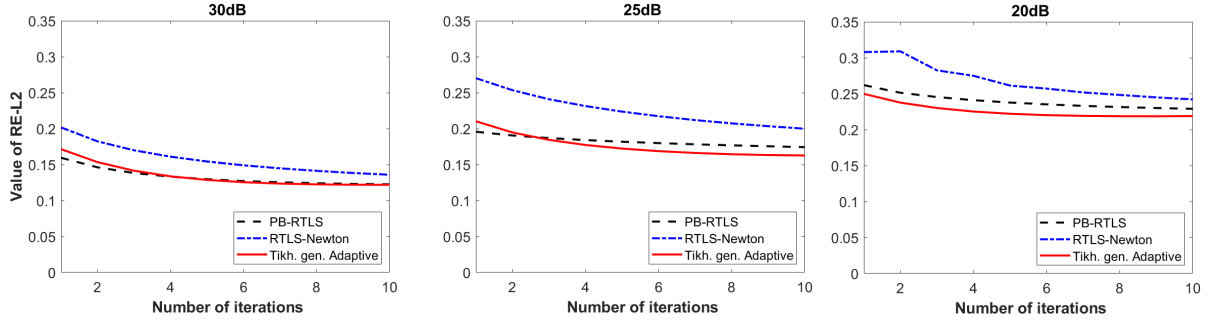


Figure 6.15: Plots of the relative error $RE-\ell_2$ for PB-RTLS, RTLS-Newton and Tikhonov general Adaptive during 10 iterations of the DBI method with 30 dB (left), 25 dB (middle) and 20 dB noise (right).

case had a different noise level: 20dB, 25dB and 30dB.

The slowest method was Tikhonov in general form since it required calculation of GSVD of matrix pair (\mathbf{X}, \mathbf{L}) . The RTLS-Newton was faster as expected. The fastest one was PB-RTLS because, not only that GSVD calculation was avoided, but the problem was projected onto lower dimensional subspace.

Values of the relative error $RE-\ell_2$ for the reconstructed scattering function in Born approximation and after 10 iterations of DBI are presented in Table 6.4. These values show that our adaptive method produces the lowest relative error. This is also confirmed with the plots of $RE-\ell_2$, presented in Figure 6.15. It is visible that our adaptive method produces the lowest relative error for 20 and 25 dB, while for 30 dB it is similar to PB-RTLS.

Figure 6.16 shows horizontal slice plots of the reconstructed phantom at $y = 2$ mm for three different cases: 30 dB, 25 dB and 20 dB noise. The highlighted segment of the images for 25 and 20 dB show that the part of the phantom with the highest value of the change in velocity is best reconstructed using our adaptive algorithm.

The advantage of PB-RTLS is that it accounts for the errors in matrix \mathbf{X} . However, our adaptive algorithm utilize the features of DBI method (mainly the discrepancy between calculated and measured scattered field) to decrease the influence of the noise.

PB-RTLS provides accuracy with low execution time, while for more noisier data (SNR equal to 20 or 25 dB), Tikhonov regularization combined with our adaptive algorithm is more accurate.

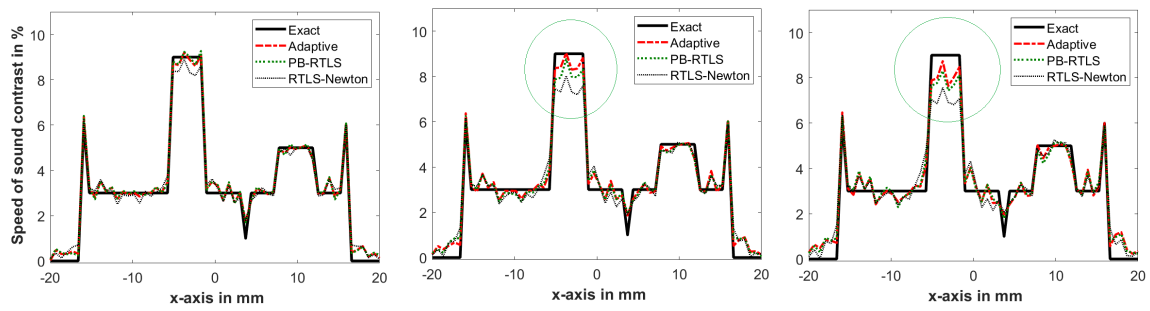


Figure 6.16: Slice plots of the reconstructed phantom after 10 iterations of DBI for three different cases: 30 dB (left), 25 dB (middle) and 20 dB noise (right).

Chapter 7

Conclusions

7.1 Summary and conclusions

Ultrasound tomography (UT) is a medical imaging modality which can be used for the detection of malignant tissue in the human breast. Compared to other imaging techniques, such as X-ray mammography, CT and MRI, it is relatively low cost and does not infiltrate healthy tissue. The ultrasound wave propagation can be modeled using Helmholtz equation, that is, its Lippmann-Schwinger integral representation when Sommerfeld radiation condition is satisfied. However, this problem is nonlinear since it requires knowledge of both scattering function and total field throughout the region of interest. Hence, it can not be solved exactly.

In this dissertation we simulated the problem of UT and solved it numerically using the distorted Born iterative (DBI) method, as described in Chapter 2. The Born approximation was used as initialization for DBI. Since an ill-posed inverse problem needs to be solved within each iteration of DBI, main focus of this dissertation was on its regularization.

Direct regularization methods, presented in Chapter 4, are based on truncating or damping smaller (generalized) singular values. We created a simulation of UT and solved the inverse problem using truncated (G)SVD and damped (G)SVD. A comparison between these SVD forms and GSVD forms of methods showed the benefits of using first order derivative operator \mathbf{L} , which is a part of TGSVD and DGSVD, in reconstruction of scattering function for UT. This can be attributed to the smoothing property of matrix

L.

An appropriate regularization parameter is necessary for direct regularization methods to be efficient. Existing algorithms for parameter search (GCV and L-curve) are proven to be ineffective when utilized within DBI. That is why in Chapter 5 we developed our adaptive algorithm based on signal loss and noise error. It requires only an overestimate of the norm of noise in measured data. Then this estimation is decreased within iterations of DBI according to discrepancy between measured and calculated data.

These three algorithms were utilized for Tikhonov regularization inside the DBI method and tested for simulations on two different phantoms with 20 and 30 dB noise. Two different settings were created. First one was full aperture setting, where all transducers were receiving the echo. The second one was limited aperture settings where the echo was received with certain number of transducers placed on one side of imaging object.

Our proposed algorithm provided the lowest relative error of reconstructed scattering function for all tested cases after 10 iterations of DBI. The reason for this was that our algorithm determined an adequate parameter λ inside each iteration of DBI, while the parameters obtained with GCV and L-curve were either too large or too small respectively. This resulted in higher quality reconstructed images when our algorithm was employed.

Another approach in regularizing the inverse problem is truncated total least squares (TTLS) method, showed in Chapter 6, which assumes errors both in operator matrix \mathbf{X} and measured vector \mathbf{b} . Since matrix \mathbf{X} in ill-posed inverse problem is composed of approximations for the total field and inhomogeneous Green's functions, the TTLS method seems like a logical choice for the regularization. However, TTLS has problems with determination of truncation parameter k and sensitivity to noise from the measured data.

First problem is addressed in Section 6.2 where a truncation parameter for TTLS is found using adaptive algorithm. Numerical results show that proposed TTLS adaptive provides lower relative error of the reconstructed scattering function than with fixed truncation parameter. Reason for this is that adaptive algorithm minimizes the noise from the measured data while keeping received informations as much as possible.

Regarding the problem of noise sensitivity of TTLS, we regularized the inverse problem with two different methods for RTLS and compared the results with TTLS. First

method is RTLS-Newton where the solution for RTLS problem is found by solving the equivalent eigenvalue problem, which resulted in decrease of execution time since SVD calculations is avoided. We simulated a problem of UT and showed that regularization with RTLS-Newton produced lower relative error of reconstructed scattering function than with TTLS.

The second method for RTLS described in this dissertation is the projection based (PB-RTLS). This method projects the problem onto lower dimensional subspace using generalized Krylov subspace expansion. This resulted in decreasing the execution time of the DBI method. The performance of TTLS and PB-RTLS was analyzed on three phantoms (two simulated and breast phantom) with different levels of noise (20, 25 and 30 dB) considered in the measured data. We have proved that using PB-RTLS gives lower residual error which results in better reconstructed images in all cases.

Finally, we compared RTLS-Newton, PB-RTLS and Tikhonov regularization in general form where the λ is obtained using our adaptive algorithm. These three methods are useful when utilized for the regularization within iterations of DBI. PB-RTLS is the fastest and produces low relative error. However, when more noisier data is considered, Tikhonov regularization combined with our adaptive algorithm is the most accurate.

7.2 Future work

There are three possible directions for our future work on the problem of UT: decreasing the execution time of the regularization methods used in this dissertation and testing them on larger domains, investigate new regularization methods which could provide better quality of reproduced images and examining a different models for UT. More details are listed as follows:

- In recent years, new approach for computing SVD and GSVD with randomized algorithms has been developed. Successful implementation of these algorithms for Tikhonov regularization in standard and general form is presented in [75] and [72] respectively. Our further research will be done in implementing our adaptive algorithm to be suited for these new approximations of Tikhonov regularization which will result in dramatic decrease of execution time.

- Another type of regularization that is more appropriate for reconstruction of sparse domain is ℓ_1 regularization. This approach could be beneficial when utilized for reconstruction of scattering function.
- Other researchers are modeling the UT with full wave inversion so we will compare this approach with the DBI method and analyze advantages and shortcomings of each model.

Bibliography

- [1] M. Almekkawy, A. Carević, A. Abdou, J. He, G. Lee, and J. Barlow. Regularization in ultrasound tomography using projection-based regularized total least squares. *Inverse Problems in Science and Engineering*, pages 1–24, 2019.
- [2] S. Bernard, V. Monteiller, D. Komatitsch, and P. Lasaygues. Ultrasonic computed tomography based on full waveform inversion for bone quantitative imaging. *Physics in Medicine and Biology*, 62(17):7011, 2017.
- [3] M. Birk, S. Koehler, M. Balzer, M. Huebner, N. V. Ruiter, and J. Becker. FPGA-based embedded signal processing for 3D ultrasound computer tomography. In *Real Time Conference (RT), 2010 17th IEEE-NPSS*, pages 1–5. IEEE, 2010.
- [4] M. Birk, E. Kretzek, P. Figuli, M. Weber, J. Becker, and N. V. Ruiter. High-speed medical imaging in 3D ultrasound computer tomography. *IEEE Transactions on Parallel and Distributed Systems*, 27(2):455–467, 2016.
- [5] M. Born and E. Wolf. *Principles of optics: electromagnetic theory of propagation, interference and diffraction of light*. Elsevier, 2013.
- [6] D. Calvetti, L. Reichel, and A. Shuibi. Invertible smoothing preconditioners for linear discrete ill-posed problems. *Applied numerical mathematics*, 54(2):135–149, 2005.
- [7] A. Carević, A. Abdou, I. Slapničar, and M. Almekkawy. Employing methods with generalized singular value decomposition for regularization in ultrasound tomography. In *Medical Imaging 2019: Ultrasonic Imaging and Tomography*, volume 10955, page 1095509. International Society for Optics and Photonics, 2019.

- [8] A. Carevic, A. E. Abdou, J. Barlow, and M. Almekkawy. Using filter factors for regularization in ultrasound tomography. In *2018 40th Annual International Conference of the IEEE Engineering in Medicine and Biology Society (EMBC)*, pages 895–898. IEEE, 2018.
- [9] A. Carević, X. Yun, and M. Almekkawy. Adaptive truncated total least square on distorted born iterative method in ultrasound inverse scattering problem. In *Medical Imaging 2019: Ultrasonic Imaging and Tomography*, volume 10955, page 1095515. International Society for Optics and Photonics, 2019.
- [10] A. Carević, X. Yun, G. Lee, I. Slapničar, A. Abdou, J. Barlow, and M. Almekkawy. Solving the ultrasound inverse scattering problem of inhomogeneous media using different approaches of total least squares algorithms. In *Medical Imaging 2018: Ultrasonic Imaging and Tomography*, volume 10580, page 105800J. International Society for Optics and Photonics, 2018.
- [11] W. C. Chew and Y.-M. Wang. Reconstruction of two-dimensional permittivity distribution using the distorted born iterative method. *IEEE transactions on medical imaging*, 9(2):218–225, 1990.
- [12] J. W. Demmel. *Applied numerical linear algebra*, volume 56. Siam, 1997.
- [13] M. Donatelli, A. Neuman, and L. Reichel. Square regularization matrices for large linear discrete ill-posed problems. *Numerical Linear Algebra with Applications*, 19(6):896–913, 2012.
- [14] M. Donatelli and L. Reichel. Square smoothing regularization matrices with accurate boundary conditions. *Journal of Computational and Applied Mathematics*, 272:334–349, 2014.
- [15] N. Duric, P. Littrup, L. Poulou, A. Babkin, R. Pevzner, E. Holsapple, O. Rama, and C. Glide. Detection of breast cancer with ultrasound tomography first results with the computed ultrasound risk evaluation (cure) prototype. *Medical physics*, 34(2):773–785, 2007.

- [16] N. Duric, P. Littrup, O. Roy, S. Schmidt, C. Li, L. Bey-Knight, and X. Chen. Breast imaging with ultrasound tomography: Initial results with softvue. In *Ultrasonics Symposium (IUS), 2013 IEEE International*, pages 382–385. IEEE, 2013.
- [17] M. Ekstrom and R. Rhoads. On the application of eigenvector expansions to numerical deconvolution. *Journal of Computational Physics*, 14(4):319–340, 1974.
- [18] R. D. Fierro, G. H. Golub, P. C. Hansen, and D. P. O’Leary. Regularization by truncated total least squares. *SIAM Journal on Scientific Computing*, 18(4):1223–1241, 1997.
- [19] S. Gazzola and J. G. Nagy. Generalized arnoldi–tikhonov method for sparse reconstruction. *SIAM Journal on Scientific Computing*, 36(2):B225–B247, 2014.
- [20] H. Gemmeke, T. , M. Zapf, C. Kaiser, and N. V. Ruiter. 3d ultrasound computer tomography: Hardware setup, reconstruction methods and first clinical results. *Nuclear Instruments and Methods in Physics Research Section A: Accelerators, Spectrometers, Detectors and Associated Equipment*, 873:59–65, 2017.
- [21] G. H. Golub, P. C. Hansen, and D. P. O’Leary. Tikhonov regularization and total least squares. *SIAM Journal on Matrix Analysis and Applications*, 21(1):185–194, 1999.
- [22] G. H. Golub, M. Heath, and G. Wahba. Generalized cross-validation as a method for choosing a good ridge parameter. *Technometrics*, 21(2):215–223, 1979.
- [23] G. H. Golub and C. F. Van Loan. An analysis of the total least squares problem. *SIAM Journal on Numerical Analysis*, 17(6):883–893, 1980.
- [24] G. H. Golub and C. F. Van Loan. *Matrix computations*, volume 3. JHU Press, 2012.
- [25] H. Guo and R. A. Renaut. A regularized total least squares algorithm. In *Total Least Squares and Errors-in-Variables Modeling*, pages 57–66. Springer, 2002.
- [26] O. S. Haddadin and E. S. Ebbini. Adaptive regularization of a distorted born iterative algorithm for diffraction tomography. In *Image Processing, 1996. Proceedings., International Conference on*, volume 2, pages 725–728. IEEE, 1996.

- [27] O. S. Haddadin and E. S. Ebbini. Imaging strongly scattering media using a multiple frequency distorted born iterative method. *IEEE transactions on ultrasonics, ferroelectrics, and frequency control*, 45(6):1485–1496, 1998.
- [28] O. S. Haddadin and E. S. Ebbini. Ultrasonic focusing through inhomogeneous media by application of the inverse scattering problem. *The Journal of the Acoustical Society of America*, 104(1):313–325, 1998.
- [29] O. S. Haddadin, S. D. Lucas, and E. S. Ebbini. Solution to the inverse scattering problem using a modified distorted born iterative algorithm. In *1995 IEEE Ultrasonics Symposium. Proceedings. An International Symposium*, volume 2, pages 1411–1414. IEEE, 1995.
- [30] P. C. Hansen. The truncatedsvd as a method for regularization. *BIT Numerical Mathematics*, 27(4):534–553, 1987.
- [31] P. C. Hansen. Regularization, gsvd and truncatedgsvd. *BIT numerical mathematics*, 29(3):491–504, 1989.
- [32] P. C. Hansen. Regularization tools: A matlab package for analysis and solution of discrete ill-posed problems. *Numerical algorithms*, 6(1):1–35, 1994.
- [33] P. C. Hansen. *Rank-Deficient and Discrete Ill-Posed Problems*. SIAM Publications, Philadelphia, PA, USA, 1998.
- [34] P. C. Hansen. Regularization tools version 4.0 for matlab 7.3. *Numerical algorithms*, 46(2):189–194, 2007.
- [35] P. C. Hansen and D. P. O’Leary. The use of the L-curve in the regularization of discrete ill-posed problems. *SIAM Journal on Scientific Computing*, 14(6):1487–1503, 1993.
- [36] L. Hogben. *Handbook of linear algebra*. Chapman and Hall/CRC, 2013.
- [37] T. Hohage. On the numerical solution of a three-dimensional inverse medium scattering problem. *Inverse Problems*, 17(6):1743, 2001.

- [38] T. Hopp, M. Zapf, E. Kretzek, J. Henrich, A. Tukalo, H. Gemmeke, C. Kaiser, J. Knaudt, and N. Ruiter. 3d ultrasound computer tomography: update from a clinical study. In *Medical Imaging 2016: Ultrasonic Imaging and Tomography*, volume 9790, page 97900A. International Society for Optics and Photonics, 2016.
- [39] T. Q. Huy, N. T. Cuc, T. T. Long, T. D. Tan, et al. Tomographic density imaging using modified df-dbim approach. *Biomedical Engineering Letters*, 9(4):449–465, 2019.
- [40] S. A. Johnson and M. L. Tracy. Inverse scattering solutions by a sing basis, multiple source, moment method—part i: Theory. *Ultrasonic Imaging*, 5(4):361–375, 1983.
- [41] I. Jovanovic. *Inverse problems in acoustic tomography, PhD thesis*. Ecole Polytechnique Federale de Lausanne, 2008.
- [42] R. Lavarello and M. Oelze. A study on the reconstruction of moderate contrast targets using the distorted born iterative method. *ieee transactions on ultrasonics, ferroelectrics, and frequency control*, 55(1), 2008.
- [43] R. Lavarello and M. Oelze. Density imaging using a multiple-frequency DBIM approach. *IEEE Transactions on Ultrasonics, Ferroelectrics, and Frequency Control*, 57(11):2471–2479, 2010.
- [44] R. J. Lavarello and M. L. Oelze. Density imaging using inverse scattering. *The Journal of the Acoustical Society of America*, 125(2):793–802, 2009.
- [45] R. J. Lavarello and M. L. Oelze. Tomographic reconstruction of three-dimensional volumes using the distorted Born iterative method. *IEEE Transactions on Medical Imaging*, 28(10):1643–1653, 2009.
- [46] G. Lee and J. L. Barlow. Two projection methods for regularized total least squares approximation. *Linear Algebra and its Applications*, 461:18–41, 2014.
- [47] G. Lee, H. Fu, and J. L. Barlow. Fast high-resolution image reconstruction using tikhonov regularization based total least squares. *SIAM Journal on Scientific Computing*, 35(1):B275–B290, 2013.

- [48] S. K. Lehman and A. J. Devaney. Transmission mode time-reversal super-resolution imaging. *The Journal of the Acoustical Society of America*, 113(5):2742–2753, 2003.
- [49] F. Lin, A. I. Nachman, and R. C. Waag. Quantitative imaging using a time-domain eigenfunction method. *The Journal of the Acoustical Society of America*, 108(3):899–912, 2000.
- [50] C. Liu, Y. Wang, and P. A. Heng. A comparison of truncated total least squares with tikhonov regularization in imaging by ultrasound inverse scattering. *Physics in medicine and biology*, 48(15):2437, 2003.
- [51] Y. Lou, W. Zhou, T. P. Matthews, C. M. Appleton, and M. A. Anastasio. Generation of anatomically realistic numerical phantoms for photoacoustic and ultrasonic breast imaging. *Journal of biomedical optics*, 22(4):041015, 2017.
- [52] C. Lu, J. Lin, W. Chew, and G. Otto. Image reconstruction with acoustic measurement using distorted born iteration method. *Ultrasonic Imaging*, 18(2):140–156, 1996.
- [53] V. Z. Marmarelis, T.-S. Kim, and R. E. Shehada. High resolution ultrasonic transmission tomography. In *Proc SPIE Med Imaging*, volume 5035, pages 33–40, 2003.
- [54] T. D. Mast, A. I. Nachman, and R. C. Waag. Focusing and imaging using eigenfunctions of the scattering operator. *The Journal of the Acoustical Society of America*, 102(2):715–725, 1997.
- [55] T. P. Matthews, K. Wang, C. Li, N. Duric, and M. A. Anastasio. Regularized dual averaging image reconstruction for full-wave ultrasound computed tomography. *IEEE Transactions on Ultrasonics, Ferroelectrics, and Frequency Control*, 64(5):811–825, 2017.
- [56] P. Mojabi and J. LoVetri. Ultrasound tomography for simultaneous reconstruction of acoustic density, attenuation, and compressibility profiles. *The Journal of the Acoustical Society of America*, 137(4):1813–1825, 2015.

- [57] J. L. Mueller and S. Siltanen. *Linear and nonlinear inverse problems with practical applications*. SIAM, 2012.
- [58] S. J. Norton. The inverse-scattering problem and global convergence. *The Journal of the Acoustical Society of America*, 118(3):1534–1539, 2005.
- [59] N. Ozmen. *Ultrasound Imaging Methods for Breast Cancer Detectionm, PhD thesis*. Delft University of Technology, Delft, The Netherlands, 2014.
- [60] C. C. Paige and M. A. Saunders. Towards a generalized singular value decomposition. *SIAM Journal on Numerical Analysis*, 18(3):398–405, 1981.
- [61] M. Pérez-Liva, J. Herraiz, J. Udías, E. Miller, B. Cox, and B. Treeby. Time domain reconstruction of sound speed and attenuation in ultrasound computed tomography using full wave inversion. *The Journal of the Acoustical Society of America*, 141(3):1595–1604, 2017.
- [62] M. Perez-Liva, J. L. Herraiz, J. M. Udías, B. T. Cox, and B. E. Treeby. Full-wave attenuation reconstruction in the time domain for ultrasound computed tomography. In *Biomedical Imaging (ISBI), 2016 IEEE 13th International Symposium on*, pages 710–713. IEEE, 2016.
- [63] R. F. Remis and P. Van den Berg. On the equivalence of the Newton-Kantorovich and distorted Born methods. *Inverse Problems*, 16(1):L1, 2000.
- [64] R. A. Renaut and H. Guo. Efficient algorithms for solution of regularized total least squares. *SIAM Journal on Matrix Analysis and Applications*, 26(2):457–476, 2004.
- [65] N. V. Ruiter, G. Göbel, L. Berger, M. Zapf, and H. Gemmeke. Realization of an optimized 3D USCT. In *Proc. SPIE*, volume 7968, page 796805, 2011.
- [66] M. Slaney, A. C. Kak, and L. E. Larsen. Limitations of imaging with first-order diffraction tomography. *IEEE Transactions on Microwave Theory and Techniques*, 32(8):860–874, 1984.
- [67] G. W. Stewart. *Introduction to matrix computations*. Elsevier, 1973.

- [68] L. N. Trefethen and D. Bau III. *Numerical linear algebra*, volume 50. Siam, 1997.
- [69] S. Van Huffel and J. Vandewalle. *The total least squares problem: computational aspects and analysis*, volume 9. Siam, 1991.
- [70] C. F. Van Loan. Generalizing the singular value decomposition. *SIAM Journal on Numerical Analysis*, 13(1):76–83, 1976.
- [71] K. Wang, T. Matthews, F. Anis, C. Li, N. Duric, and M. A. Anastasio. Waveform inversion with source encoding for breast sound speed reconstruction in ultrasound computed tomography. *IEEE Transactions on Ultrasonics, Ferroelectrics, and Frequency Control*, 62(3):475–493, 2015.
- [72] Y. Wei, P. Xie, and L. Zhang. Tikhonov regularization and randomized GSVD. *Siam Journal on Matrix Analysis and Applications*, 37(2):649–675, 2016.
- [73] J. Wiskin, D. Borup, E. Iuanow, J. Klock, and M. W. Lenox. 3-D nonlinear acoustic inverse scattering: Algorithm and quantitative results. *IEEE Transactions on Ultrasonics, Ferroelectrics, and Frequency Control*, 64(8):1161–1174, 2017.
- [74] J. Wiskin, D. Borup, S. Johnson, and M. Berggren. Non-linear inverse scattering: High resolution quantitative breast tissue tomography. *The Journal of the Acoustical Society of America*, 131(5):3802–3813, 2012.
- [75] H. Xiang and J. Zou. Regularization with randomized svd for large-scale discrete inverse problems. *Inverse Problems*, 29(8):085008, 2013.
- [76] X. Yun, J. He, A. Carevic, I. Slapnicar, J. Barlow, and M. Almekkawy. Reconstruction of ultrasound tomography for cancer detection using total least squares and conjugate gradient method. In *Medical Imaging 2018: Ultrasonic Imaging and Tomography*, volume 10580, page 105800K. International Society for Optics and Photonics, 2018.

Curriculum Vitae

Anita Carević was born in 1988 in Split, Croatia. She received her Bachelor of Science and Master of Science degrees in Mathematics from University of Split in 2009 and 2011 respectively. In 2013 she enrolled in PhD program at University of Zagreb under the supervision of professor I. Slapničar.

She visited Pennsylvania State University, USA, in 2016 and 2017 where she worked with professors M. Almekkawy and J. Barlow on the problems of regularization in ultrasound tomography. She presented this research at SIAM Conference on IMAGING SCIENCE, Bologna, Italy and Ninth Conference on Applied Mathematics and Scientific Computing, Šibenik, Croatia in 2018. The research is also published in publications listed below.

Publication list

Journal Publications

1. M. Almekkawy, A. Carević, A. Abdou, J He, G. Lee, J. Barlow, Regularization in Ultrasound Tomography using Projection Based Regularized Total Least Squares, *Inverse Problems in Science & Engineering*, pages 1-25, 2019.

Conference Publications

1. A. Carević, A. Abdou, I. Slapničar, M. Almekkawy, Employing methods with Generalized Singular Value Decomposition for Regularization in Ultrasound Tomography, *Proceedings of Medical Imaging 2019: Ultrasonic Imaging and Tomography*. Vol. 10955. International Society for Optics and Photonics (SPIE), 2019.

2. A. Carević, X. Yun, M. Almekkawy, Adaptive truncated total least squares on distorted Born iterative method in ultrasound inverse scattering problem, *Proceedings of Medical Imaging 2019: Ultrasonic Imaging and Tomography*. Vol. 10955. International Society for Optics and Photonics (SPIE), 2019.
3. A. Carević, A. Abdou, J. Barlow, M. Almekkawy, Using filter factors for regularization in ultrasound tomography *Proceedings of IEEE Engineering in Medicine and Biology Society*, 2018.
4. A. Carević, X. Yun, G. Lee, I. Slapničar, A. Abdou, J. Barlow, M. Almekkawy, Solving the ultrasound inverse scattering problem of inhomogeneous media using different approaches of total least squares algorithms, *Proceedings of Medical Imaging 2018: Ultrasonic Imaging and Tomography*. Vol. 10580. International Society for Optics and Photonics (SPIE), 2018.
5. X Yun, J He, A Carević, I Slapničar, J Barlow, M Almekkawy, Reconstruction of ultrasound tomography for cancer detection using total least squares and conjugate gradient method, *Proceedings of Medical Imaging 2018: Ultrasonic Imaging and Tomography*. Vol. 10580. International Society for Optics and Photonics (SPIE), 2018.

IZJAVA O IZVORNOSTI RADA

Ja, _____, student/ica Prirodoslovno-matematičkog
fakulteta Sveučilišta u Zagrebu, s prebivalištem na adresi
_____, OIB _____,

JMBAG _____, ovim putem izjavljujem pod materijalnom i kaznenom
odgovornošću da je moj završni/diplomski/doktorski rad pod naslovom:

_____, isključivo moje autorsko djelo, koje je u
potpunosti samostalno napisano uz naznaku izvora drugih autora i dokumenata korištenih u radu.

U Zagrebu, _____

Potpis